**Title**

Prediction of Thermal and Electrical Transport in Nanostructured Materials for Energy Conversion Applications

**Author**

Hosseini, Seyed Aria

**Publication Date**

2021

UNIVERSITY OF CALIFORNIA
RIVERSIDE

# Prediction of Thermal and Electrical Transport in Nanostructured Materials for Energy Conversion Applications

A Dissertation submitted in partial satisfaction
of the requirements for the degree of

Doctor of Philosophy

in

Mechanical Engineering

by

Seyed Aria Hosseini

June 2021

Dissertation Committee:

Dr. Peter Alexander Greaney, Chairperson
Dr. Richard Wilson
Dr. Chen Li

The Dissertation of Seyed Aria Hosseini is approved:

Committee Chairperson

University of California, Riverside

# Acknowledgments

I am grateful to my advisor, without whose help, I would not have been here.

I certify that chapters three and six of this dissertation are the entire articles without being rewritten published in Journal of Physical Review B and ACS Applied Energy Materials, respectively. I also declare that chapters four and five are publicly available on arXiv e-Print archive.

To those who *inspired* it!

# ABSTRACT OF THE DISSERTATION

## Prediction of Thermal and Electrical Transport in Nanostructured Materials for Energy Conversion Applications

by

Seyed Aria Hosseini

Doctor of Philosophy, Graduate Program in Mechanical Engineering
University of California, Riverside, June 2021
Dr. Peter Alexander Greaney, Chairperson

Thermoelectrics (TE) are a class of materials that convert heat directly into electricity. If made sufficiently efficient and inexpensive, these materials could be used to recapture low-grade waste heat from the industrial process as useful electrical energy. The potential energy savings are vast. Recent studies by Lawrence Livermore National Laboratory have reported that more than 68% of U.S. energy consumption escapes as waste heat [1] while recuperating *only* 10% of heat lost into electricity can improve fuel energy efficiency by 20% [2]. This research presented here pursues strategies to make energy harvesting more efficient by using nanoengineering to improve the energy performance of TEs. Three significant theoretical insights are developed that together create a new design paradigm for engineering both thermal and electrical properties of TEs. The first strategy is to enhance the TE power factor through selectively filtering low-energy electrons. A publicly available python design platform called *thermoelectric.py* with innovative mathematical approaches to accurately and efficiently compute, from first principles, the strength, and energy dependence of electron scattering from nanoscale pores and particles with different geometries is developed. The second strategy is the design of the nanoscale morphology of porous TEs to detriment the lattice thermal conductivity through phonon coherent effects. An analytical framework is laid out to model heat current anticorrelation (HCAC) in materials containing specific porous topologies. The model predicts that HCAC leads to an extreme reduction in thermal conductivity of up to 80% compared to structures in which the anticorrelation effect is not observed. The third strategy is a large-scale screening of TE alloys containing nanoscale porosity to find the minimum thermal conductivity. A general model is developed to predict lattice thermal conductivity of dielectrics containing nanoscale to macroscale porosity. The model is robust in providing a good approximation of the results from full Boltzmann transport (BTE) simulations of lattice thermal conductivity for a wide range of pores shapes, sizes, and spacings that span both the diffusive and ballistic regimes. This provides a simple yet accurate estimation of thermal transport in nanostructures that can be used to rapidly screen or design materials for a particular thermal task. As such this work provides an important tool to facilitate the design and discovery of materials for thermal-related applications, without explicitly solving the BTE.

# Contents

# List of Figures

# List of Tables

# Chapter 1

# Introduction

Thermoelectrics (TEs) are materials that convert temperature differences directly into electrical power.1 These materials are currently used in fairly niche applications that require reliability and small footprints, such as providing the power for deep space probes, and the cooling for compact refrigerators. However, they have the potential to transform the way that we use and recover heat if TEs can be created with sufficient efficiency, using materials that are inexpensive, and environmentally benign. TE energy efficiency is described by figure of merit, $ZT = \sigma s^2/\kappa$, where $\sigma$, $S$ and $\kappa$ are electrical conductivity, Seebeck coefficient, and thermal conductivity, respectively. TE performance requires having an optimal balance of several electrical properties in conjunction with very poor thermal conductivity.

This research is motivated by making global energy use more efficient by improving the performance of TEs so that their use to recapture waste heat from industrial processes becomes cost effective. The scope for energy savings from recapturing low-grade waste heat is large. A recent study from Lawrence Livermore National Laboratory has reported that more than 68% of U.S. energy consumption escaped as waste heat [1]. In some industries this ratio is much higher, for example the 80% of the energy loss in the raw mill process of cement production is lost as heat, a process that accounts for almost 2% of the electricity produced worldwide [4]. Large energy savings are also available in the transportation sector. Use of TEs saves up to 4.75% of fuel economy efficiency in modern vehicles where still up to two third of combusted fuel energy waste [5]. Other studies have shown that recuperating only 10% of heat lost into electricity can improve fuel energy efficiency by 20% [2]. Recovering heat in these applications requires compact power generation units that can conform the hot components and exhaust streams of existing industrial infrastructure. This is where TEs offer a particular advantage. TEs are compact and can be made to integrate with existing technologies. They also have no moving parts, no working fluids, and so are considerably more reliable [6]. The compactness also makes TEs attractive to provide the compact power supplies for distributed wirelessly networked sensors that monitor industry 4.0 process manufacturing [7]. Unfortunately, TEs have lower energy conversion efficiency (less than 10%) than mechanical heat engines such as Stirling and Rankine cycles with energy efficiency near to 30% [8]. However, theoretical predictions suggested that engineering interfaces can hugely enhance the efficiency of TEs [9, 10, 11].

The work presented here has generated theoretical insights in three aspects of TEs that each reveals new strategies for the design TEs for energy harvesting applications. My work has also developed new computational tools for the optimization of TEs' performance using these strategies.

The first strategy is the design of nanoscale morphology of porous TEs to reduce thermal conductivity through the "Heat Current AntiCorrelation" (HCAC) mechanism. The central strategy is to make use of the anticorrelation between an incident and reflected paths of phonons that are scattered from pore surfaces so that the outgoing phonon undoes the heat current from the incidence phonon. Consequently, the effective mean free path of phonons is much smaller than the spacing between the scattering centers, a phenomenon we refer to as "supersuppression". The model predicts an extra reduction in thermal conductivity of up to 80% compared to structures in which HCAC is not observed. We showed that to get the maximum reduction, large pore with short neck geometry is needed. In addition, the specular scattering demonstrates stronger HCAC effect and therefore low surface roughness to increase specular scattering is favorable. The model was validated against a set of molecular dynamics simulations for Si for which we were able to observe HCAC and obtain extreme reduction in thermal conductivity of about one order of magnitude for only 3% porosity.

The second strategy is large-scale screening of TE alloys containing nanoscale porosity to find the lowest thermal conductivity. High-frequency phonons are scattered through alloying and low-frequency phonons by pores. A model is developed to predict the thermal conductivity of dielectrics containing nanoscale to macroscale porosity. The model is based on the characteristic length of pores and characteristic MFP of the bulk materials. We have provided a relatively complete database for the characteristic length of pores with different shapes and porosities and characteristic MFP of a wide sweep of dielectrics that are commonly used as TE materials. The model is robust in providing an excellent approximation for a wide range of pores shapes, sizes, and spacings that span both the diffusive and ballistic regimes. This provides a simple yet accurate estimation of thermal transport in nanostructures that can be used to rapidly screen or design materials for a particular thermal task. As such this work provides an important tool to facilitate the design and discovery of materials for thermal-related applications, without explicitly solving the BTE.

The third strategy is to mitigate the effect of porosity on electrical properties by filtering low-energy electrons. This is complementary to the first two strategies since the enhancement in ZT by suppressing the thermal conductivity is partially canceled by the reduction in electrical conductivity. I have created a python design platform called *thermoelectric.py* to accurately and efficiently compute the strength, and energy dependence of electron scattering from nanoscale pores with different shapes, sizes, and spacings is developed. *Thermoelectric.py* is now publicly available as an open-source tool to enable materials engineers to find the shape and size of the optimal pores and the carrier concentrating window in which ZT is most favorable. This is an important step in designing TEs since the optimal ZT in monolithic crystals and nanoporous structures do not take place at the same carrier concentration.

# Chapter 2

# Background and Mathematical Derivations

## 2.1 Introduction

In this chapter, I present the mathematical models I have developed during my studies. In section 2.2, energy-dependent electron filtering in materials containing additive nanoparticles/ porosity is described. This model is validated against a set of experiments done with Mangolini's group at UC Riverside. In their experiments, a fine distribution of SiC dispersoids is sintered in bulk Si TEs. The model is in good agreement with the experiments. This method is used in next chapters to study the effect of nanopores on TE power factor and ZT in Si and $Si_{0.8}Ge_{0.2}$ dielectrics. In section 2.3, an analytical model of anticorrelation (AC) heat flux phenomenon in porous dielectrics is derived. In addition to this generic model, a ray tracing Monte Carlo method to model this phenomenon and molecular dynamics (MD) algorithms to observe this behavior in materials with additive pores are described. This model is used in next chapters to study AC heat flux in Si with porosity. In section 2.5, a new reduced-order model that can be used to quickly assist in the design of dispersoids tailored to semiconducting alloys is developed and validated against a set of Boltzmann transport simulations. This model is used in next chapters to compute thermal conductivity of dielectrics in group IV and group IIIV containing nanoscale pores

## 2.2 Model Energy Dependent Electron Filtering in Nanoengineered Materials

The imperative for reducing global use of energy from fossil fuels is incontrovertible, and humanity is faced with the afflictive task of reducing its consumption of hydrocarbon deposits while the energy demand continues to increase as the world becomes more industrialized. The societal and economic hurdles to reducing energy use are rendered less painful by using energy more efficiently. Towards this end, realizing good thermoelectric (TE) performance in bulk materials that are abundant, inexpensive, and environmentally benign is a holy grail of renewable energy technologies and has the potential to transform our use, and reuse, of energy.

The design of materials for efficient thermoelectric energy conversion is a far-from-trivial task that requires careful optimization of several design parameters, such as doping level, charge carrier concentration, and thermal conductivity. Thermal to electric power conversion efficiency is described by the dimensionless figure of merit, $ZT = (\sigma S^2)/(\kappa_e + \kappa_l)T$, where $\kappa_e$ is the electrical contribution to the thermal conductivity, $\kappa_l$ is lattice thermal conductivity, $\sigma$ is the electrical conductivity and $S$ is the Seebeck coefficient (thermopower) and $T$ is the temperature. For a given material, it is challenging to decouple the transport terms independently. For instance, doping can increase electrical conductivity, decrease thermal conductivity via electron-impurity scattering, but decrease the Seebeck coefficient. Much of the research on thermoelectrics has focused on (a) the search for materials with inherently low thermal conductivity, such as skutterudites and chalcogenides [12], and/or (b) the control of nanoscale features to hinder thermal transport by phonons without affecting electronic transport properties [13]. While promising, these approaches rely either on materials that can be rare and expensive, limiting their potential for large scale terrestrial applications, or on the control of nanoscale features such as diameter and length of nanowires, which also poses synthetic difficulties for large scale implementation. Here we present a theoretical model to elucidate the use of nanoscale additives for the improvement of thermoelectric performance in common semiconductor materials such as silicon. The model strongly indicates that at least part of the improvement in thermoelectric performance observed experimentally originates from the mechanism of electron energy filtering – an approach to enhancing a material's thermopower by selectively scattering low energy electrons to recuperate the damage to the electrical properties – and provides a theoretical framework for guiding the further experimental synthesis of these materials. Bulk silicon is not an efficient thermoelectric material due to its high thermal conductivity [14]; however, it provides an excellent platform for studying the role of design parameters on transport properties, since its bulk properties are extremely well characterized. This study is partially motivated by our recent findings suggesting that oxide inclusion, spontaneously nucleated during the sintering of silicon nanoparticles, can be effective at improving thermoelectric power conversion [15]. While the mechanism is attractive, this synthesis route is problematic since the thermodynamically-driven nucleation of oxide inclusions is difficult to control, meaning that inclusions size and density are not easily and independently tunable. Here we use silicon carbide nanoparticles as an additive that is mechanically mixed via ball milling with silicon feedstock powder. The addition of even a minor quantity of silicon carbide nanoparticles (5% by volume) increases the overall performance significantly. Careful transport measurements, coupled with detailed modeling of the electronic transport properties, unequivocally confirm that energy-selective electron scattering is responsible for the performance enhancement. The energy-selective scattering increases the Seebeck coefficient and the overall power factor (PF), defined as $\sigma S^2$. Our study suggests that carefully designed nanoinclusions can enable one to increase doping concentration without the usual decrease in the Seebeck coefficient. As such, the approach overcomes long-standing intrinsic constraints that have limited the power conversion efficiency of thermoelectric materials.

### Model Transport Coefficients in Bulk Thermoelectrics

The electrical conductivity and thermopower of a population of independent charge carriers can be derived from the Boltzmann transport equation by integrating the contribution from all carrier states. In an isotropic system where the states can be enumerated by their energy, and using the single relaxation time approximation for the collision operator, these can be written as integrals over the carrier energy $E$, so that $\sigma$, $S$, and $\kappa_e$ are given by [16]

$$\sigma = \frac{-1}{3} e^2 \int \chi(E,T)\tau(E,T) dE = \frac{-1}{3} e^2 \Delta_0, \tag{2.1}$$

$$S = \frac{-1}{eT} \frac{\int \gamma(E,T)\tau(E,T) dE}{\int \chi(E,T)\tau(E,T) dE} = \frac{-1}{eT}(\Delta_1 - E_f), \tag{2.2}$$

$$\kappa_e = \frac{-1}{3T} e^2 \left( \int \zeta(E,T)\tau(E,T) dE - \frac{(\int \gamma(E,T)\tau(E,T) dE)^2}{\int \chi(E,T)\tau(E,T) dE} \right) = \frac{-1}{3T} \Delta_0 (\Delta_2 - \Delta_1^2). \tag{2.3}$$

Here the function $\chi(E,T) = \nu^2(E) D(E) \dfrac{df(E,E_f,T)}{dE}$, lumps together the materials density of carrier states, $D(E)$, and group velocity, $\nu(E)$, with the energy derivative of the Fermi-Dirac occupancy, $f(E,E_f,T)$, where $E_f$ is the Fermi level. The functions $\gamma(E,T) = (E - E_f)\chi(E,T)$ and $\zeta(E,T) = (E - E_f)^2 \chi(E,T)$. Equations 2.1, 2.2 and 2.3 also express the relationship between the transport properties and $\Delta_n$, the moments of the distribution of conductivity over carriers with different energy, defined as

$$\Delta_n = \begin{cases} \int \chi\tau dE & n = 0 \\ \frac{1}{\Delta_0} \int E^n \chi\tau dE & n \neq 0 \end{cases} \tag{2.4}$$

The Seebeck coefficient from equation 2.2 obtains its largest magnitude by maximizing the asymmetry of product $D\tau\nu^2$ about the Fermi level to move its center of current, $\Delta_1$, away from the Fermi level. In bulk semiconductors, the relaxation time, $\tau$, from impurities and phonons is inversely proportional to the electronic density of states, $D(E)$ [17], with a weak dependency on carrier energy and a prefactor that appears in the numerator and denominator of equation 2.2. This makes the Seebeck coefficient quite insensitive to the overall magnitude of electron-phonon scattering and leaves $\nu(E)$ as the only property that impacts Seebeck coefficient. As a result, most approaches to optimizing power factor, $\sigma S^2$, focus on engineering the band structure and Fermi level to tune the charge carriers concentration

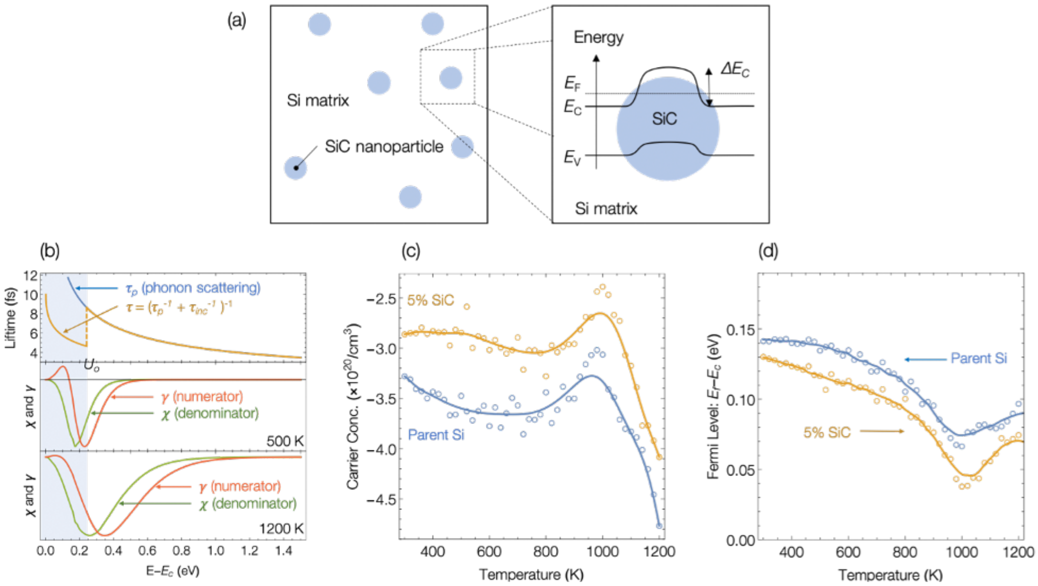

Figure 2.1: (a) Schematic picture of the energy barrier $\Delta E_c$ for filtering conduction band electrons in Si due to the conduction band offset of embedded SiC nanoparticles. Panel (b) illustrates the electron energy filtering concept. The upper plot shows the energy dependence of the electron scattering time, including an additional filtering scattering process that is felt by all electrons with energy less than $U_o$. The lower plots show the kernels $\chi$ and $\gamma$, normalized, and plotted at 500 K (middle) and 1200 K (bottom). The additional electron filtering scattering in the shaded region causes a larger reduction of the $\tau$ weighted integral of $\chi$ than $\gamma$. Panel (c) shows the temperature dependence of the experimentally measured carrier concentration (circles) and its smoothed interpolation (solid lines) for the P-doped silicon with 0% and 5% volume fraction of SiC dispersoids. The temperature dependence of the Fermi level computed to be self-consistent with the experimental carrier concentration is plotted in panel (d). The carrier concentration is lower in the material with 5% volume fraction of SiC dispersoids.

and effective mass to align the Fermi energy to where the density of states is changing most rapidly [18]. Unfortunately, these parameters produce countervailing responses in $S$ and $\sigma$, so the overall scope for enhancing the power factor is limited.

An alternative strategy for generating asymmetry in $D\tau\nu^2$ is to add extrinsic scattering processes (a task that is easier than engineering intrinsic properties) to break the reciprocity of $D$ and $\tau$. Introducing any new scattering mechanism shortens the electron relaxation time and hence reduces $\sigma$. For the Seebeck coefficient, however, $\tau$ appears in both numerator and denominator of equation 2.2, consequently both numerator and denominator are decreased by the additional scattering mechanism. The central concept in electron energy filtering is to introduce a scattering mechanism that can reduce the denominator of $S$ faster than the numerator so that the overall magnitude of the Seebeck coefficient is increased.

The electron energy filtering concept is illustrated graphically in figure 2.1b, which plots normalized $\chi$ and $\gamma$ functions for the conduction band of silicon on the same axes as $\tau$, the electron lifetime. For $n$-doped semiconductors, $\chi$ is negative for any $E$ in the conduction band, and thus $\gamma$ is positive for electrons with energy lower than $E_f$. The high energy tails in $\chi$ and $\gamma$ look functionally similar, and imposing electron scattering in the high energy region has a similar scaling effect on the magnitude of the integrals in the numerator and denominator of equation 2.2. At low energies around and below the Fermi energy, $\chi$ and $\gamma$ are functionally very different. In this region, $\gamma$ contributes little or negatively to its integrated magnitude, whereas $\chi$ contributes strongly to its integrated magnitude. Hence introducing processes for selectively scattering electrons with energies in the blue shaded region of figure 2.1b will decrease the denominator of equation 2.2 faster than the numerator, yielding an increase in $S$ – and can even increase the power factor.

The addition of SiC dispersoids to Si provides additional electron and phonon scattering centers that could enable electron filtering; however, since phosphorous is not expected to dissolve in SiC, the presence of the nanoinclusions effectively reduces the overall carrier concentration. To discriminate the effects of changes in carrier concentration from electron filtering we require a self-consistent and quantitatively accurate model of the electrical transport properties. To this end we have developed a semiclassical transport model that computed equations 2.1 and 2.2 using the ab initio computed band structure of pure Si in combination with the experimentally measured carrier concentration.

### Model Intrinsic Properties

The terms $D(E)$, and $\nu(E)$, in functions $\chi$ and $\gamma$ in equations 2.1–2.4 were derived from the conduction band of Si computed with density functional theory (DFT) using the Vienna Ab initio Simulation Package (VASP) [19, 20, 21, 22]. The calculations were performed using the generalized gradient approximation (GGA) with the Perdew-Burke-Ernzerhof exchange correlation functional (PBE) [23]. Ion cores were represented with projector augmented wave (PAW) pseudopotentials [24, 25], the Kohn-Sham wave functions constructed using a planewave basis set with a 700 eV energy cutoff, and a $12 \times 12 \times 12$ Monkhorst-Pack k-point grid was used to sample the Brillouin zone [26]. The Si primitive cell and atomic basis were relaxed to minimize forces on the atoms to better than $10^{-6}$ eV/Å. The electronic band structure used to compute $D(E)$ and $\nu(E)$ were generated from a $45 \times 45 \times 45$ k-point grid. These intrinsic materials properties were treated as temperature independent. The group velocity was obtained from the conduction band curvature, $\nu = 1/\hbar|\nabla_k E|$ along the $\langle 100\rangle$ directions on the $\Gamma$ to $X$ Brillouin zone path.

### Model Fermi Level

The final term that appears in the distributions $\chi$ and $\gamma$ is the Fermi energy. This is not an intrinsic property, $E_f$ is strongly dependent on the carrier concentration,

$N_i$, and experimentally this is found to vary non-monotonically with temperature as the solubility of the phosphorus dopant changes. Rather than model the physics of the temperature dependence of carrier concentration (which is unrelated to electron transport), we use the empirically measured carrier concentration as an input and then compute the Fermi level that gives the same carrier population in the DFT computed conduction band. This circumvents the problem that DFT underestimates the bandgap as the Fermi level is computed self-consistently from the conduction band using the conduction band edge to set the reference frame. In this method Joyce and Dixon approximation of $E_f$ for degenerate semiconductors, $\frac{E_f-E_c}{k_B} \simeq \ln(\frac{N_i}{N_c}) + 1/\sqrt{(8)}(\frac{N_i}{N_c}) - (3/16 - \sqrt{3}/9)(\frac{N_i}{N_c})^2$ [27], is used as the initial guess. Here $N_c$ is the effective density of states in the conduction band. For Si, the effective density of states in the conduction band is defined as $N_c = 5.3 \times 10^{21} \times T^{3/2}$ 1/cm$^3$ [28]. The $E_f$ iterates to meet the relation between charge density and density of state ($n = \int_{E_c}^{\infty} D(E)f(E)dE$). The experimental measurements of carrier concentration are plotted in figure 2.1c. This shows that the reduction in carrier concentration from the parent Si to the material with 5% SiC inclusions is larger than the 5% reduction dopant level due to the presence of the undoped SiC nanoparticles. This is due to unavoidable variation in doping level introduced during the mechanical mixing of the silicon feedstock powder and the red phosphorous. The experimental measurements are noisy and so for the transport model, the carrier concentration was represented with the continuous smoothing function fit through the experimental data — the lines in figure 2.1(c). The Fermi levels computed for these carrier concentrations are plotted in figure 2.1(d) where it can be seen that, although the addition of SiC nanoinclusions lowers $E_f$, at all temperatures $E_f$ is in the conduction band. This implies that there is a range of electron energies for which $\gamma$ is positive. The addition of a scattering mechanism for low energy electrons is thus expected to lead to an increase in the magnitude of $S$.

**Model Lifetime**

Semiconductor TEs are generally doped to beyond their saturation level (supersaturate solutions). In these materials, strongly screened Columbic force induced by ionized impurities is the main source of scattering. The transition rate between initial ($E_i$) and final ($E_f$) energy states has $SR(E_i, E_f) = \frac{2\pi N_i e^4 L_D^4}{(4\pi\epsilon\epsilon_o)^2 \hbar\Omega}\delta(E_f - E_i)$, where $L_c$, $\Omega$, $\epsilon$, and $\epsilon_o$ are Debye length, volume, relative and vacuum permittivity, respectively [29]. In this case, the electron lifetime is defined as [29]

$$\tau_{im}(E) = \frac{\hbar}{\pi N_i \left(\frac{e^2 L_D^2}{4\pi\epsilon\epsilon_o}\right)^2 D(E)}. \tag{2.5}$$

We use $\epsilon = 11.7$ to model permittivity in Si [28]. For the strongly screened Columbic potential $L_D$ is small so that $1/(L_D^4)$ in equation 2.5 is pivotal. The Debye length has generalized form of [30]

$$L_D = \frac{e^2 N_c}{4\pi\epsilon\epsilon_o k_B T}\left[F_{-\frac{1}{2}}(\eta) + \frac{15\alpha k_B T}{4} F_{\frac{1}{2}}(\eta)\right], \tag{2.6}$$

where $N_c = 2\left(\frac{m_c k_B T}{2\pi\hbar^2}\right)^{\frac{3}{2}}$ is the effective density of states in the conduction band and $m_c$ is the conduction band effective mass. While the electron lifetime in equation 2.5 serves reasonably well for many semiconductors, one should note two shortcomings of the Born approximation failures for slow moving electrons in Coulomb potential and deficiency of simply computing scattering from a single impurity and then multiplying it by number of impurities in capturing interference effects occur as electron wave propagate through random distribution of impurities in deriving equation 2.5. We modeled the conduction band effective mass variation with temperature using $m_c(T) = m_c^*(1 + 5\alpha k_B T)$ [31]. The term $m_c^*$ is equal to $0.23 m_e$, where $m_e$ is free electron rest mass equal to $9.11 \times 10^{-31}$ kg. The reciprocal energy, $\alpha = 0.5$ eV$^{-1}$ describes the deviation of the conduction band from parabolic due to the admixture of s-like conduction band states and p-like valence band states [32]. This model assumes linear dependency on temperature and does not count for degeneracy in high carrier population. A better model that captures dopant concentration needs further study. We remark that for moderate and low carrier populations, the electron charged impurities scattering rate is modeled using Brooks and Herring [29]

$$\tau_{ion} = \frac{16\pi\sqrt{2m_c}(4\pi\epsilon\epsilon_o)^2}{e^4 N_i\left(\ln(1+\beta) - \frac{\beta}{1+\beta}\right)} E^{\frac{3}{2}} \tag{2.7}$$

where $\beta = \frac{8 m_c E L_D^2}{\hbar^2}$. The second important scattering mechanism specially at high temperature in nonpolar semiconductors like Si is due to the acoustic phonon deformation potential. For electron phonon interaction, Ravich defined the lifetime as [33]

$$\tau_p(E) = \frac{\rho\nu^2\hbar}{\pi D_A^2 k_B T D(E)}\left(\left[1 - \frac{\alpha E}{1+2\alpha E}\left(1 - \frac{D_v}{D_A}\right)\right]^2 - \frac{8}{3}\frac{\alpha E(1+\alpha E)}{(1+2\alpha E)^2}\frac{D_v}{D_A}\right)^{-1} \tag{2.8}$$

Here $\rho$ and $\nu_s$ are the crystal's mass density and speed of sound, respectively, and $D_v$ and $D_A$ are electron and hole deformation potentials and equal to 2.94 eV and 9.5 eV, respectively [32]. We use $\rho = 2329$ kg/m$^3$ and $\nu_s = \sqrt{(B/\rho)}$, where $B$ is bulk module defined as $B = 98$ GPA [28].This equation accounts for both absorption and emission of phonons. Note that the electron lifetime is strongly dominated by ion scattering and has weak dependency on phonon scattering. The other scattering terms of electron-electron and electron intervalley scattering has negligible importance in determining the electron lifetime and are excluded in calculations without loss of accuracy.

### 2.2.1 Model Transport in Nanocomposite Thermoelectrics

Electron transport in nanocomposites with non-ionized particles is distinguished from bulk films through (a) changes in carrier populations and therefore the Fermi level (b) extra extrinsic scattering term of electron-nanoparticle, $\tau_{np}$, (c) stronger electron grain boundary scattering rate, $\tau_{gb}$, because of the finer grain boundary length. The population in nanocomposite Si using self-consistent method described in previous section. To compute electron lifetime from the two extra scattering terms of nanoparticles and grains, we used Fermi's golden rule to relates the transmission probability from initial energy state to the distribution of final energy states for a given time invariant potentials. The final form of lifetime for energy conservative scattering in Born approximation is [34]

$$\tau^{-1}(s) = \frac{N}{(2\pi)^2\hbar} \int_{E(k')=0} \frac{M_{kk'}\overline{M}_{kk'}}{\nabla E(k')}(1-\cos\theta)dS(k') \tag{2.9}$$

Here, $M_{kk'}$ is the matrix element operator shows the coupling strength between initial and final wavefunctions and the number of ways the transmission may happen, $N$ is the number density of scattering source and $\theta$ is the angel between initial and final wave vectors. For the Bloch waves, $M_{kk'}$ is defined as $M_{kk'} = \int e^{i(k'-k).r}U(r)dr$ [35].

In equation 2.9, $S(k')$ represents electron isoenergic surfaces. For semiconductors with degenerate transverse modes, the isoenergic surfaces near the conduction valley often describe as $E(k) = \hbar^2[(\frac{(k_l-k_{ol})^2}{2m_l^*} + \frac{(k_t-k_{ot})^2}{m_t^*}]$, where $E(k)$, $k_o = (k_{ol}, k_{ot}, k_{ot})$, $m_l^*$, $m_t^*$ are energy level from conduction band edge, conduction band minimal wavevector, longitudinal and transverse effective masses, respectively. For silicon, $m_l^* = 0.98m_o$, $m_t^* = 0.19m_o$ where $m_o$ is free electron rest mass, and $k_o = 2\pi/a(0, 0, 0.85)$, where $a$ is Si lattice parameter equal to 0.543 nm [28].

### Model Electron Lifetime by Nanoparticles

The band alignment at the interface of nanoparticles presents a barrier to electron transport equal to the band offset of conduction bands in bulk silicon and the inclusions ($\mathrm{U_o}$). For spherical nanoparticles, the scattering potential term, given as, $U(r) = U_o\Pi(r_o - r)$, where $r_o$ is the nanoparticle's radius and $\Pi(r)$ is a dimensionless boxcar function equal to unit inside and zero outside of the particles. For the spherical symmetric potential, $M_{kk'}$ only depends on $q = \Delta K_{kk'}$ and is defined as [36]

$$M_{kk'} = \frac{4\pi U_o}{q^2}\left(\frac{1}{q}\sin(r_o q) - r_o\cos(r_o q)\right) \tag{2.10}$$

At equilibrium, Fermi energy level of nanoparticles and parent material aligned leaving the band offset between SiC nanoparticles and silicon, $U_o$, equal to the difference between Fermi energy level and conduction band edge of the SiC. For intrinsic semiconductors Fermi energy level is located at the middle of band gap so that $U_o = \frac{1}{2}E_g$. The SiC band gap varies from 2.36 eV at 300 K down to 2.036 eV at 1200 K following ($E_g = 2.39 - 6.0 \times 10^{-4} \times \frac{T^2}{T+1200}$) [28]. Such a variation has negligible effect on scattering rate so that we used temperature independent value of $\mathrm{E_g}$=2.19 eV (and therefore $U_o = 1.095$ eV) to model electron-nanoparticle scattering rate. Note that $N$ is equation 2.9, is the number density of nanoparticles and is equal to $N = \frac{3\phi}{4\pi r_o^3}$, where $\phi$ is the volumetric fraction of nanoparticle. Equations 2.9 and 2.10 are used to compute the electron lifetime of nanoparticles.

### Model Electron Lifetime by Grain Boundaries

Along with the change in dopant concentration, the addition of 1% and 5% of SiC nanoparticles results in a 22% and 40% reduction in the grain size, respectively. It is known that grain boundaries can cause an electron filtering effect, particularly if the boundaries include segregated species such as oxygen that provide centers for trapping charge carriers [37]. However, this effect only becomes significant in much smaller grain sizes. For our Si/SiC nanocomposites, even with a 40% size reduction, the grains are still an order of magnitude larger than average electron mean free path in P-doped Si (which is only a few nanometers only at room temperature for carrier concentrations in excess of $10^{20}$ $1/\text{cm}^3$) [13]. Furthermore, we have computed the rate of electron scattering from grains (this is of special importance in next section where we evaluate the scope of enhancement in power factor in Si nanocomposites) using the approach by Minnich et al in Ref. [38] in which they have modeled grain boundaries as decomposition of many local regions, each interacts independently with charge carriers and coherently scatters electron waves. The model potential for grain boundaries in their work described as

$$U_{GB} = \begin{cases} U_g e^{\frac{-|z|}{z_o}} & r < r_{GB} \\ 0 & r > r_{GB} \end{cases} \tag{2.11}$$

In this equation, $z$ is the direction normal to the grain with $z = 0$ at the center of the grain boundary, $r_{GB}$ is a constant on the order of the screening length, and $z_o$ is a constant related to the size of the depletion region. $U_g$ in this model is proposed as, $U_g = \frac{e^2 N_t^2}{8\epsilon\epsilon_o N_c}$, where $\epsilon$ and $\epsilon_o$ are relative and vacuum permittivity, respectively, $N_c$ is the doping concentration, and $N_t$ is the area density of traps. The matrix element of this potential is

$$M_{kk'} = 4\pi U_g \left[\frac{z_o}{1 + (q_z z_o)^2}\right] r_o^2 \left[\frac{J_1(q_r r_o)}{q_r r_o}\right] \tag{2.12}$$

where $J_1(q_r r_o)$ is the first-order Bessel function of the first kind, $q = k - k'$, $q_r$ and $q_z$ are the $r$ and $z$ component of $q$, respectively. Equations 2.9 and 4.16 are used to compute $\tau_{gb}$. Unfortunately, there is a limit information about the trap area density ($N_t$) and the exact value of $z_o$ and $r_o$. Nevertheless, we know that depletion regime and the screening length are in the order of few nm. We used (high value of) $N_t = 10^{13} \frac{1}{\text{cm}^2}$ for trap density of doped silicon, $z_o = 1$ nm and $r_o = 1$ nm [39].

### Modified Electron Density of State in Nanocomposites

The nanoparticles will not change the concentration of carrier concentration locally in the remaining Si (nor the Fermi energy), but it will change the volume-averaged carrier concentration due to the reduction in the volume-averaged density of states. This will impact the conductivity, and thus the effective electrical conductivity of nanocomposite materials is modeled as $\sigma_{\text{eff}} = (1 - \phi)\sigma$. This change does not affect the Seebeck coefficient since the changes in the density of state cancels out for the denominator and numerator of $S$ equation. We assumed that nanoparticles do not change the band structure of the Si. We remark that in Si with narrow nanoparticle spacing, confinement effect leads to flattening of the conduction band [40, 41] and increases the effective mass [40], making transport coefficients different from the bulk Si; However, considering low volume fraction of SiC particles ($\phi = 0.05$) within which the inclusions are far apart, SiC nanoinclusions can be considered as perturbations encountered by the electronic wave functions of bulk Si.

### 2.2.2 Maximum Theoretical Power Factor Enhancement

The approach of electron energy filtering is to shift the transport distribution's center of mass by tuning $\tau$ – in essence blocking or filtering low energy electrons so that they do not contribute to transport. The concept has the practical advantage that it is easier to add extrinsic sources of scattering to a material than it is to tune the material's band structure. However, typically one can only add sources of electrical scattering which means that, as with tuning $\chi$, enhancement of $S$, is obtained at the expense of $\sigma$. This can still yield an improvement in $ZT$ providing the power factor is increased. When tuning the parameters in $\chi$ it is found that the trade-off between $S$ and $\sigma$ leads to a narrow window of optimal conditions that maximize the power factor. However, as we demonstrate below, no such trade-off exists when tuning $\tau$. Electron energy filtering can always be made to increase $S^2$ more quickly than $\sigma$, enabling the power factor, in theory, to be increased indefinitely.

#### Cutoff Model – Ideal Filtering Effect

To better understand the enhancement in power factor that can be obtained with the energy selective filtering we can consider the extreme case where all the electrons with energy lower than $U_0$ are completely blocked. For this perfect filtering case it is useful to evaluate the fraction of the total transport integrals in $\chi$ and $\gamma$ as a function of energy above the conduction band edge. We call these $X(E)$ and $\Gamma(E)$ and define them as

$$X(E) = \frac{\int_0^E dE'\chi(E')\tau_p(E')}{\int_0^\infty dE'\chi(E')\tau_p(E')} \tag{2.13}$$

$$\Gamma(E) = \frac{\int_0^E dE'\gamma(E')\tau_p(E')}{\int_0^\infty dE'\gamma(E')\tau_p(E')} \tag{2.14}$$

The function $X(E)$ is always positive, while $\Gamma(E)$ is negative for $E < E_A$, where $E_A$ is the energy level at which $\int_0^{E_f} dE\gamma(E) = -\int_{E_f}^{E_A} dE\gamma(E)$. The function $\Gamma(E)$ is always less than $X(E)$ and converges to 1 more slowly than $X(E)$. The integral fractions describe how much an energy range in the conduction band contributes to transport. They can be used to define, $\alpha_\sigma(U_0)$, the ratio of a materials' electrical conductivity with and without energy filtering. Similarly, we define $\alpha_S(U_0)$ and $\alpha_{PF}(U_0)$

$$\alpha_\sigma(U_0) = 1 - X(U_0) \tag{2.15}$$

$$\alpha_S(U_0) = \frac{1 - \Gamma(U_0)}{1 - X(U_0)} \tag{2.16}$$

$$\alpha_{PF}(U_0) = \frac{(1 - \Gamma(U_0))^2}{1 - X(U_0)} \tag{2.17}$$

The power factor enhancement, $\alpha_{PF}(U_0)$, always rises above unity for small values of $U_0$, but falls back below one when $\Gamma(U_0) = 1 - \sqrt(1 - X(U_0)$. The optimum filtering threshold for power factor enhancement, $U^*_{PF}$, satisfies the condition

$$U^*_{PF} = E_f - \frac{eTS}{2}\left(\frac{1 - \Gamma(U^*_{PF})}{1 - X(U^*_{PF})}\right) = E_f - \frac{eTS}{2}\alpha_S(U^*_{PF}) \tag{2.18}$$

where $S$ is the Seebeck coefficient in bulk material. This implies that $E_f < U^*_{PF} < E_A$. Figure 2.2(a) shows the variation of power factor with carrier concentration for ideal electron filtering in Si as a function of energy filtering cutoff, $U_0$ at 500 K. This suggests that

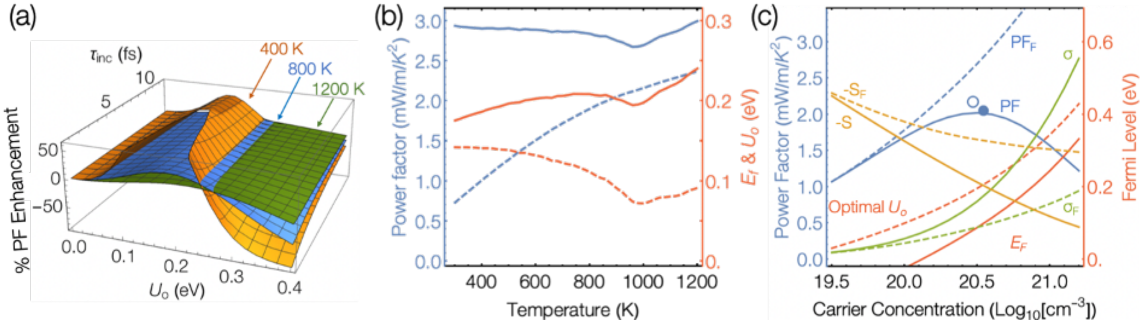

Figure 2.2: Plot (a) shows the change in power factor of P-doped Si as a function of the electron filtering threshold, $U_o$, and filter scattering time $\tau_o$ at 300 K (Gold), 500 K (blue), and 1300 K (green).There is no observed dependency between optimal values of $U_o$, and $\tau_o$. Plot (b) the optimal filtering threshold (solid red line) as a function of temperature for the parent Si and (solid blue line) the corresponding theoretical maximum power factor if filtering is perfect (i.e., $\tau_o = 0$).

theoretically there is considerable room for further improvement to the power factor, particularly at low temperatures. More surprising is how the maximum obtainable power factor changes with carrier concentration as plotted in figure 2.2(b) – it shows that if one can tune the energy filtering threshold then one should adopt a new paradigm for the design and optimization of thermoelectric materials. In the traditional picture of a $n$-type thermoelectric, the material's power factor is maximized at carrier concentrations that place the Fermi energy at the conduction band edge. However, if one applies perfect energy filtering one can obtain greatly enhanced power factor by doping the material so as to push the Fermi energy deeper into the conduction band — even to doping levels where thermal conductivity is dominated by electron transport. This presents a new strategy for designing thermoelectric which is freed from the constraint of optimizing the carrier concentration.

### Generalized Cutoff Model

While the perfect cutoff model suggests an extremely large enhancement in power factor, it is not feasible to completely block low energy electrons, here, we instead take a phenomenological approach. Regardless of the mechanism of scattering, we assume that the scattering rate from inclusions is largest for low energy electrons and weaker for high energy electrons (consistent with Fermi's golden model of nanoparticles scattering rate). The reverse trend is true for ion scattering and so we assume that scattering of low energy electrons is dominated by scattering from inclusions but that there can exist a crossover energy $U_o$ where the scattering of electrons with energy above this threshold is predominantly from phonons. The filtering threshold $U_o$ is related to the conduction band offset, $\Delta E_C$. The simplest phenomenological model of inclusion scattering is to model the additional rate of scattering as a step function so that electrons with energy $E < U_o$ are subjected to an additional scattering process with characteristic lifetime $\tau_o$, represented mathematically as

$$\tau_{inc}^{-1} = \tau_o^{-1} \vartheta(U_o - E) \tag{2.19}$$

where $\vartheta$ is the Heaviside function. Matthiessen's rule is used to sum the rate of this extrinsic scattering term with electron-impurity and electron-phonon scattering giving the total electron scattering rate

$$\tau^{-1} = \tau_{im}^{-1} + \tau_p^{-1} + \tau_{inc}^{-1} \tag{2.20}$$

Using this scattering function in the transport model we can examine the model's prediction for transport properties of Si containing 5% volume fraction of SiC nanoparticles. Figure 2.2c shows the predicted fractional increase in power factor for a material with the carrier concentration of $n = 10^{20}$ 1/cm$^3$, if we could independently control $U_o$ and $\tau_o$. This provides several important insights. The first is that the optimal filtering threshold, $U_o$, for enhancing power factor is independent of $\tau_o$ and vice versa. This is a fortuitous result as it provides post hoc justification for the phenomenological filtering model — although we have no mechanistic rationale for our choice of the additional scattering time $\tau_o$, we do not need to know $\tau_o$ to think about $U_o$ and how to optimize it. Figure 2.2(c) shows that at room temperature electron energy filtering has the potential to produce a very large enhancement of the power factor, but that the scope for enhancing the power factor diminishes at higher temperatures. Figure 2.2(c) also shows that if the filtering threshold is not optimal electron filtering can diminish the power factor rather than enhance it. Shorter $\tau_o$ is always more beneficial for power factor enhancement, but the optimal $U_o$ depends on temperature.

## 2.3 Model Anticorrelated Heat Current in Materials Containing Nanoscale Porosity

The advancements in nanoengineering methods enabled extreme reduction in thermal conductivity of Si-based nanostructures including nanowires [42, 42], thin films [43, 44], nanomesh [45, 46], superlattices [47, 48, 49] and Si-based nanoporous alloys [50, 51, 52]. The additional phonon scattering at the surfaces of these nano defects blocks phonons with long mean free path and thereby detriments the lattice thermal conductivity. While phonon-gas model suffices to capture the detail of particle-like behavior of phonons in nanostructures, the phonon *coherent* transport is missed in this scheme. In a recent work, we have studied topological features of Si-based structures containing nanoscale porosity and identified *geometry-dependent* anticorrelated (AC) heat current phenomenon which causes an additional reduction in thermal conductivity, of up to 80% compare to similar porous structures in which heat current anticorrelation is not observed. The origin of this behavior returns back to multiple specular reflection of trapped phonons between the pores such that their contribution to the thermal conductivity is partly undone.

The AC effect is not only remarkable due to its ability to significantly reduce thermal conductivity, but because it allows unprecedented control over the thermal behavior of the materials. We have identified the nature and impact of the AC effect in nanoporous Si and observed it to be a function of pore size/neck and distribution. We have determined that the AC can be controlled in terms of both the amount and duration of anticorrelated specular phonon scattering. The pores provide two functions: the periodicity (along the transport direction) controls the lifetime over which a phonons' momentum is correlated, and the packing, determined by pore sizes and necks (perpendicular to transport), controls the strength of correlated phonon reflections. These functions can be engineered by tuning the spacing/periodicity between pores along the transport direction, and the pore and neck sizes, respectively. The AC effects are observed for necks of at least up to $\sim 6$ nm suggesting that the porous structures can be scaled to such technologically feasible pore/neck sizes, making it easier to be used as a design tool to control thermal conductivity beyond traditional boundary scattering.

Here, I present an *analytical* model for AC heat current in materials containing nanoscale porosity. This model is used to show how different types of phonon scattering manifest as signatures in the heat current autocorrelation function, we further investigate the extent to which other nanostructuring approaches (e.g., inclusions, straight surfaces) can be designed to scatter phonons specularly, and the nature of scattering at the boundaries (at low temperatures). Ray tracing Monte Carlo method is used to test how different scattering behavior that could be occurring at the surfaces of the pores would be manifest in the heat current autocorrelation (HCACF).

## 2.4 Analytic Model of Uncorrelated Scattering

To begin, we lay out the theoretical basis for the ray tracing model by establishing that macroscopic thermal conductivity can be computed from the sum of the autocorrelation functions of the individual phonon modes' occupancy fluctuations. The Green-Kubo equation gives the thermal conductivity tensor as the integral of the total heat current autocorrelation function:

$$\kappa = \frac{V}{k_B T^2} \int_0^\infty d\tau \left\langle \mathbf{J}(t) \bigotimes \mathbf{J}(t+\tau) \right\rangle, \tag{2.21}$$

where $\mathbf{J}(t)$ is the total instantaneous heat flux at time $t$, in the volume of materials $V$ that is at thermal equilibrium at temperature $T$. The autocorrelation function $\langle \mathbf{J}(t) \bigotimes \mathbf{J}(t+\tau) \rangle$ is the time-averaged dyadic of the heat fluxes an interval $\tau$ apart. The contribution to the heat current from the mode with wave vector $\mathbf{k}$ and polarization $p$ is

$$\mathbf{J}_{\mathbf{k}p}(t) = \left( \frac{1}{2} + n_{\mathbf{k}p}(t) \right) \frac{\hbar \omega_{\mathbf{k}p} \nu_{\mathbf{k}p}}{V}, \tag{2.22}$$

where $n_{\mathbf{k}p}(t)$ is the mode's occupancy at time $t$. This can be rewritten in terms of the average flux and the instantaneous excursion from the average:

$$\mathbf{J}_{\mathbf{k}p}(t) = \langle \mathbf{J}_{\mathbf{k}p} \rangle + \left( n_{\mathbf{k}p}(t) - \langle n_{\mathbf{k}p} \rangle \right) \frac{\hbar \omega_{\mathbf{k}p} \nu_{\mathbf{k}p}}{V}, \tag{2.23}$$

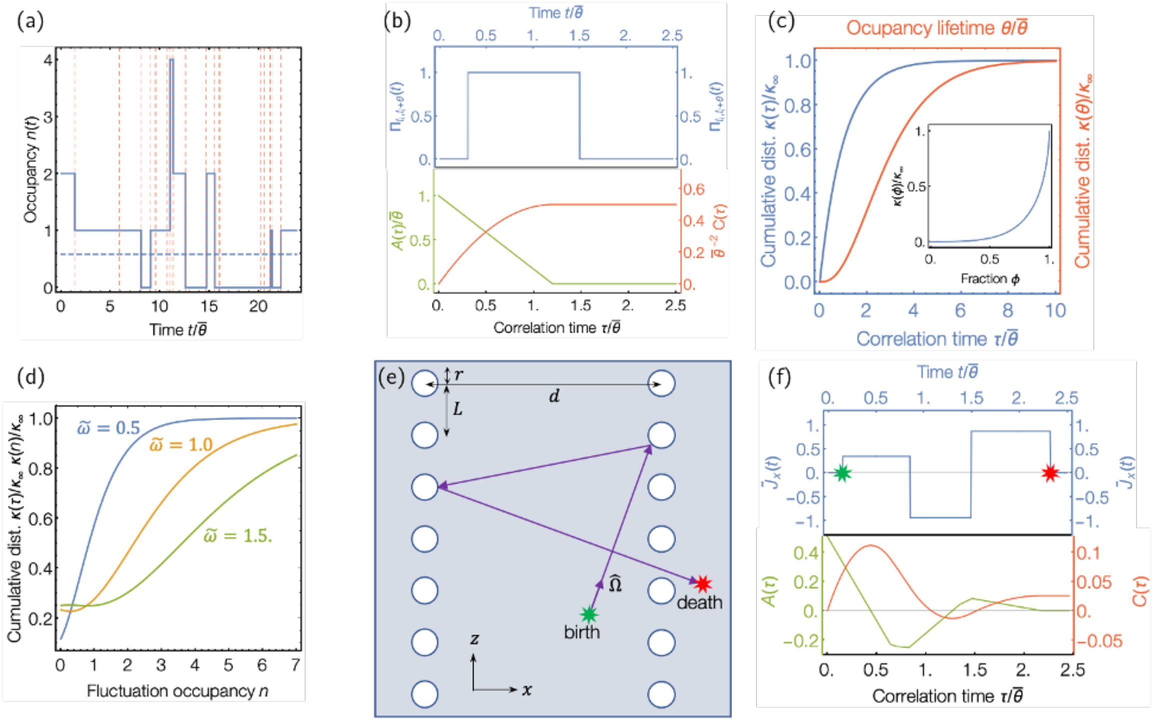

Figure 2.3: (a) Example of the random occupancy fluctuations in a phonon mode with dimensionless frequency $\widetilde{\omega} = 1.0$ and mean scattering lifetime $\overline{\theta}$. (b) Example of a single occupancy fluctuation in time (top pane) and its autocorrelation (green) and integral (red) in the bottom pane. (c) the cumulative conductivity distribution over the Green-Kubo heat flux autocorrelation time (blue) and the cumulative conductivity distribution over the fluctuation duration (red). The inset plot shows the cumulative conductivity distribution $\kappa(\phi)/\kappa_\infty$ over the fraction of fluctuations ranked in ascending order of longevity. (d) Cumulative conductivity distribution over fluctuation magnitude. The blue, gold and green lines are for $\widetilde{\omega} = 0.5,\ 1.0$ and $1.5$, respectively (or $\langle n \rangle = 0.15,\ 0.51$ and $1.1$. (e) Schematic of a phonon wave packet's trajectory in nanoporouse Si. The wave packet is spawned as the result of anharmonoic phonon-phonon interactions at location p traveling initially along direction $\hat{\Omega}$, and in this case is scattered elastically twice from pores before its annihilation through another phonon-phonon interaction. (f) The top pane shows the contribution to heat flux in the x direction from the wavepacket in (e) (blue). The bottom pane shows the corresponding heat flux autocorrelation function and its integral plotted in green and red, respectively.

where $\langle n_{\mathbf{k}p} \rangle$ is the Bose-Einstein occupancy

$$\langle n_{\mathbf{k}p} \rangle = \frac{1}{e^{\widetilde{\omega}_{\mathbf{k}p}} - 1}, \tag{2.24}$$

and $\widetilde{\omega}_{\mathbf{k}p}$ is the dimensionless mode frequency $\widetilde{\omega}_{\mathbf{k}p} = \frac{\hbar\omega_{\mathbf{k}p}}{k_B T}$. The total instantaneous heat flux is then the sum of contributions from all modes,

$$\mathbf{J}(t) = \sum_{\mathbf{k}p} \mathbf{J}_{\mathbf{k}p}(t) = \sum_{\mathbf{k}p} \left(n_{\mathbf{k}p}(t) - \langle n_{\mathbf{k}p} \rangle\right) \frac{\hbar\omega_{\mathbf{k}p}\nu_{\mathbf{k}p}}{V}. \tag{2.25}$$

where the mean flux from pairs of modes with opposite **k** has canceled one another so that the net flux only depends on the sum of occupancy excursions from the mean. If the occupancy fluctuations in one mode are uncorrelated with the fluctuations in the other modes then when expanding the product of the sum of modal fluxes, the cross-correlations between modes will be zero simplifying the total correlation function to the sum of autocorrelation functions for each mode individually:

$$\left\langle \mathbf{J}(t) \bigotimes \mathbf{J}(t+\tau) \right\rangle = \sum_{\mathbf{k}'p} \sum_{\mathbf{k}p} \left\langle \mathbf{J}_{\mathbf{k}'p'}(t) \bigotimes \mathbf{J}_{\mathbf{k}p}(t) \right\rangle = \sum_{\mathbf{k}p} \left\langle \mathbf{J}_{\mathbf{k}p}(t) \bigotimes \mathbf{J}_{\mathbf{k}p}(t+\tau) \right\rangle \tag{2.26}$$

This, in turn, depends only on the autocorrelation of the occupancy fluctuations

$$\left\langle \mathbf{J}_{\mathbf{k}p}(t) \bigotimes \mathbf{J}_{\mathbf{k}p}(t+\tau) \right\rangle = \left(\frac{\hbar\omega_{\mathbf{k}p}}{V}\right)^2 \nu\nu_{\mathbf{k}p} \left\langle \left(n_{\mathbf{k}p}(t) - \langle n_{\mathbf{k}p} \rangle\right) \left(n_{\mathbf{k}p}(t+\tau) - \langle n_{\mathbf{k}p} \rangle\right) \right\rangle, \tag{2.27}$$

where the shorthand notation $\nu\nu_{\mathbf{k}p} = (\nu_{\mathbf{k}p} \bigotimes \nu_{\mathbf{k}p})$ has been used for the tensor product of the group velocity.

The occupancy $n(t)$ of a phonon mode will be a random stepped function in time as shown in Fig. 2.3(a) with phonon mode holding a constant excitation for some duration before anharmonic interactions with other phonon modes lead to scattering and a reset of the mode's excitation. This function can be expressed as a sum of boxcar functions that represent the occupancy during the interval between successive scattering events

$$n(t) = \sum_{i=1}^{\infty} n_i \Pi_{t_i, t_i+\theta_i}(t), \tag{2.28}$$

where $\Pi_{a,b}(t)$ is the boxcar function (plotted in blue in the top pane of 2.3(b)

$$\Pi_{a,b}(t) = \begin{cases} 1 & \text{for } a \leq t < b \\ \\ 0 & \text{otherwise} \end{cases} \tag{2.29}$$

and $n_i$ and $\theta_i$ are the size and duration of the $\mathrm{i}^{\mathrm{th}}$ occupancy fluctuation, and the fluctuations abut one another so that $\theta_i = t_{i+1} - t_i$.

If the probability of the $\mathrm{i}^{\mathrm{th}}$ occupancy $n_i$ and its duration $\theta_i$ are independent from the fluctuations that proceeded it (as in the figure above), then the occupancy is only correlated during the intervals between scattering and so the occupancy correlation function reduces to simply the average of the correlation functions for each excursion with itself

$$\langle (n(t) - \langle n \rangle)\,(n(t+\tau) - \langle n \rangle) \rangle = \sum_{n=0}^{\infty} \int_0^{\infty} d\theta' P_{\overline{\theta}}(\theta') R_n (n - \langle n \rangle)^2 A(\tau, \theta'), \tag{2.30}$$

where the subscripts have been dropped temporarily for clarity. Here, $R_n$ is the average rate of scattering events that leave the mode with occupancy $n$, and $P_{\overline{\theta}}(\theta)$ is the probability that a fluctuation of occupancy $n$ survives for time $\theta$ before scattering given that the average duration of fluctuations is $\overline{\theta}$. The term $A(\tau, \theta)$ is the autocorrelation function of a single boxcar function

$$A(\tau, \theta) = \int_0^{\infty} dt' \Pi_{a,a+\theta}(t') \Pi_{a,a+\theta}(t' + \tau) = \theta \left(1 - \frac{\tau}{\theta}\right) H(\theta - \tau) \tag{2.31}$$

with $H(x)$ is the Heaviside theta function. The integral of the boxcar's autocorrelation function is

$$C(\tau, \theta) = \int_0^{\infty} d\tau' A(\tau', \theta) = \left(\theta\tau - \frac{\tau^2}{2}\right) H(\theta - \tau) + \theta^2 (1 - H(\theta - \tau)). \tag{2.32}$$

The upper pane of Fig. 2.3.b shows the boxcar function for a single fluctuation, with the lower pane showing its autocorrelation function and integral. The integrated ACF converges to

$$C(\infty, \theta) = \frac{1}{2}\theta^2. \tag{2.33}$$

If the scattering processes that lead to the occupation fluctuations are random, then occupation times $\theta$ are drawn from the Poisson distribution of waiting times

$$P_{\overline{\theta}}(\theta) = \frac{1}{\overline{\theta}} e^{-\theta/\overline{\theta}}. \tag{2.34}$$

The rate, $R_n$, of scattering into occupancy $n$ is related to the thermodynamic probability $P_n$ of finding the mode in its $\mathrm{n}^{\mathrm{th}}$ state of occupancy by

$$R_n = \frac{P_n}{\overline{\theta}}, \tag{2.35}$$

where $P_n$ is the probability distribution for the canonical ensemble

$$P_n = e^{-n\widetilde{\omega}}\left(1 - e^{-\widetilde{\omega}}\right). \tag{2.36}$$

Using Eq. 2.34–2.36 in 2.30 and performing the integral over lifetimes and summing over $n$ gives:

Performing the averaging over all possible occupancies gives

$$\langle (n(t) - \langle n \rangle)(n(t+\tau) - \langle n \rangle) \rangle = \frac{1}{\overline{\theta}} \frac{e^{\widetilde{\omega}}}{(e^{\widetilde{\omega}} - 1)^2} \int_0^\infty d\theta' A(\tau, \theta) e^{-\theta'/\overline{\theta}}, \tag{2.37}$$

and averaging over all possible fluctuation durations gives

$$\langle (n(t) - \langle n \rangle)(n(t+\tau) - \langle n \rangle) \rangle = \frac{e^{\widetilde{\omega}}}{(e^{\widetilde{\omega}} - 1)^2} e^{-\theta'/\overline{\theta}} \tag{2.38}$$

The cumulative thermal conductivity tensor is then

$$\kappa(\tau) = \frac{V}{k_B T^2} \sum_{\mathbf{k}p} \left(\frac{\hbar \omega_{\mathbf{k}p}}{V}\right)^2 \frac{e^{\widetilde{\omega}}}{(e^{\widetilde{\omega}} - 1)^2} \nu \nu_{\mathbf{k}p} \int_0^\tau d\tau' e^{-\tau'/\overline{\theta}_{\mathbf{k}p}}, \tag{2.39}$$

which after some mathematical manipulation simplifies to

$$\kappa(\tau) = \sum_{\mathbf{k}p} \left( \frac{\hbar\omega_{\mathbf{k}p}}{V} \frac{d\langle n_{\mathbf{k}p} \rangle}{dT} \right) \nu\nu_{\mathbf{k}p} \overline{\theta}_{\mathbf{k}p} \left( 1 - e^{-\tau/\overline{\theta}_{\mathbf{k}p}} \right). \tag{2.40}$$

The first term in parenthesis is the mode's volumetric specific heat. If the phonon modes all have the same scattering rate and group velocity and assuming cubic symmetry, the first element of the thermal conductivity tensor reduces to the well-known result from kinetic theory:

$$\kappa_{xx}(\infty) = \frac{1}{3} C_v \overline{\nu}_g \lambda. \tag{2.41}$$

where $C_v$, $\overline{\nu}_g$ and $\lambda$ are the systems volumetric specific heat, group velocity, and mean free path. This result shows that in order to understand the HCACF and the reduction in thermal conductivity we need only consider just the autocorrelation of individual occupancy fluctuation or phonon wavepackets by themselves, and thus provides the formal theoretical footing for the ray tracing model that follows. Before moving on to the ray tracing model, however, we make note of several insights that can be obtained from the analysis above.

The correlation function in Eq. 2.38 decays (and the cumulative conductivity in Eq. 2.39) exponentially over a correlation time equal to the mean phonon scattering time $\overline{\theta}$, so is all modes have the same lifetime the cumulative thermal conductivity distribution over *correlation* time $\tau$ is

$$\frac{\kappa(\tau)}{\kappa_\infty} = 1 - e^{-\tau/\overline{\theta}}. \tag{2.42}$$

This masks the importance for the transport of heat of long-lived occupancy fluctuations in the tail of the Poisson distribution of lifetimes. As can be seen from Eq. 2.33, the contribution that occupancy fluctuations make to the thermal conductivity is proportional to their lifetime squared, and so we can compute the cumulative thermal conductivity distribution over phonon *lifetimes* as

$$\frac{\kappa(\theta)}{\kappa_\infty} = \frac{\int_0^\theta d\theta' \theta'^2 P_{\overline{\theta}}(\theta')}{\int_0^\infty d\theta' \theta'^2 P_{\overline{\theta}}(\theta')} = 1 - \frac{1}{2}\left(2 + \frac{\theta}{\overline{\theta}}\left(2 + \frac{\theta}{\overline{\theta}}\right)\right) e^{-\theta/\overline{\theta}}. \tag{2.43}$$

Both Eq. 2.42 and 2.43 are plotted in Fig. 2.3(c) where it can be seen that the short-lived fluctuations (small $\theta$) contribute very little to the thermal conductivity while the cumulative conductivity distribution in $\tau$ rises rapidly at small correlation times. This illustrates the conceptual difference between fluctuation duration $\theta$ and correlation time $\tau$; the change in $\kappa(\tau)$ at correlation time $\tau$ includes contributions from all fluctuations with $\theta > \tau$. It is common in heat transport texts to see plots of the cumulative contribution to thermal conductivity over the distribution of phonon modes' mean free paths in a crystal $\kappa(\lambda)$, and so we take pains here to point out that the $\kappa(\theta)$ distribution in Fig. 2.3(c) is due to the shot noise in a mode with average scattering rate $\overline{\theta}$, it is not from a distribution different $\overline{\theta}$ over different modes. However, the effect of this noise is significant, with a large contribution to the total conductivity coming from a small number of phonons that travel ballistically over distances many times longer than the *mean* free path before scattering. This point is further emphasized by computing the cumulative conductivity distribution over the fraction $\phi$ of occupancy fluctuations ranked in ascending order of their longevity,

$$\frac{\kappa(\phi)}{\kappa_\infty} = \phi - (1-\phi)\ln(1-\phi)\left(1 - \frac{1}{2}\ln(1-\phi)\right), \tag{2.44}$$

as is plotted in Fig. 2.3(d). In fact, more than 50% of the heat transported is carried by just 7% of phonons that survive for more than 2.7 times the average phonon lifetime $\overline{\theta}$. It can also be seen that 80% of the heat current comes from fewer than 20% of the phonon mode occupancy fluctuations. This matches Pareto's 80-20 rule that is a signature of Lévy flights, although in this case, the distribution of flight lengths is not fractal (power-law), and so this behavior is not a true Lévy flight. The outsized importance of the long-lived phonons is significant as it implied that ballistic effects for heat transport in nanoscale systems should become significant at system sizes significantly larger than the phonons' nominal mean free path. This observation also has important ramifications for deterministic simulations of the Boltzmann transport equation (BTE) for phonons, implying that to correctly predict the heat conduction due to phonon transport in nanostructured material, one must smear the intrinsic distribution of average phonon lifetimes by the Poisson distribution—a practice that is often overlooked in frequency-dependent and multi-grey BTE simulations [Jackson, Giuseppe].

In addition to computing the contribution from different occupancy durations, it is also insightful to consider the cumulative distribution contribution from different occupancy

$$\frac{\kappa(n)}{\kappa_\infty} = \sum_{n'=0}^{n} P_{n'}(n' - \langle n \rangle)^2 \Big/ \sum_{n'=0}^{\infty} P_{n'}(n' - \langle n \rangle)^2, \tag{2.45}$$

as plotted in Fig. 2.3(e) with values for $\varpi$ of 0.5, 1.0, and 1.5 (which corresponds to average occupancies of $\langle n \rangle$ of 0.16, 0.58, and 1.1). It can be seen that because of the $(n - \langle n \rangle)^2$ dependence on the ACF infrequency multiple phonon excitations of the modes account for a large fraction of the heat carried, even at temperatures where $\langle n \rangle \sim 0.5$. This suggests that scattering processes involving four or more phonons, although rare, will have a significant impact on the overall thermal conductivity, even at low temperatures.

### 2.4.1 RAY TRACING MODEL

It is difficult to infer the phonon scattering behavior that gives rise to the anti-correlation in HCACF directly from the shape of the HCACF curve. To circumvent this difficulty, we have developed a Monte Carlo phonon ray tracing model which allows us to test how different scattering behavior that could be occurring at pores would be manifest in the HCACF, allowing us to seek signatures of different scattering phenomena in the HCACF obtained from the MD simulations. Phonon ray tracing models have been used to great effect by several other researchers to identify signatures of ballistic transport in a variety of nanoscale geometries. What sets our use of the ray tracing model apart is that rather than using it to predict thermal transport, we use it to construct the heat current autocorrelation function.

#### Monte Carlo Ray Tracing Model of Correlated Scattering

To isolate the effects that arise from correlated scattering we study a simpler model system consisting of a grey population of phonons in which we assume that all phonon modes have the same frequency $\omega$, group velocity $\nu_g$, and mean intrinsic scattering lifetime $\overline{\omega}$. The derivation above shows that the HCACF can be constructed by considering each correlated heat carrier event in isolation and then averaging their contribution to the total HCACF. For a wavepacket scattered elastically from one mode (with wavevector $\mathbf{k}$ and polarization $p$) into another mode ($\mathbf{k}'p'$) by an interface, one must consider the flight of both the incident wavepacket and the scattered wavepacket together as the occupancy fluctuations in $\mathbf{k}p$ and $\mathbf{k}'p'$ modes are now (anti)correlated. This is true even in the case of diffuse scattering, where the choice of the scattered $\mathbf{k}'$ mode is independent of the incident mode, as after scattering the *sign* of the velocity component perpendicular to the interface is reversed, making heat flux in that direction after scattering anticorrelated with the flux before scattering. As we now have to consider the sequential occupancy of two or more modes, rather than compute the occupancy auto- and cross-correlations of the modes we instead consider the heat current from individual wavepackets of lattice vibration, starting from their birth, and following them as they are scattered elastically through a series of different phonon modes, up until the uncorrelated phonon-phonon scattering event that causes their annihilation. An example of such a trajectory is shown in Fig. 2.3(e) with the resulting heat flux along x and its autocorrelation function shown in Fig. 2.3(f).

In using this conceptually subtly different approach of following wavepackets rather than occupancy fluctuations, we can apply some of the insights from the derivation above to write the autocorrelation function of the heat current fluctuations along the x direction as the average of the heat flux autocorrelation functions of wavepackets with unit magnitude

$$\langle J_x(t)J_x(t+\tau) = \frac{D}{V\overline{\theta}}\frac{e^{\widetilde{\omega}}}{(e^{\widetilde{\omega}}-1)^2}(\hbar\omega\nu_g)^2\langle A_{xx}(\tau,\theta,\mathbf{r},\widehat{\Omega})\rangle, \tag{2.46}$$

where $D$ is the density of states (the number of phonon modes per unit volume), and $A_{xx}(\tau,\theta,\mathbf{r},\widehat{\Omega})$ is the autocorrelation function of the heat flux along x created by a unit wavepacket that was born at location $\mathbf{r}$, traveled initially along direction $\overline{\theta}$, and lived for duration $\theta$, before being annihilation into the phonon bath. The total thermal conductivity reduction can thus be computed as:

$$\frac{\kappa(\tau)}{\kappa_{\text{bulk}}} = \frac{3}{\overline{\theta}^2}\int_0^\tau d\tau'\langle A_{xx}(\tau',\theta,\mathbf{r},\widehat{\Omega})\rangle = \frac{3}{\overline{\theta}^2}\langle C_{xx}(\tau,\theta,\mathbf{r},\widehat{\Omega})\rangle. \tag{2.47}$$

As this population phonons are in a volume that includes physical scattering centers such as pores and inclusions, in addition to averaging over the phonon lifetimes $\theta$, the average $\langle A_{xx}(\tau', \theta, \mathbf{r}, \widehat{\Omega})\rangle$ is also taken over the spatial domain $\mathbf{r}$, the phonon modes $\widehat{\Omega}$, and the various possibilities for the reflected wave packet at each correlated scattering events.

Rather than perform the average in Eq. 2.47 analytically, we average using Monte Carlo sampling – tracing the trajectory of wavepackets as they collide with pores and are scattered off into new directions. In this scheme we took the average HCACF from 20,000 randomly sampled wavepacket trajectories; each beginning from a randomly selected starting point, with random initial direction, and with a lifetime drawn randomly from the Poisson distribution. The single wavepacket HCACFs in the x, y, and z directions were computed numerically out to a correlation time of 20 times the mean scattering time $\widehat{\Omega}$ to prevent truncation of contributions from long-lived phonons in the tails of the Poisson distribution. This averaging was sufficient to reduce the uncertainty in the computed values of $\kappa_{\text{bulk}}$ to $< 3\%$. The details of how the correlated scattering from pores was modeled are described in the next section.

### Pore Scattering Models

The HCACF from the MD simulations of material containing cylindrical pores shows a single pronounced region of anticorrelation. The correlation time at which the HCACF is most negative changes with the distance d between the ranks of pores but is characterized by single effective velocity $\nu_{dip}$ which is found to be less than half of the averaged acoustic phonon velocity. Finally, the anti-correlation effect can be very large, with the final thermal conductivity of the material containing pores $\kappa_{\infty}$ being as little as 20% of

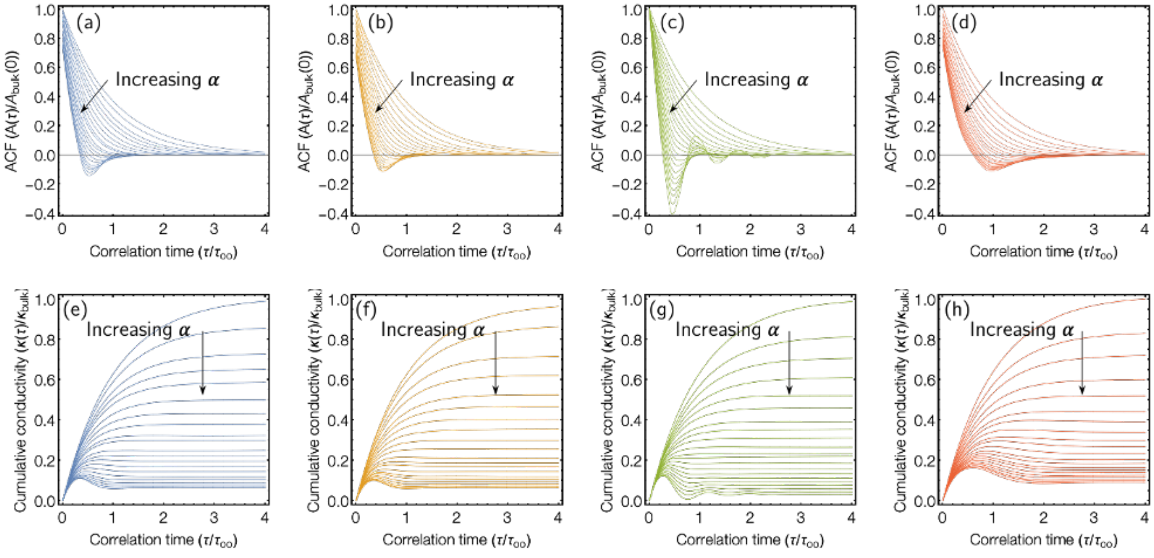

Figure 2.4: Plots of the HCACF (top row), and corresponding cumulative thermal conductivity (bottom row), for the four scattering models. The specular and diffuse palisade models are plots in blue (a & e) and gold (b & f), respectively, while specular and diffuse wall models are plotted in green (c & g) and red (d & h), respectively. All plots are for simulations with $K_n = 2.5$, and the geometric scattering probability $\alpha$ is swept from 0 to 1. In the top row, the HCACF is plotted normalized by $A_{bulk}(0) = 1/3(v_g\tau_o)^2$, the initial value of the HCACF in the bulk crystal. Similarly, on the bottom row the cumulative thermal conductivity is normalized by the thermal conductivity of the bulk crystal containing no extrinsic scattering centers.

the peak cumulative thermal conductivity, $\kappa_{peak}$. This implies that the motion of phonons after scattering, on average, undoes 80% of the heat conduction by the phonons before they were scattered from the pores. With the ray tracing model, we aim to understand what factors in the scattering of phonons from pores affect these three factors: single vs multiple anticorrelation, $\nu_{dip}$, and $\kappa_{peak}/\kappa_\infty$. For this, we consider the effect on the HCACF from four phenomenological models of phonon scattering from scattering centers separated by distance $L_p$ in the material. Two geometries of scattering centers are considered: an array of parallel permeable planer *walls*, and a series of *palisades* of cylindrical pores. For each geometry we examined the effect of both specular and diffuse phonon scattering by the obstacles, giving us four scattering models in total. The two geometries have a single geometric degree of freedom $\alpha$ that is related to the probability that phonons are not scattered when they encounter the wall/ palisade.

**Diffuse and specular wall scattering models** We represent the pores in MD simulation as a series of parallel planer interfaces perpendicular to the x-axis. The spacing, $L_p$, between planes is described in terms of the Knudsen number $Kn = \frac{\nu_g \bar{\theta}}{L_p}$. When a phonon encounters an interface there is a finite probability $1 - \alpha$ that it will pass through with its trajectory unaltered, otherwise, the phonon is reflected. For the specular model, reflection involves only flipping the direction of the x-component of the velocity. In the diffuse model, a new random directory is chosen in the half-space perpendicular to the reflection plane, so that the x-component of the velocity of the scattered phonon has the opposite sign from the incident phonon. Simulations were performed sweeping $\alpha$ from 0 to 1 and $\log[Kn]$ from -1 to 1. Although we refer to this model as the interface model, it is a reasonable representation of scattering from rectangular pores.

**Diffuse and Specular Palisade Scattering Models** With the palisade model we aim to more closely mimic the pore geometry simulate in the MD simulations. We assume that the material contains rows of cylindrical pores, each with radius r and aligned with their axis parallel to the y-direction. The pores are arrayed in the z-direction with spacing L to form a palisade fence. The geometry of the palisade is parameterized the parameter $\alpha = \frac{2r}{L}$ which is the scattering probability for phonons that meeting the palisade head-on. In general, the probability that phonons are scattered by the pores rather than passing between them is a function of incidence angle, $\chi$, of the phonon trajectory in the x-z plane with the x-axis. The transmission probability depends on the gap between cylinders that is visible to the phonons as they travel towards the palisade, given by

$$T(\chi) = 1 - \frac{\alpha}{|\cos\chi|}. \tag{2.48}$$

Here $\tan\chi = \nu_z/\nu_x$. The probability of transmission drops to zero at grazing angles of incidence where the shadow of the cylinder one another. Rather than models the location of cylinders explicitly we consider the probability that an incident phonon strikes a cylinder at a position with normal vector at an angle of $\beta$ relative to the phonon direction. This probability is given by $P(\beta) = \frac{\cos\beta}{\sin\beta_{\max} - \sin\beta_{\min}}$, where $\beta_{\min}$ and $\beta_{\max}$ are the limits to the possible incident angles that a phonon could strike the surface of a cylinder. If there is no shadowing $\beta_{\min} = -\pi/2$, and $\beta_{\max} = \pi/2$. Shadowing occurs at angles when $T(\chi) < 0$, and in these cases:

$$\beta_{min} = \begin{cases} \arcsin\left(1 - \frac{2\cos\chi}{\alpha}\right) & \text{for} \cos\chi\sin\chi > 0 \\ -\frac{\pi}{2} & \text{otherwise} \end{cases}, \tag{2.49}$$

$$\beta_{max} = \begin{cases} -\arcsin\left(1 - \frac{2\cos\chi}{\alpha}\right) & \text{for} \cos\chi\sin\chi < 0 \\ \frac{\pi}{2} & \text{otherwise} \end{cases}. \tag{2.50}$$

For the specular scattering model, when a phonon's x position lies on a palisade a pseudorandom number generator is used to decide if the phonon passed through the barrier unscattered or if it struck on of the pillars. If scattering occurs the incidence of a random incidence angle is selected from $P(\beta)$ and the phonon is set on a new trajectory with a new

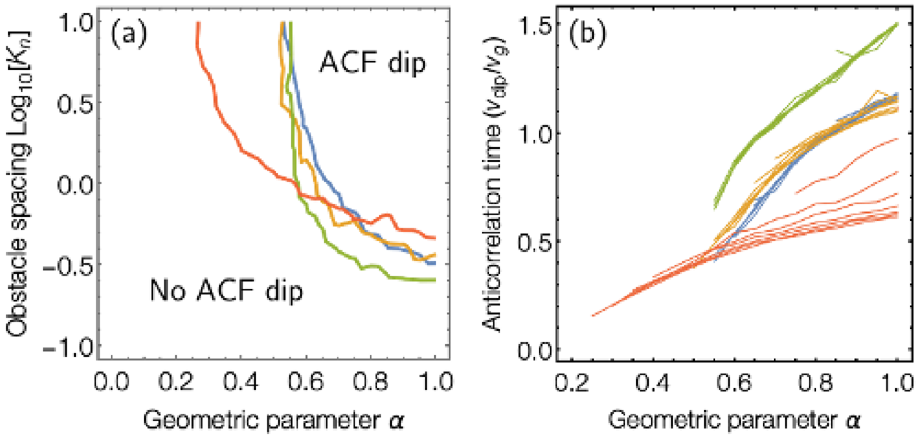

Figure 2.5: Plot (a) show the phase map in conditions of $\alpha$ and $K_n$ under which a detectable anticorrelation is observed in the HCACF for the four scattering models. The lines mark the boundary between no observed anticorrelation in the bottom left and observed anticorrelation in the top right. The phase boundaries for the specular and diffuse palisade and specular and diffuse wall scattering models are plotted in blue, gold, green and red, respectively. It can be seen that while the onset of anticorrelation in the two palisade models is within the noise of one another, the two wall scattering models are quite distinct. Plot (b) shows the time to the maximum anticorrelation for all the simulations performed, using the same color coding as in (a). The anticorrelation time, $\tau_{dip}$, is expressed in terms of the effective velocity $\nu_{dip}$, normalized by the group velocity. Each line corresponds to a sweep of $\alpha$ for different $K_n$. If can be seen that $\nu_{dip}$ is independent of the obstacle spacing for the two palisade models and the specular wall, but this is not the case for the diffuse wall. Moreover, in all cases $\nu_{dip}$ increases with increasing scatter

angle

$$\chi' = \chi + \pi - 2\beta. \tag{2.51}$$

Note that this mean-field model of scattering does not resolve the physical size of the pores and the possibility of multiple scattering between neighboring cylinders within a palisade is not considered.

The model for diffuse scattering from cylindrical pores uses the same procedure to stochastically select the normal at the point on the surface of the cylinder that the phonon strikes (this has an angle $\chi' = \chi + \pi - \beta$.). A new random direction is then selected for the

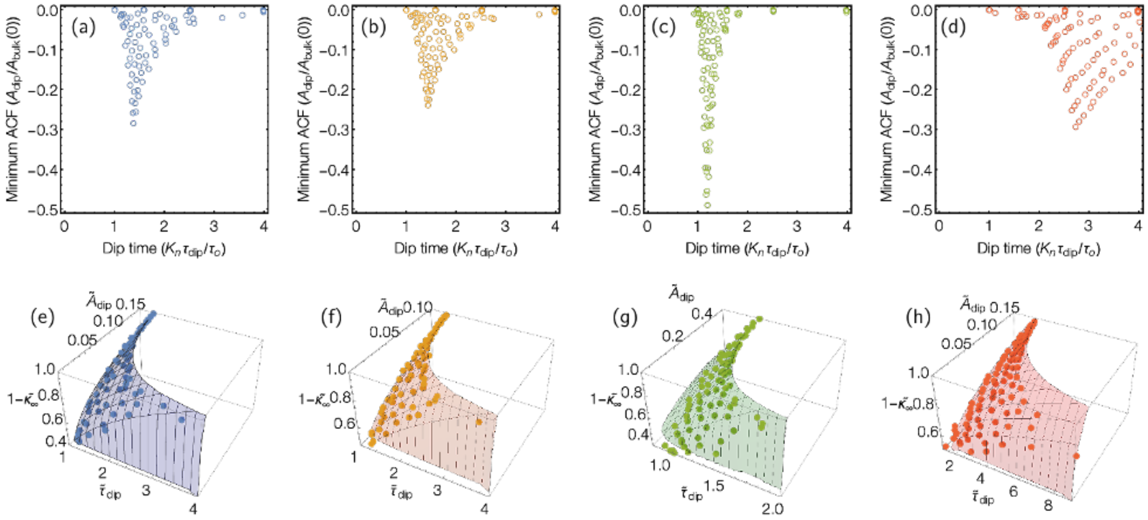

Figure 2.6: The plots in the top row shows the location (time and depth) of the minimum of the HCACF for all simulations with detectable anticorrelation. The anticorrelation time $\tau_{dip}$ is scaled buy the Knudsen number and normalized by the mean phonon lifetime. The specular and diffuse palisade and specular and diffuse wall scattering models are plotted in blue, gold, green, and red respectively (a–d). The plots in the bottom row show the time and depth of the HCACF minimum, along with the corresponding thermal conductivity reduction $1-\tilde{\kappa}_\infty$ with the same color coding as in the top row. For each scattering models all the points lie on a single manifold meaning that the location and depth of the anticorrelation is sufficient to predict the final thermal conductivity. The translucent surface in plots (e–h) shows the fit through these points as described in the main text. The manifold is different for each scattering model, providing a means of distinguishing the scattering behavior present in the MD simulations. models

phonon in the half-space defined by this normal vector.

### Discussion of Ray Tracing Model Results

The MC simulation results reveal 3 sets of key insights that help us interpret the behavior in the MD simulations.

**Qualitative differences in the HCACF anticorrelation** Plots showing the change in HCACF and corresponding cumulative conductivity as the geometric scattering probability

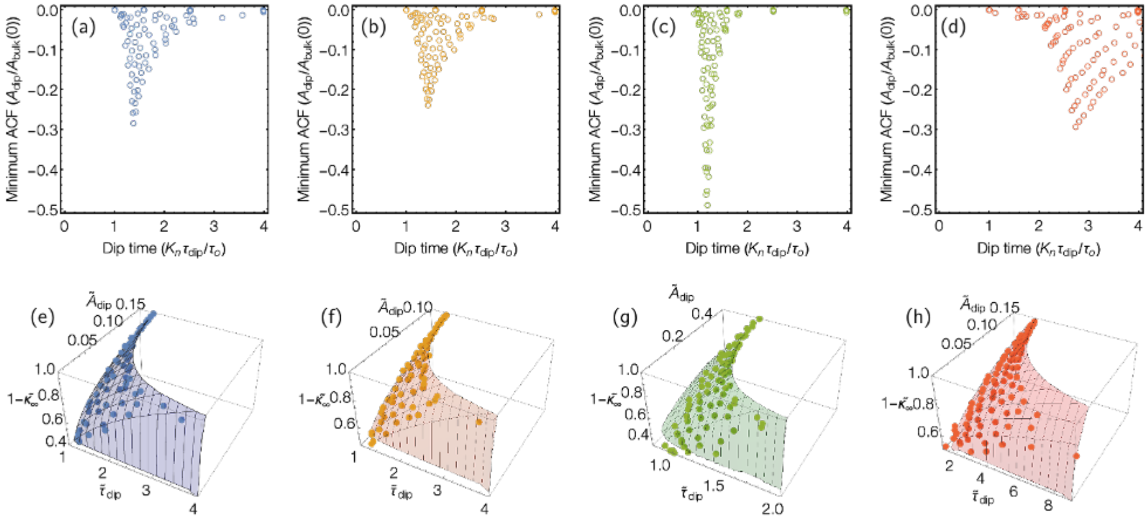

Figure 2.7: The plots in the top row shows the location (time and depth) of the minimum of the HCACF for all simulations with detectable anticorrelation. The anticorrelation time $\tau_{dip}$ is scaled buy the Knudsen number and normalized by the mean phonon lifetime. The specular and diffuse palisade and specular and diffuse wall scattering models are plotted in blue, gold, green, and red respectively (a–d). The plots in the bottom row show the time and depth of the HCACF minimum, along with the corresponding thermal conductivity reduction $1-\tilde{\kappa}_\infty$ with the same color coding as in the top row. For each scattering models all the points lie on a single manifold meaning that the location and depth of the anticorrelation is sufficient to predict the final thermal conductivity. The translucent surface in plots (e–h) shows the fit through these points as described in the main text. The manifold is different for each scattering model, providing a means of distinguishing the scattering behavior present in the MD simulations. models

parameter $\alpha$ is swept from 0 to 1 are shown in figure 2.5.

**Dependence of HCACF Anticorrelation on Scattering Geometry** The different modes of scattering at pores gives rise to different dependence of the observed heat current anticorrelation on the geometric arrangement of scattering centers.

**Quantitative Signatures of Scattering Behavior** From the HCACF at each value of $\alpha$ and $K_n$ we determine if there is a detectable region of anticorrelation, and if so, we compute the location of its minimum ($\tau_{dip}$, and $A_{dip}$) and the corresponding peak and final thermal conductivity ($\kappa_{peak}$, and $\kappa_{\infty}$).

## 2.5 Simple Formula to Predict Thermal Conductivity of Materials with Nanoscale Porosity

Prevailing nanostructuring strategies have enabled unprecedented ability to manipulate the phononic behavior of dielectrics with widespread application in thermal metamaterials ranging from microelectronic devices [53, 54] to optoelectronics [55, 56] and thermoelectrics [57, 58, 59, 60]. The extensive application of nanoengineered materials is largely because of the ability to dissociate strongly interdependent electrical and thermal behavior of dielectrics with countervailing dependence of intrinsic structural properties [61] and because of the ability to meticulously manage the heat dissipation [62, 63, 64]. Studies on nanoengineered materials including thin films [43, 44], superlattices [47, 48, 49], nanowires [42, 42], nanomesh [45, 46],nanocomposites [65, 66], and nanoporous structures [50, 51, 52] reported extremely low thermal conductivity by increasing number of surfaces that scatter phonons.

Existing nanostructuring methods mostly focus on generating multiscale lattice defects — from point defect impurities [67] to mesoscale pores [68] — to enhance the incoherent phonon scattering to limit phonons traveling distance. Recent studies on nanoporous materials showed that the judicious design of nanoscale morphology of pores can bring down the lattice thermal conductivity of dielectrics beyond their amorphous limit [69]. The consensus is that when the characteristic length of materials is about to or less than the mean free path of the phonons (better known as the Knudsen regime), phonon boundary scattering strongly detriments the lattice thermal conductivity. This behavior is known as the phonon size effect and is generally described by the Knudsen number as $Kn = \frac{\Lambda}{L_c}$. In this equation, $\Lambda$ is the phonon's mean free path and $L_c$ is the characteristic length. In materials with aligned pores, the characteristic length, $L_c$, is roughly the pore-pore distance [70] – better descriptor for $L_c$ is presented in the following sections. We note that in [71], Knudsen number is defined as the ratio of phonon mean free path and pore radius which differs from the expression we have used in this manuscript by a prefactor. The phonon size effects of pore-pore spacing, pore's misalignment, and phonon line-of-sight on lattice thermal behavior of solids containing nanoscale pores in Knudsen regime, where, $Kn \geq 1$, are widely studied in [72, 73, 74, 70, 52]. In diffusive regime, where $Kn \ll 1$, various analytical expressions, e.g., effective medium [75, 76], Hasselman-Johnson (better known as Maxwell-Garnett) [77], Maxwell-Eucken [78, 79], Rayleigh [80], Benveniste [81] and Nan [82], are articulated to study thermal conductivity of multiphase materials. These models can be used to predict the thermal conductivity of solids containing pores assuming vacuum (air) as the secondary phase. In more recent work, Minnich and Chen [83] refined Nan's mode to include phonons confinement effects ($Kn \approx 1$). Recently, Prasher [84], Machrafi et al [71] and Liu et al [85] extend models for phonons in ballistic regime ($Kn \geq 1$).

Here, we seek a simple formula to compute the lattice thermal conductivity of materials containing microscale pores. The pores are infinitely long (system size) perpendicular to the heat current and therefore the transport is planar with translational invariance vertical to the simulation surface. The simulation domain is a square unit of $L_x = L_y = L_p$

with periodic boundary condition assumed in all directions. The square comprising a single circular pore with a radius $r$ at the center of the unit so that the radius of the pores is $r = L_p\sqrt(\phi/\pi)$, where $\phi$ is the porosity.

### 2.5.1 Descriptor

The effective thermal conductivity materials containing nanoscale pores is given by

$$\kappa_{\text{eff}}(L_c) = \int_0^\infty \mathrm{K}(\Lambda)S(\Lambda, L_c)d\Lambda, \tag{2.52}$$

where $S(\Lambda)$ is the phonon suppression function describing the scattering events at the interface of the pores for the phonon with mean free path of $\Lambda$ [86] and $\mathrm{K}(\Lambda)$ is the mean free path dependent thermal conductivity of the bulk material. In diffusive regime, for gray phonons, $S(\Lambda \to 0, L_c) \approx \frac{1-\phi}{1+\phi}$, which is in agreement with Maxwell-Garnett prediction, while in ballistic regime, $S(\Lambda \to \infty, L_c) \propto L_c^{-1}$ [87]. We remark that for a given porosity of $\phi$, the specific heat and group velocity of the porous materials change as $C(\phi) = (1-\phi)C_{bulk}$ and $\nu(\phi) = \frac{1}{1-\phi}\nu_{bulk}$ [88], and thereby the $(1-\phi)$ term in $C(\phi)$ and $\frac{1}{1-\phi}$ term in $\nu(\phi)$ are canceled out in kinetic theory expression of thermal conductivity ($\kappa \approx \frac{1}{3}C\nu\Lambda$), leaving $\Lambda$ the only parameter that $S(\Lambda, L_c)$ relies on.

Let's integrate equation 2.52 by parts

$$\kappa_{\text{eff}}(L_c) = \kappa_{\text{bulk}}\left[S(\infty) - \int_0^\infty \alpha(\Lambda)g(\Lambda)d\Lambda\right], \tag{2.53}$$

where the normalized cumulative thermal conductivity, $\alpha(\Lambda)$, is defined as

$$\alpha(\Lambda) = \frac{1}{\kappa_{\text{bulk}}}\int_0^\Lambda \mathrm{K}(\lambda)d\lambda, \tag{2.54}$$

and

$$g(\Lambda) = \frac{\partial S(\Lambda, L_c)}{\partial \Lambda}. \tag{2.55}$$

We note that

$$S(\infty) = S(0) + \int_0^\infty g(\Lambda) d\Lambda, \tag{2.56}$$

therefore, equation 2.53 turns into

$$\kappa_{\text{eff}}(L_c) = \kappa_{\text{bulk}} \left[ S(0) + \int_0^\infty g(\Lambda) \left(1 - \alpha(\Lambda)\right) d\Lambda \right]. \tag{2.57}$$

The cumulative thermal conductivity is often approximated by a logistic function in logarithmic abscissa as

$$\alpha(\Lambda) = \frac{1}{1 + \frac{\Lambda_o}{\Lambda}}. \tag{2.58}$$

Here $\Lambda_o$ is a uniparameter used to fit the logistic function to the cumulative thermal conductivity [89]. We use following form for the suppression function

$$S(\Lambda) = \frac{S(0)}{1 + \frac{\Lambda}{L_c}}, \tag{2.59}$$

where $L_c$ is the mean distance phonons travel before being scattered by pores. In derivation of this equation, it is assumed that phonon-pore scattering happens independent from the phonon-phonon scattering and therefor $\Lambda_p^{-1} = \Lambda^{-1} + L_c^{-1}$. Here, $S(0)$ is normalized diffusive thermal conductivity as $S(0) = \kappa_{\text{fourier}}/\kappa_{\text{bulk}}$. Using equations 6.11 and 6.12, equation 6.10 becomes

$$\kappa_{\text{eff}}(L_c) = \kappa_{\text{bulk}} S(0) \left[ 1 - \Lambda_o L_c \int_0^\infty \frac{1}{\left(\Lambda + \Lambda_o\right) \left(\Lambda + L_c\right)^2} d\Lambda \right], \tag{2.60}$$

which leads to

$$\kappa_{\text{eff}}(L_c) = \kappa_{\text{bulk}} S(0) \Xi(Kn), \tag{2.61}$$

where $\Xi(Kn) = \left[\frac{1+Kn(\ln(Kn)-1)}{(Kn-1)^2}\right]$. In this equation, $Kn = \frac{\Lambda_o}{L_c}$ is the Knudsen number . This equation relates the effective thermal conductivity of porous materials and Knudsen number of $Kn$ to bulk lattice thermal conductivity. Note that in diffusive regime where $Kn \ll 1$, this equation simplify to the diffusive heat conduction equation through $\kappa_{\text{bulk}} S(0) = \kappa_{\text{fourier}}$. In the remaining of this section, we describe the best descriptors for $L_c$ and $S(0)$.

### Descriptor for $L_c$

The $L_c$ shows the average interval for a free-flying phonon to collide with a boundary. Minnich and Chen defined $L_c$ as [83]

$$L_c = \frac{1}{\text{Number density of collisions} \times \text{Area of collision}} \; . \tag{2.62}$$

For cylindrical pores, equation 2.62 leads to

$$L_c = \frac{1}{\sqrt{\frac{4\phi}{\pi}}} L_p, \tag{2.63}$$

where $L_p$ is the distance between the pores. In the limit of high porosity, the mean free path of the phonons colliding with pores is expected to tend to zero, thereby Machrafi and Lebon proposed [71]

$$L_c = \frac{1-\phi}{\sqrt{\frac{4\phi}{\pi}}} L_p, \tag{2.64}$$

that differs from equation 2.63 by a factor of $(1-\phi)$ in the numerator. Liu and Huang proposed

$$L_c = (1-\phi)\lambda_i + \phi\lambda_{ii}, \tag{2.65}$$

in which, $\lambda_i$ is the geometric average of phonon's flying distance per number of collisions with the pores – proposed by Minnich in equation 2.62 – and the inter-pore distance, and $\lambda_{ii}$ is the hydraulic diameter of the pore. For the aligned cylindrical pores, the inter-pore distance is $L_p - 2r$, where $r$ is the radius of the pore, $\lambda_i = \sqrt{(L_p^2/2r)(L_p - 2r)} = L_p \sqrt{\left(\frac{1}{\sqrt{\frac{\phi}{\pi}}} - 1\right)}$, and $\lambda_{ii} = 2r = 2L_p \sqrt{\frac{\phi}{\pi}}$. We refer to their original paper for the complete list of equations for $L_c$ in materials containing pores with different shapes [85].

**Descriptor for $S(0)$**

The term $S(0) = S(\Lambda \to 0, L_c)$ is a dimensionless figure shows the effect of pores on thermal conductivity in the diffusive regime (note that in this definition we neglect ballistic effects). In this manuscript, we briefly describe three models of $S(0)$ and refer to [85, 90, 91, 92, 93] for other available expressions.

The Maxwell-Garnett's model is simply [77]

$$S(0) = \frac{1 - \phi}{1 + \phi}. \tag{2.66}$$

This is the value obtained by diffusive heat conduction using Fourier's law. Similar equation can be derived by performing angular average of the polar suppression for gray phonons [87].

The Maxwell-Eucken's model is [79]

$$S(0) = \frac{2 - 2\phi}{2 + \phi}. \tag{2.67}$$

We remark that, Nan's equation [82] for multiphase structures reduced to the same equation for the porous materials.

For cylindrical pore extended along $\hat{k}$ direction in Cartesian coordinates, the Rayleigh's model gives [80]

$$S_k(0) = (1 - \phi), \tag{2.68}$$

$$S_i(0) = S_j(0) \approx 1 - \frac{2\phi}{1 + \phi + 0.3\phi^4 + ...}, \tag{2.69}$$

and, thereby, the effective suppression function for cubic crystal structures, is $S(0) = \frac{1}{3}\sum_i S_i(0) \approx 3 - \phi - \frac{4\phi}{1+\phi+0.3\phi^4}$. Note that the Maxwell-Eucken's and Rayleigh's models give quite similar value for $S(0)$.

In this chapter, we use equations 2.63 and 2.66 to model $L_c$ and $S(0)$, respectively. Substituting equation 2.66 in equation 2.61, we will have

$$\kappa_{\text{eff}}(L_c) = \frac{1-\phi}{1+\phi}\kappa_{\text{bulk}}\Xi(Kn). \tag{2.70}$$

Similar equations can be used for structures with extended cubic and discrete spherical pores but with different $L_c$ terms of $\frac{1}{\sqrt{\phi}}L_p$ and $\frac{4}{3}L_p\sqrt[3]{\frac{3}{4\pi\phi^2}}$, respectively. Finally, we remark that for prism pores with equilateral triangle base, a better approximation for $S(0)$ and $L_c$ are $-4.37\phi^3 + 3.47\phi^2 - 2.67\phi + 1$ and $\sqrt{\phi\sqrt{3}}L_p$, respectively [85].

### 2.5.2 Model Prediction

The cumulative thermal conductivity and suppression function for GaAs at 300 K are plotted in figure 2.8(left) and 2.8(right), respectively. The blue line in figure 2.8(left) is mean free path thermal conductivity computed from first principles in *AlmaBTE*. The red line shows the logistic function with the form of equation 2.58 fitted to cumulative thermal conductivity computed using DFT. Therefore, when the feature size in GaAs-based porous materials is less than roughly 183 nm, the phonon-pore scattering dominates over the anharmonic scattering. The logistic curve predicts $\Lambda_o = 183$ nm. At the same temperature, the model prediction for $\Lambda_o$ in AlAs, InP, Ge is $\Lambda_o = 236$ nm, $\Lambda_o = 803$ nm, and $\Lambda_o =$

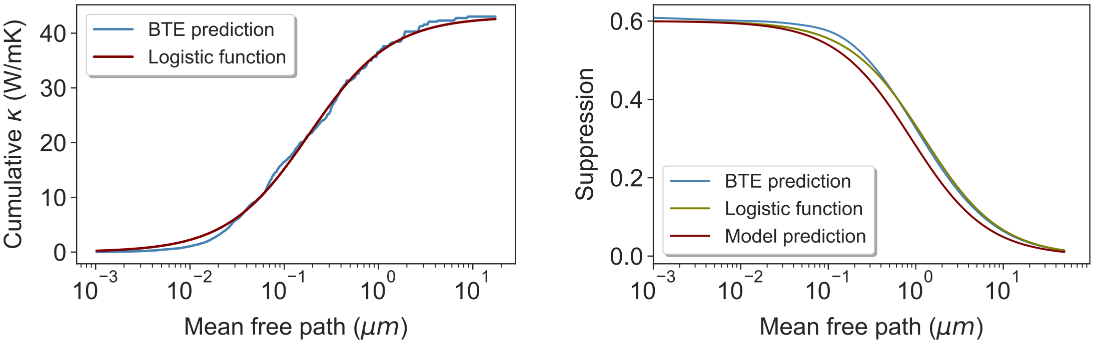

Figure 2.8: (Left) Model and first principles prediction for cumulative thermal conductivity in GaAs at 300 K in red and blue, respectively. The model predicts $\Lambda_o = 183\ nm$. (Right) The mean free path dependent suppression function from Boltzmann transport simulation in blue, logistic curve fitted to the BTE prediction in green, and model prediction in red. The logistic curve and the model predict 1.25 and 0.89 $\mu m$ line-of-sight, respectively.

296 nm, respectively. The blue curve in pane 2.8(right) shows the suppression function computed from BTE simulation using *OpenBTE*. The green plot shows the logistic curve with the form of equation 2.59 fitted to blue curve assuming that the suppression function converges to Maxwell-Garnett's diffusive model when $\Lambda \rightarrow 0$. The curve predicts $L_c = 1.25\ \mu m$. The red line shows the model prediction for the suppression function. This model predicts $L_c = 0.89\ \mu m$, slightly underestimating the feature size. We remark that, the model predictions of Machrafi (equation 2.64) and Liu (equation 2.65) estimate $L_c = 0.66\ \mu m$ and $L_c = 0.67\ \mu m$, respectively. In overall, the model prediction for cumulative thermal conductivity and the line-of-sight is in good agreement with first principles' prediction.

Figure 2.9(top-left) and 2.9(top-right) show the model and BTE predictions of lattice thermal conductivity for Si, GaAs, InAs, and Sn at 300 K for different pore-pore spacing of $L_p$ but fixed porosity of 0.25 and 0.55, respectively. The model prediction is marked with open circle while BTE simulation is marked with open triangle. The model prediction is in excellent agreement with BTE prediction for pore-pore spacing as short as 10 nm up up to macro-level spacing and for porosity up to $\sim 0.6$. For highly porous structures, the model slightly overestimates the thermal conductivity. Figure 2.9(bottom) shows the variation of thermal conductivity normalized with the bulk thermal conductivity with temperature for InP with 0.15 and 0.40 porosity plotted in blue and red, respectively. The pore spacing is fixed at $L_p = 500\ nm$. The model prediction is marked with open circle and BTE prediction is marked with triangle. The figure suggests the accuracy of the model for a wide range of temperature.

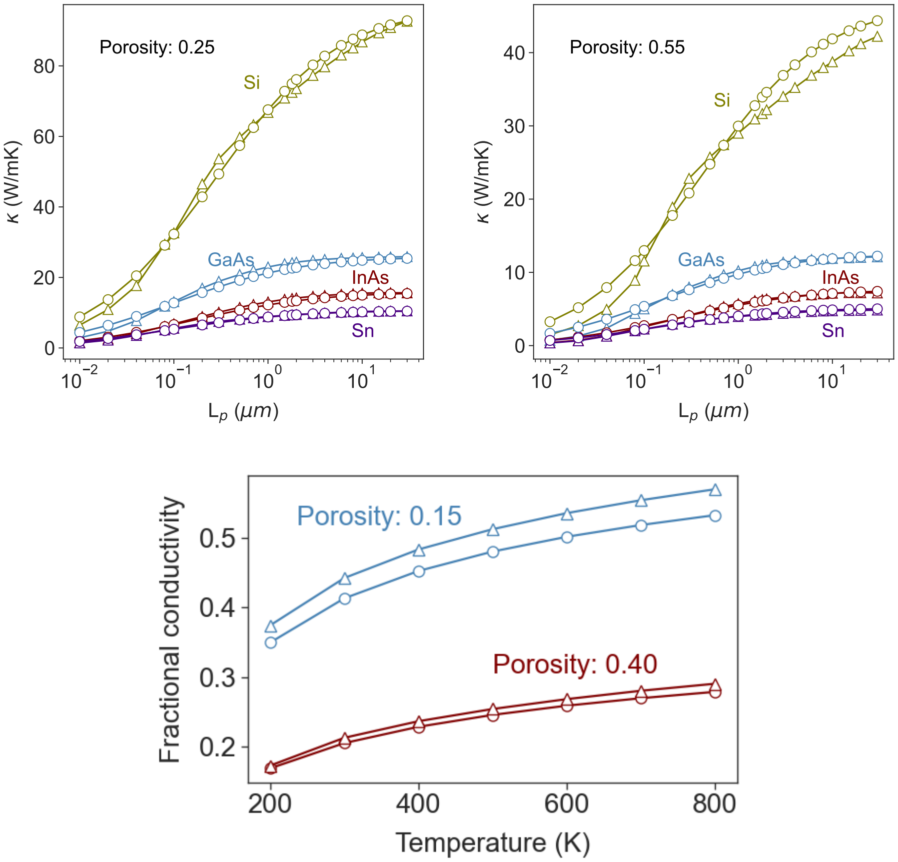

Figure 2.9: (Top)The model and BTE predictions for thermal conductivity of Si, GaAs, InAs, and Sn at 300 K for different pore-pore spacing at fix porosity of (left) $\phi = 0.25$, and (right) $\phi = 0.55$. The model prediction is marked with open circle and BTE prediction is marked with open triangle. (Bottom) The thermal conductivity of InP normalized with bulk thermal conductivity versus temperature for 0.15 and 0.40 porosity in blue and red, respectively. The pore spacing is fixed at $L_p = 500\ nm$. The model and BTE predictions are marked with circle and triangle, respectively.

# Chapter 3

# Mitigating the Effect of Nanoscale Porosity on Thermoelectric Power Factor of Si

## 3.1 Abstract

The addition of porosity to thermoelectric materials can significantly increase the figure of merit, ZT, by reducing the thermal conductivity. Unfortunately, porosity is also detrimental to the thermoelectric power factor in the numerator of the figure of merit ZT. In this manuscript we derive strategies to recoup electrical performance in nanoporous Si by fine tuning the carrier concentration and through judicious design of the pore size and shape so as to provide energy selective electron filtering. In this study, we considered phosphorus doped silicon containing discrete pores that are either spheres, cylinders, cubes, or

triangular prisms. The effects from these pores are compared with those from extended pores with circular, square and triangular cross sectional shape, and infinite length perpendicular to the electrical current. A semiclassical Boltzmann transport equation is used to model Si thermoelectric power factor. This model reveals three key results: The largest enhancement in Seebeck coefficient occurs with cubic pores. The fractional improvement is about 15% at low carrier concentration ($< 10^{20}$ 1/cm$^3$) up to 60% at high carrier population with characteristic length around $\sim 1$ nm. To obtain the best energy filtering effect at room temperature, nanoporous Si needs to be doped to higher carrier concentration than is optimal for bulk Si. Finally, in $n$-type Si thermoelectrics the electron filtering effect that can be generated with nanoscale porosity is significantly lower than the ideal filtering effect; nevertheless, the enhancement in the Seebeck coefficient that can be obtained is large enough to offset the reduction in electrical conductivity caused by porosity.

## 3.2 Introduction

In the quest to create inexpensive thermoelectric (TE) materials that can be used for harvesting low grade waste heat, researchers have identified the strategy for improving thermoelectric performance in materials such as Si by engineering nanoscale porosity [68, 73]. Nanoscale pores with a spacing smaller than the typical phonon mean free path hinder heat transfer by phonons and can produce a dramatic reduction in thermal conductivity [94]. However, although the electron mean free path is much smaller than the phonon mean free path, porosity damages the transport of low energy electrons. In this manuscript we examine strategies for designing pores so that the damage that they cause to the electrical conductivity is offset in the thermoelectric power factor (PF) by an enhancement in Seebeck coefficient. These materials are envisioned for conversion of waste heat, and so work in the temperature range of 300–700 K. Theoretical predictions suggest that at these temperatures there is significant scope for improving a materials' thermoelectric power factor through electron energy filtering, thus our approach to mitigate the effect of pores is to identify conditions under which the reduction in electrical conductivity from additional scattering of electrons by pores is offset by improvement of the Seebeck coefficient due to electron energy filtering.

The performance of thermoelectric materials at a given temperature, $T$, is quantified by the dimensionless figure of merit, $ZT = (\sigma S^2)/(\kappa_e + \kappa_l)T$, where $\sigma$ is electrical conductivity, $S$ is Seebeck coefficient, $\kappa_e$ and $\kappa_l$ are electron and lattice thermal conductivity, respectively [34]. The TE figure of merit depends on a combination of strongly interdependent electrical transport properties, that have countervailing dependence on the carrier concentration so that the overall scope for enhancing the power factor is limited. The tradeoff of these parameters is well studied, and it has become an accepted truth that optimal performance of bulk TE can be obtained in semiconductors that are highly doped to a narrow window of optimized charge carrier concentration [34].

The electrical transport properties that appear in ZT can be derived from the semiclassical Boltzmann transport equation using the single relaxation time approximation [16]. In this model, the electrical conductivity, $\sigma$, is written as

$$\sigma = -\frac{1}{3}e^2 \int \chi(E,T)\tau(E,T)dE, \tag{3.1}$$

where e is electron charge, $\tau(E,T)$ is momentum relaxation time of electrons with energy $E$ at temperature $T$ in $n$-doped semiconductors. The kernel $\chi$ includes all the intrinsic non-scattering terms and is given by

$$\chi(E,T) = \nu^2(E)D(E)\frac{df(E,E_f,T)}{dE}. \tag{3.2}$$

Here $E_f$ is the Fermi level, $\nu(E)$ the carrier group velocity, $f(E_f,E,T)$ the Fermi-Dirac distribution, and $D(E)$ is the density of states available for charge carriers. The Seebeck coefficient, $S$, in ZT describes the diffusion of electrons due to temperature gradient and is related to the difference between the average energy at which current flows and the Fermi energy level [17]. In bulk material, with negative charge carrier, the Seebeck coefficient is given by [17]

$$S = \left(-\frac{k_B}{e}\right)\left(\frac{E_c - E_f}{k_B T} + \delta\right), \tag{3.3}$$

where $k_B$, $E_c$ are Boltzmann constant and conduction band edge, respectively. The dimensionless parameter $\delta$ describes how far the average energy of the current carrying electrons is from the conduction band edge. It is defined as $\delta = \Delta_1/k_B T$, where $\Delta_1 = E_\sigma - E_c$, and $E_\sigma$ is the average energy of the charge carrier weighted by their contribution to electrical conductivity

$$\Delta_n = \frac{\int \chi(E,T)\tau(E,T)E^n dE}{\int \chi(E,T)\tau(E,T)dE}. \tag{3.4}$$

The central concept of energy filtering is to provide sources of scattering that selectively impede low energy electrons so as to increase $\Delta_1$ by reshaping product $\chi(E,T)\tau(E,T)$

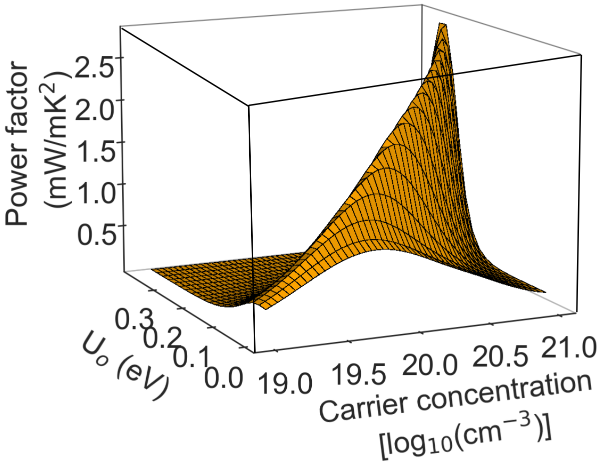

Figure 3.1: Ideal energy filtering effect in bulk P-doped silicon at 300 K. This model predicts best power performance at the tail of the Fermi distribution.

so that it is more strongly asymmetric about the fermi energy. For ideal or perfect filtering a high rate of additional scattering would be applied to all the electrons with energy lower than a certain threshold, $U_o$ so as to reduce their drift velocity to zero. The calculated change in the room temperature power factor ($\sigma S^2$) of $n$-doped silicon that would be provided by with ideal filtering is plotted in figure 3.1 as a function of filtering threshold, $U_o$, and carrier concentration (the details of this calculation are explained in the next section). The key result of this calculation is that if one can control the filtering threshold, the best power performance is to be found at high carrier concentration — ideal filtering breaks the conventional wisdom that there is a carrier concentration that provides the best compromise between conductivity and thermopower to optimize the power factor. It would provide game changing scope for enhancing thermoelectric power factor by exploiting the carrier population in the tail of the Fermi distribution. In this manuscript we examine the electron energy filtering effect provided in Si by nanoscale pores of various sizes and shapes. Our study shows while filtering by nanoscale pores are far from the ideal model, they can provide sufficient enhancement in Seebeck to countervail the degraded electrical conductivity, leaving power factor undiminished. In the sections that follow we describe electron scattering from discrete pores with different shapes, and the parameter-free semiclassical model that we use to model $n$-type Si (and its validation). Then we elucidate the effect of pores that are extended in one dimension through the entire system perpendicular to transport direction. We conclude the manuscript with a brief discussion of Lorenz number and TE performance at high temperature.

### 3.2.1 Electron Transport in Nanoporous Silicon

We used semiclassical BTE models of electrical conductivity and Seebeck coefficient to predict the strength of the filtering effect in $n$-type Si based nanoporous materials. This model is based on the intrinsic electronic band structure of undoped Silicon obtained using density functional theory (DFT). Without porosity, the scattering lifetime, $\tau$, is dominated by electron-ion and electron-phonon scattering, and the scattering rate from these two processes were modeled using equations in refs [29] and [33], respectively. The Fermi level for a given carrier concentration was computed relative to the conduction band edge and self-consistently with the DFT band structure. The electron-pore scattering term was computed using Fermi's golden rule and Matthiessen's rule was used to add the scattering rates. The detail of the calculations for bulk Si can be found in [95], here we briefly explain the arc of the model.

The terms $D(E)$, and $\nu(E)$, in function $\chi$ for Si were derived from the conduction band of Si computed with DFT using the Vienna Ab initio Simulation Package (VASP)

[19, 96, 97, 98] using generalized gradient approximation (GGA) with the Perdew-Burke-Erzerhof exchange correlation functional (PBE) [23]. Projector augmented wave (PAW) pseudopotentials is used represent the ion cores [24, 25]. The Kohm-Sham wave functions constructed using a planewave basis set with 700 eV energy cutoff. The Brillouin zone was sampled using $12 \times 12 \times 12$ Monkhorst-Pack k-point grid [26]. The forces on the atoms minimized to better than $10^{-6}$ eV/Å to relax the Si primitive cell. The electronic band structure used to compute D(E) on a $45 \times 45 \times 45$ k-point grid. The group velocity was obtained from the conduction band curvature, $\nu = \frac{1}{\hbar} |\nabla_k E|$ along the $\langle 100 \rangle$ directions on the $\Gamma$ to $X$ Brillouin zone path.

To complete the transport model, we need to define the electron lifetime, $\tau(E,T)$ in bulk Si — that is the coherence time of electrons between scattering events in bulk Si containing no pores. At moderate temperatures (room temperature), this scattering is predominated by a combination of electron-phonon and electron-ion interactions. Semiconductor TEs are generally doped to beyond the solid solubility limit (they are supersaturated) so that the carrier population is high, and the Coulomb potential is strongly screened. Therefore, we used the model developed for ions with strong screening for electron-ion lifetime [29]. In this model the transition rate has $\delta$-function form and the screening length plays a significant role. For better prediction of screening length, we used the generalized model for degenerate semiconductors [30]. We used phonon deformation potential of Ravich to model electron-phonon lifetime [33].

The final material property that appears in function $\chi$ is the Fermi level. In P-doped silicon this depends strongly on the carrier concentration, which varies non-

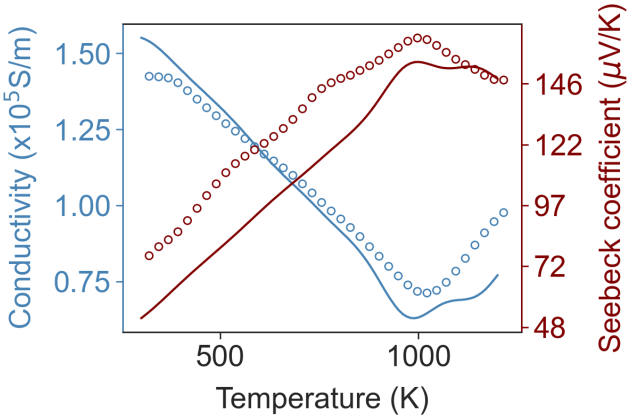

Figure 3.2: Magnitude of electrical conductivity and Seebeck coefficient in phosphorus-doped bulk silicon. The solid blue line shows the model prediction for electrical conductivity, and the red line shows the prediction for the Seebeck coefficient. The experimentally measured $\sigma$ and $S$ are marked with open circles.

monotonically with temperature as the solubility of the dopant changes. For a given carrier concentration, we used a self-consistent approach to compute $E_f$ by setting the conduction band edge as the reference frame and computing $E_f$ that gives the same carrier population in DFT computed band to circumvent the well documented problem of DFT's underprediction of electronic band gaps.

We have validated the transport model in bulk materials against a set of phosphorus-doped Si based thermoelectrics produced through a novel plasma synthesis process whose synthesis and characterization are described in ref. [95] . This reference also provides a complete description of the calculations of the electron lifetimes. The electrical conductivity and Seebeck coefficient of bulk P-doped Si is shown in figure 3.2. The experimentally measured values are marked with open circles. The minimum (maximum) in conductivity (Seebeck coefficient) is due changes in the dissolved P with temperature. Our semiclassical model has no tuning parameters and uses the experimentally measured carrier concentration at each temperature as its only input. Its predictions for conductivity and thermopower are plotted in figure 3.2 using solid lines and are a good fit to the experimental data across the full range of temperatures. The calculations were performed used a python package, *thermoelectric.py*, that we have made available for download through GitHub [99].

The band bending in the Si at the interface to a pore presents a large potential energy barrier to electron transport. The height of this barrier, $U_o$, is equal to the semiconductor's electron affinity [34]. The potential impedes transport of the low energy electrons while presenting little extra resistance to electrons in high energy states. This scattering, which occurs in addition to the intrinsic scattering from phonons and impurities, changes the electron lifetime by introducing a perturbation potential that for a single pore can be described as $U = U_o\Pi(r)$, where $\Pi(r)$ is a dimensionless boxcar function equal to unity inside the pore and zero outside of it. For uniform distribution of pores, the electron momentum relaxation time is defined as [34]

$$\tau_{np}^{-1}(s) = \frac{N}{8\pi^3}\int SR_{kk'}(1-\cos(\theta_{kk'}))dk', \tag{3.5}$$

where $N$, is the number density of pores. This is related to porosity through $N = \varphi/V_{pore}$, where $\varphi$ is the porosity and $V_{pore}$ is the average pore volume. The term $SR_{kk'}$ in equation 3.5 is the probability of transition from an initial state with wave vector $k$ and energy $E$ to a state $k'$ with energy $E'$. The $(1-\cos\theta)$ term accounts for the change in momentum that accompanies this transition, with $\theta$ the angle between initial and scattered wavevectors. For a time-invariant potential, the transition rate $SR_{kk'}$ is given by Fermi's golden rule [34, 39], $SR_{kk'} = \frac{2\pi}{\hbar}\left|M_{kk'}\right|^2\delta(E-E')$. In this expression $M_{kk'}$ is the matrix element operator that

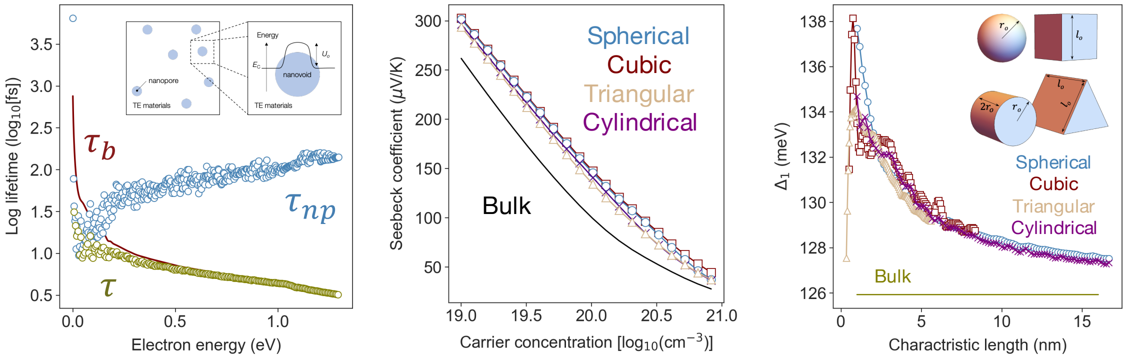

Figure 3.3: (Left) Electron lifetime in $n$-type Si at 300 K with a $10^{20}$ $1/\mathrm{cm}^3$ carrier concentration due to: (red) scattering from phonon and ions, (blue) scattering from 0.05 porosity due to spherical pores with an 8 nm diameter, and (green) the resulting total lifetime from the combination of these processes. Electron-pore scattering is dominant for electron with energy less than 140 meV. The average energy of charge flow is increased about 10 meV by adding these pores. (Middle) The maximum Seebeck coefficients with different shapes of pores. The cubic and spherical pores show the best performance, respectively. (Right) The variation of average energy of electron vs effective length for pores with different shapes but fixed porosity of $\varphi = 0.05$ at $1.2 \times 10^{20}$ $1/\mathrm{cm}^3$ concentration. The inset figure shows the four geometries examined in this work and their characteristic lengths in parenthesis. Clockwise from the top left: sphere ($l_c = 1/3r_o$), cube ($l_c = 1/6l_o$), triangular prism ($l_c = 1/(2+4\sqrt{3})l_o$), and cylinder ($l_c = 1/3r_o$).

describes the strength of the coupling between initial and final states and the number of ways that the transition between states can occur. For the Bloch waves, $M_{kk'}$ is defined as

$$M_{kk'} = \int e^{i(k'-k).r} U(r) dr. \tag{3.6}$$

For energy conservative (elastic) electron-pore scattering only transmission to eigenstates with the same energy level is possible so the Brillouin zone integral in equation 3.5 can be written as a surface integral over the isoenergetic $k$ space contour

$$\tau_{np}^{-1}(s) = \frac{N}{(2\pi)^2\hbar} \int_{E(k')=E(k)} \frac{M_{kk'}\overline{M}_{kk'}}{\nabla E(k')} (1-\cos\theta) dS(k'), \tag{3.7}$$

where $S(k')$ is the electron isoenergy state for a given wavevector. In most semiconductors isoenergy states close to the conduction valley have ellipsoid shape in momentum space that can be approximated as

$$E(k) = \hbar^2/2\left[(k_x - k_{ox})^2/(m_x^*) + (k_y - k_{oy})^2/(m_y^*) + (k_z - k_{oz})^2/(m_z^*)\right],$$

where $E(k)$, $k_o = (k_{ox}, k_{oy}, k_{oz})$, $m_x^*$, $m_y^*$, $m_z^*$ are energy level from conduction band edge, conduction band minimum, effective masses along $k_x$, $k_y$ and $k_z$, respectively. For Silicon the conduction band minimum is located at $k_o = 2\pi/a(0.85, 0, 0)$, where $a$ is the lattice parameter equal to 5.43 Å, and $m_x^* = 0.98\ m_o$, $m_y^* = m_z^* = 0.19\ m_o$ where $m_o$ is electron rest mass equal to $9.11 \times 10^{-31}$ kg [100]. We remark that in Si with narrow pore spacing confinement effect leads to flattening of conduction band [40, 41] and increase the effect mass [40], making transport coefficients different from the bulk Si. To avoid this regime, we limited our model to only consider low porosity within which the pores are far apart so that can be considered as perturbations encountered by the electronic wavefunctions of bulk Si.

In this study, we considered phosphorus doped silicon containing one of four different shaped pores: spheres, cylinders, cubes, and triangular prisms, which are shown in the inset in the right-hand plot of figure 3.3. The spherical pore has radius $r_o$, the edges of the cube are length $l_o$, the cylinder has radius $r_o$ and height $2r_o$ and all the edges of the triangular prism are $l_o$. The characteristic length (volume to surface area ratio) of these shapes are $1/3r_o$, $1/6l_o$, $1/3r_o$ and $1/(2+4\sqrt{3})l_o$, respectively. The analytic expression for the scattering matrix element, $M_{kk'}$ for each pore shape is presented in the appendix. The data for different pores' geometries is plotted using the following markers: circles for spherical pores, squares for cubic pores, triangles for triangular prism pores and × markers for cylindrical pores. In spite of the poor thermoelectric efficiency of bulk silicon due to its high thermal conductivity, it provides an excellent platform for studying the role of design parameters on transport properties, since its bulk properties are extremely well characterized [100, 14, 101].

Introducing pores into Si will not change the concentration of carrier concentration locally in the remaining Si (nor the Fermi energy), but it will change the volume averaged carrier concentration due to the reduction in the volume averaged density of states. This will impact the conductivity, and thus the effective electrical conductivity of porous materials is modeled as $\sigma_{eff} = (1 - \varphi)\sigma_{np}$. This change does not affect the Seebeck coefficient since the changes in density of states cancels out for the denominator and numerator of $S$ equation. We assumed that pores do not change the band structure of the Si — no quantum confinement effect, e.g., band flattening is considered — so we limit our study to the pores taking up 5% volume fraction — a level that is still sufficient to reduce the thermal conductivity of Si by an order of magnitude [94].

We assume that electron-pore scattering is independent of the electron-phonon and electron-ion scatterings thus Matthiessen rule can be used to sum the scattering rate from the three processes giving total scattering rate, $\tau^{-1} = \tau_b^{-1} + \tau_{np}^{-1}$, where $\tau_b$ is the electron lifetime in bulk Si because of the ionic and phononic scattering terms ($\tau_b^{-1} = \tau_{ion}^{-1} + \tau_{phonon}^{-1}$).

## 3.3 Results and Discussion

In this section we show the model prediction for the mean time between electrons being scattered by pores and demonstrate how this scattering changes the electrical behavior of nanoporous Si. The maximum power factor enhancement that can be obtained from electron filtering from nanopores is compared with that from ideal filtering. The electron scattering lifetimes due extended pores are also computed and it is shown that the electrical coefficients are insensitive to this class of pores due to limited unoccupied energy states. We conclude this section with a brief discussion of the effect of pores on electron thermal conductivity and the TE behavior of porous Si at high temperatures.

The left-hand plot in figure 3.3 shows the lifetimes in bulk Si because of the intrinsic electron-phonon and extrinsic electron-ion scattering (at $10^{20}$ 1/cm$^3$ carrier population) in red and extrinsic electron-pore scattering computed in P-doped Si containing 5% porosity due to 8 nm diameter spherical pores at 300 K in blue. The total lifetime is plotted in green. The noise in the lifetime reflects the difference in scattering rate of wavevectors around the conduction band valley minimum. Pores are the dominant scattering term for electrons with energy less than 140 meV. The central panel shows the Seebeck coefficient at different carrier concentrations for different shaped pores using the pore size that returns the largest enhancement in thermopower for that carrier concentration. The cubic pores show slightly better performance and enhanced the Seebeck coefficient up to 15% at low carrier concentrations and $\sim$ 60% at high carrier concentrations while the enhancement is limited to 12% and 30% at low and high carrier concentration regimes, respectively for spherical pores. Note than the largest enhancement in Seebeck generally takes place at medium-level concentrations ($\sim 10^{20}$ 1/cm$^3$), e.g., the largest fractional enhancement in Seebeck for cylindrical pore, occurs at $\sim 1.5 \times 10^{20}$ 1/cm$^3$ concentration. At higher temperatures, the scope for fractional improvement in Seebeck is not as dramatic but the magnitude of enhancement is still larger than 20 $\mu V/K$ — see figure 3.8 in Appendix B. The right-hand plot in figure 3.3 shows $\Delta_1$ — the average energy of the current carrying electrons — as a function of pore size at $1.2 \times 10^{20}$ 1/cm$^3$. The green line shows $\Delta_1$ in bulk Si and is equal to 126 meV. The cubic pores provide the largest $\Delta_1$ enhancement followed by spherical pores ($\Delta_1 \approx 138$ meV). This corresponds to $\sim 9.5\%$ enhancement in thermopower due to energy electron filtering — with the optimal characteristic length of the pores being 0.75 nm and 1.00 nm, respectively. The key message from the plot of $\Delta_1$ in figure 3.3 is that, at high carrier concentrations, there is only little additional return on the effort required to make pores have particular geometry — most of the benefit comes from making the pores small. This means that as a design strategy for thermopower enhancement one should seek to create pores of any shape, but to make them as small as possible. We note that the largest enhancement in $S$ does not necessarily provide the maximum power factor. For the best PF performance, the countervailing response of enhancement in $S$ and reduction in $\sigma$ should be considered simultaneously.

Figure 3.4 shows the electrical conductivity (pentagons) and Seebeck coefficient (circles) in bulk with open marker and in 5% of spherical porosity with characteristic length of 1.67 nm with close marker. The Seebeck coefficient shows around 40% increase at $1.8 \times 10^{20}$ 1/cm$^3$ while the largest degradation in conductivity is about 55% and happened at low carrier population of $3.2 \times 10^{19}$ 1/cm$^3$. The enhancement in Seebeck ($S^2$ in PF) offsets the reduction in conductivity for carrier populations beyond $10^{20}$ 1/cm$^3$. The maximum enhancement of PF is about 35% and takes place at $3.2 \times 10^{20}$ 1/cm$^3$ concentration.

The left-hand panel in figure 3.5 shows the model prediction for the variation in

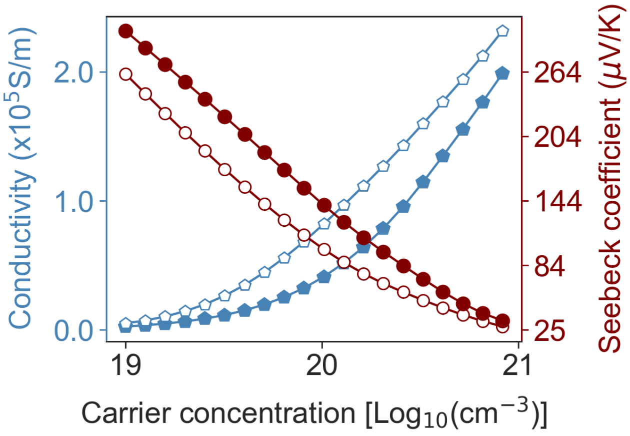

Figure 3.4: Electrical conductivity (blue) and thermopower (red) vs carrier concentration at 300 K. Open symbols are for bulk $n$-type Si. Solid symbols are for Si containing 0.05 spherical porosity with the characteristic length of 1.67 nm. The maximum enhancement in PF happens at $3.2 \times 10^{20}$ 1/cm$^3$.

largest achievable TE power factor with carrier concentration in Si based porous materials with optimal characteristic lengths at 300 K. The best power factor performance using the ideal filtering model is plotted in green. The power factor in bulk Si is plotted in black. In the narrow carrier concentration window with the highest power factor, bulk Si shows slightly better performance. The large energy difference between the conduction band edge in the Si and the vacuum level in the pore (about 4.15 eV electron affinity of bulk Si [102]) causes strong electron scattering with countervailing response of reduction in the electrical conductivity and enhancement of Seebeck coefficient that cancel out each other, leading to an overall unchanged PF value. The maximum PF in porous structures takes place at carrier concentrations higher than the optimal carrier concentration in bulk Si. This is a key insight for the design of thermoelectrics at room temperature: If one is planning to engineer porous thermoelectrics to reduce phonon conduction, then one should also plan to increase the carrier concentration above the optimal level for the bulk semiconductor. In

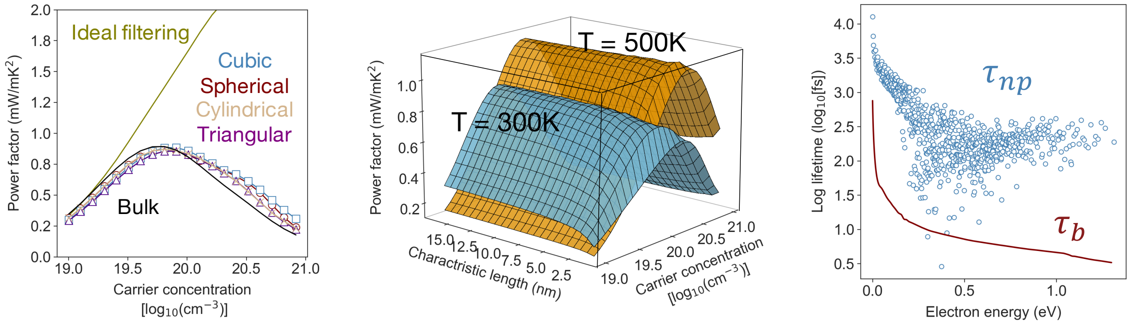

Figure 3.5: (Left) Variation in PF with carrier concentrations for pores with different shapes. The PF in bulk Si is marked with open circle in black. The largest enhancement with the ideal filtering is plotted in green. The pores with different shapes demonstrate similar behavior with reasonably good power performance. At room temperature, the maximum PF in porous structure always happens in higher carrier concentration than the carrier concentration that the bulk Si shows the best performance. (Middle) The variation in PF with pore length and carrier concentration in spherical pores at 300 and 500 K. (Right) Electron-pore lifetime for extended cylindrical pores at 300 K is plotted in blue. The characteristic length is 3.3 nm. The electron lifetime due to combination of phonons and ions is plotted in red. This is the dominant scattering term. For extended pores with low porosity, the Seebeck is similar to the bulk and the electrical conductivity is $(1-\varphi)$ of the bulk counterpart.

the Si model the maximum power factor of porous materials takes place at $8 \times 10^{19}$ 1/cm$^3$ carrier concentration and is slightly less than the maximum power factor in bulk Si occurs at $6.3 \times 10^{19}$ 1/cm$^3$, i.e., $\sim$ 25% increase in doing concentration is needed for the best performance in porous Si. The power factor in Si with spherical pores at 300 K and 500 K for different characteristic length and concentration is shown in the central panel in figure 5.5. At higher temperature of 500 K a less extreme increase in carrier concentration is needed to recuperate the power factor, and the recovery is larger. As an example, the maximum power factor of spherical pores at this temperature takes place at $1.6 \times 10^{20}$ 1/cm$^3$ carrier concentration and is slightly larger than the maximum power factor in bulk Si that takes place at $1.26 \times 10^{20}$ 1/cm$^3$ carrier concentration ($\sim$ 20% increase in doing concentration).

To complete the model of electron-pore interaction, we considered extended cylindrical with infinite length (system size) oriented along the (001) crystal axis (the z-direction is our reference system) in a P-doped silicon slab. The thermal and electrical properties of such porous Si films have been studied in [94, 103, 104], usually with the assumption that electron scattering is the same as that in bulk Si [73]. The electron lifetime of P-doped Si with extended cylindrical pores with 10 nm radius (3.3 nm characteristic length) and 0.05 porosity at 300 K is depicted in the right-hand panel of figure 3.5. This plot shows that electron-phonon and electron-ion scattering is dominant over the pore scattering by one to two orders of magnitude. The dramatic reduction in the rate of electron scattering from discrete to extended pores is due to the limited number of states that are available to accept scattered electrons. The analytic expressions for the scattering matrix elements for these extended pores are given in the Appendix A. In extended pores, scattering is only possible into states with the same component of wave vector along the pore axis. This condition, combined with the isoenergetic constraint, reduces the scattering integral to an elliptical line, drastically reducing the number of states that can participate in scattering, and means that the extended pores cause no change in the electron momentum along the axis of the pores. This result strengthens the assumption made in prior works [73, 72] that extended pores do not change the electron lifetime and thus the Seebeck coefficient of 2D nanoporous Si is the same as the bulk Si and electrical conductivity and power factor in 2D porous Si with translational invariance vertical to the simulation plane are $(1-\varphi)$ of their bulk Si counterparts.

When advocating for increased carrier concentration in thermoelectrics, it is impor-

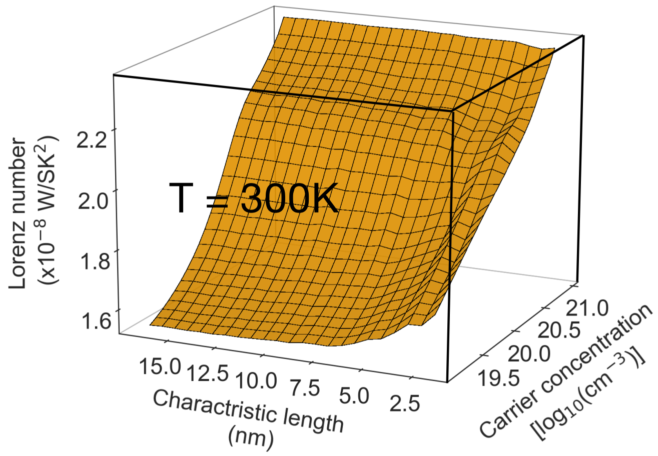

Figure 3.6: Variation of Lorenz number by the carrier concentration and characteristic length of cylindrical pores at 300 K.

tant to determine if this will cause a significant increase to the denominator of ZT. Hence, we finish our examination of the effect of pores on the room temperature electrical transport coefficients by briefly discussing the electronic thermal conductivity ($\kappa_e$). The $\kappa_e$ is related to $\sigma$ by Wiedemann Franz law as $\kappa_e = LT\sigma$. Here $L$ is the Lorenz number that conventionally varies from $2 \times (k_B/e)^2 \approx 1.48 \times 10^{-8}$ (V$^2$/K$^2$) up to $\pi^2/3 \times (k_B/e)^2 \approx 2.44 \times 10^{-8}$ (V$^2$/K$^2$) for low carrier concentration and degenerate (free electron) limit, respectively [105]. Lorenz number is related to the moments of the charge carriers, $\Delta_n$, through $L = 1/(eT)^2(\Delta_2 - \Delta_1^2)$. In bulk Si, the Lorenz number varies monotonically from $1.53 \times 10^{-8}$ (V$^2$/K$^2$) at $10^{19}$ 1/cm$^3$ to $2.39 \times 10^{-8}$ (V$^2$/K$^2$) at $10^{21}$ 1/cm$^3$. Figure 3.6 shows the variation of Lorenz number with characteristic length and carrier population in porous Si with cylindrical pores at 300 K — see figure 3.8 in Appendix B for Lorenz number in nanoporous Si with different pore shapes. While Lorenz number varies considerably with the carrier concentration it has limited dependency on pores' characteristic length especially in high carrier concentration regime. Figure 2.7 in appendix B shows the largest and the lowest changes in Lorenz number for the pores with different shapes and sizes in this study. The largest enhancements are shown with solid markers and the lowest values of the Lorenz number are shown with open markers. The Lorenz number in bulk silicon is plotted in solid black. Similar to the Seebeck coefficient, cubic pores show the largest impact on Lorenz number followed by spherical pores. Although this result is interesting, the overall impact of these changes in Lorenz number for the optimization of thermoelectric ZT will be minimal. The objective of adding porosity is to lower the lattice thermal conductivity, and prior works by Romano [94] and others [74] have shown that the lattice thermal conductivity in nanoporous Si with the geometries modeled here can be as low as $\sim 30$ W/m/K at room temperature. In bulk room temperature Si with the carrier concentration tuned to optimize ZT, the electronic thermal conductivity is $\sim 0.3$ W/m/K — still two orders of magnitude lower than the lattice conductivity.

To complete the discussion on the effect of pores on Si based porous materials we computed the transport coefficients at 1300 K (figure 3.7). The bulk properties are shown with open markers and the properties for 5% spherical pores are plotted with solid markers. Although the magnitude of power factor is larger at high temperatures the scope of PF enhancement via electron filtering is limited. Therefore, the power factor in bulk is larger than the porous Si in all ranges of carrier concentrations. The maximum PF in both bulk and porous Si takes place at $3.2 \times 10^{20}$ 1/cm$^3$ and the enhancement in Seebeck because of filtering effect mitigates up to 95% of the PF in bulk.

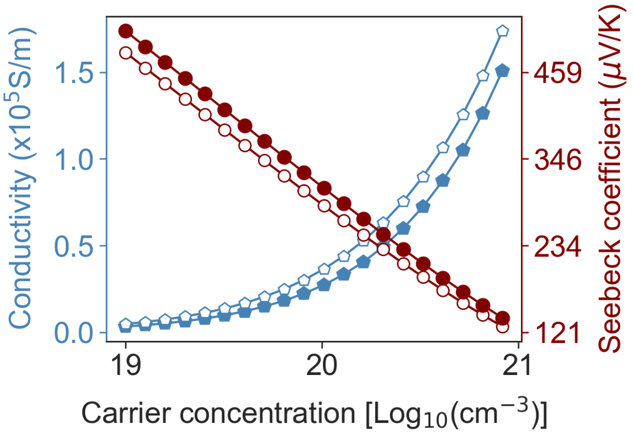

Figure 3.7: Electrical conductivity (blue) and thermopower (red) vs carrier concentration at 1300 K. Open symbols are for bulk *n*-type Si. Solid symbols are for Si containing 0.05 spherical porosity with the characteristic length of 1.67 nm. The scope of electron filtering is limited at high temperatures.

## 3.4 Conclusion

To summarize, we have used a semiclassical model to elucidate the detrimental effect that porosity has on the electrical transport properties of thermoelectric, and to devise design strategies to mitigate them. We have shown that while extended pores have little effect on electron scattering, scattering from compact pores provides an electron filtering effect that increases the Seebeck coefficient. This effect becomes more pronounced for smaller pores but is relatively insensitive to the pore geometry. We find that to take full advantage of this effect to mitigate the degradation that pores cause to thermoelectric PF one should increase the carrier concentration above the optimal level for monolithic semiconductor. In this case one can recuperate as much as 95% of the lost thermoelectric PF because of the pores. While we have focused in particular a semiclassical model of P-doped Si, as this is a model that has been experimentally validated, the findings should be transferable to other

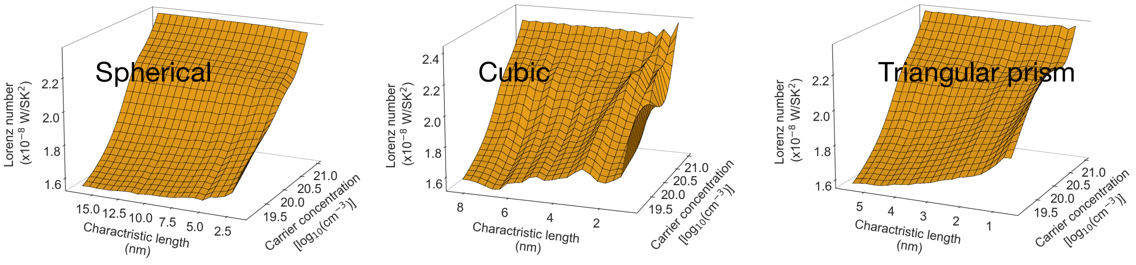

Figure 3.8: Variation of Lorenz number with carrier concentrations for spherical, cubic, and triangular prism pores with different characteristic lengths at 300 K.

semiconductors systems both $n$- and $p$- type and with either direct or indirect band gaps. While there is much focus currently on designing porosity in thermoelectrics to dramatically impede phonon transport, the results presented here form a complementary design principle for optimizing the electrical transport properties in such devices. The electrical transport properties in the numerator of ZT are less sensitive to pore shape than the phonon transport properties in the denominator. This means that a good strategy for designing nanoporous thermoelectrics that maximize ZT is to first focus on optimizing pore size and morphology to maximize phonon scattering, and then to adjust the carrier concentration to mitigate the damage to the electrical transport properties.

## 3.5 Appendix

### 3.5.1 Appendix A: Electron Matrix Elements of Pores with Different Shapes

The electron matrix element shows the strength of the coupling between initial and final wavefunctions and the number of ways the transmission may happen. For the

Bloch waves, the matrix element relies on the shape of the scattering potential. Here we present the full expression of matrix elements for pores with cubic, spherical, triangular and cylindrical shapes followed by matrix elements for different shaped extended pores.

For cubic pores with finite lengths of $l_x$, $l_y$ and $l_z$ along $x$, $y$ and $z$ direction, respectively, electron matrix element describes as

$$M_{kk'} = 8U_o \left( \frac{\sin\left(\frac{l_x q_x}{2}\right) \sin\left(\frac{l_y q_y}{2}\right) \sin\left(\frac{l_z q_z}{2}\right)}{q_x q_y q_z} \right) \tag{3.8}$$

In this equation, $q = k - k'$, and $q_x = q.\hat{i}$, $q_y = q.\hat{j}$, $q_z = q.\hat{k}$ are the projection of $q$ on Cartesian axes. In prism with isosceles triangle base, matrix element defines as

$$M_{kk'} = -4U_o l_y \left( \frac{l_x q_x - 2l_y q_y - 2l_x q_x e^{i\left(\frac{l_x q_x}{2} + l_y q_y\right)} + l_x q_x e^{i(l_x q_x)} + 2l_y q_y e^{i l_x q_x}}{l_x^2 q_x^3 - 4l_y^2 q_x q_y^2} \right) \left( \frac{\sin\left(\frac{l_z q_z}{2}\right)}{q_z} \right) \tag{3.9}$$

In this equation, $l_x$ and $l_y$ are the length and height of the triangle, respectively and $l_z$ is the height of the prism. For cylindrical potential, we have

$$M_{kk'} = 4\pi r_o U_o \left( \frac{J_1\left(r_o q_r\right)}{q_r} \right) \left( \frac{\sin\left(\frac{l_z q_z}{2}\right)}{q_z} \right) \tag{3.10}$$

In this equation, $q_r = \sqrt{(q_x^2 + q_y^2)}$, $r_o$ is the radius of the base circle, $l_z$ is the height of the cylinder and $J_1$ is the first order Bessel function of the first kind. Electron coupling matrix element for spherical potential is defined as

$$M_{kk'} = \frac{4\pi U_o}{q^2} \left( \frac{1}{q} \sin(r_o q) - r_o \cos(r_o q) \right) \tag{3.11}$$

where, $q$ is the magnitude of $\mathbf{q}$ and $r_o$ is the radius of pores. For cubic pores with infinite length (system size) along $z$, the matrix element is defined as

$$M_{kk'} = 4U_o l_z \left( \frac{\sin\left(\frac{l_x q_x}{2}\right) \sin\left(\frac{l_y q_y}{2}\right)}{q_x q_y} \right) \delta(q_z) \tag{3.12}$$

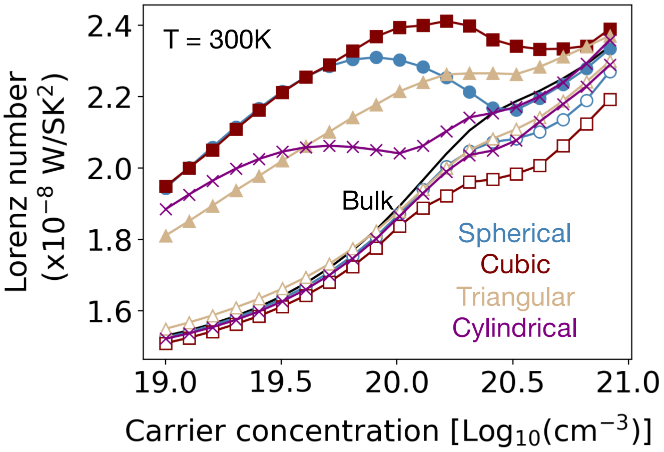

Figure 3.9: Variation of Lorenz number with carrier concentrations in bulk Si is plotted in solid black. The highest and lowest values of the Lorenz number for the pores modeled in this study are shown with solid and open markers, respectively.

For the cylindrical pore with infinite height, we have

$$M_{kk'} = 2\pi r_o U_o l_z \left( \frac{J_1\left(r_o q_r\right)}{q_r} \right) \delta(q_z) \tag{3.13}$$

For the isosceles triangular prism with infinite height matrix element is described as

$$M_{kk'} = -2U_o l_y l_z \left( \frac{l_x q_x - 2l_y q_y - 2l_x q_x e^{i\left(\frac{l_x q_x}{2} + l_y q_y\right)} + l_x q_x e^{i(l_x q_x)} + 2l_y q_y e^{i l_x q_x}}{l_x^2 q_x^3 - 4l_y^2 q_x q_y^2} \right) \delta(q_z) \tag{3.14}$$

### 3.5.2 Appendix B: The Effect of Nanopores on Lorenz Number at Room Temperature

Figure 3.8 shows changes in Lorenz number with carrier concentrations for pores with different shapes and sizes at room temperature for 5% porosity. Similar to the cylindrical pore, the Lorenz number is larger for smaller pores and the pores size has stronger effect at regimes with lower carrier populations. The maximum and minimum computed

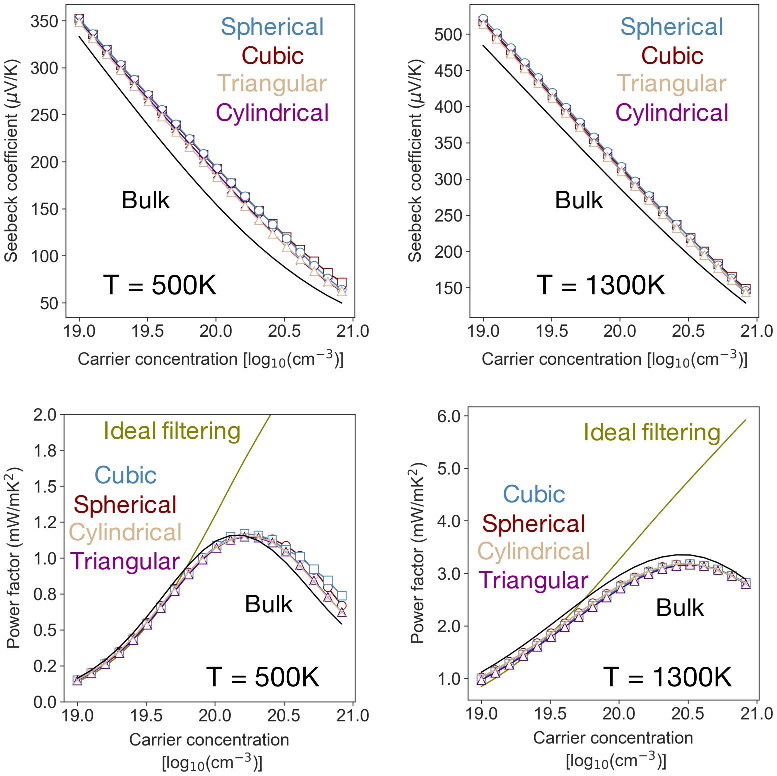

Figure 3.10: (Top) Maximum enhancement is thermopower for pores with different shapes at 500 K (left) and 1300 K (right). (Bottom) Comparison of the largest achievable PF with the filtering effect using pores with different shapes. The largest achievable PF with the filtering effect using an ideal model is plotted in green. The PF in bulk Si is shown in black. The left panel is at 500 K, and the right panel is at 1300 K.

Lorenz number and the bulk value of the Lorenz number are plotted in figure 3.9.

### 3.5.3 Appendix C: The Effect of Pores on Electrical Properties of Silicon-Based Nanoporous at High Temperatures

Figure 3.10 shows the variation of highest Seebeck (thermopower) and power factor modeled in this study with carrier concentration for pores with different shapes at 500 K and 1300 K. The bulk properties are shown in solid black lines.

# Chapter 4

# Enhanced Thermoelectric Performance of Polycrystalline $Si_{0.8}Ge_{0.2}$ Alloys through the Addition of Nanoscale Porosity

## 4.1 Abstract

Engineering materials to include nanoscale porosity or other nanoscale structures has become a well-established strategy for enhancing the thermoelectric performance of dielectrics. However, the approach is only considered beneficial for materials where the intrinsic phonon mean free path is much longer than that of the charge carriers. As such, the approach would not be expected to provide significant performance gains in polycrystalline

semiconducting alloys such as $Si_xGe_{1-x}$, where mass disorder and grains provide strong phonon scattering. In this manuscript, we demonstrate that the addition of nanoscale porosity to even ultrafine-grained $Si_{0.8}Ge_{0.2}$ may be worthwhile. The semiclassical Boltzmann transport equation was used to model electrical and phonon transport in polycrystalline $Si_{0.8}Ge_{0.2}$ containing prismatic pores perpendicular to the transport current. The models are free of tuning parameters and were validated against experimental data. The models reveal that a combination of pores and grain boundaries suppresses phonon conductivity to a magnitude comparable with the electronic thermal conductivity. In this regime, $ZT$ can be further enhanced by reducing carrier concentration to the electrical and electronic thermal conductivity and simultaneously increasing thermopower. Although increases in $ZT$ are modest, the optimal carrier concentration is significantly lowered, meaning semiconductors need not be so strongly supersaturated with dopants.

## 4.2 Introduction

The performance of thermoelectric (TE) materials depends on having both advantageous electrical transport properties, and low thermal conductivity, and is quantified by the dimensionless figure of merit, $ZT = (\sigma S^2)/(\kappa_e + \kappa_l)T$. Here $\kappa_e$ is the electrical contribution to the thermal conductivity, $\kappa_l$ is lattice thermal conductivity, $\sigma$ is the electrical conductivity and $S$ is the Seebeck coefficient (thermopower) [59, 106, 107, 108]. In materials for which the mean free path of charge carriers is much smaller than the mean free path of heat carriers (phonons), a well-established approach to increasing $ZT$ is to introduce nanoscale porosity. When tuned to the right length scale, scattering of phonons by pores can significantly reduce the heat carriers' mean free path with only minor impact on electrical transport properties in the numerator of $ZT$ [73, 72, 109]. This approach is particularly appealing because it can yield dramatic increases in energy conversion efficiency in materials such as silicon that have not traditionally been considered to be good thermoelectrics [68]. It thus opens the door for creation of energy harvesting devices that are fabricated from inexpensive, abundant, and environmentally benign materials making them intrinsically scalable. However, the approach is considered to offer little further benefit to most established high-performance thermoelectrics, such as $\mathrm{Si_xGe_{1\text{-}x}}$ alloys [34]. To achieve high $ZT$, these materials already possess one or more mechanisms for strong scattering phonons in their bulk form [110, 67, 111], and so the conventional wisdom is that there is a diminishing return on the effort and cost required to add more phonon scattering. In this manuscript, we present models of the phonon and electron transport in nanoporous $\mathrm{Si_xGe_{1\text{-}x}}$ alloys and use these to compute the full thermoelectric figure of merit as a function of the materials morphology and carrier concentration. These models show that there can be benefits to adding porosity to even good thermoelectrics such as $\mathrm{Si_xGe_{1\text{-}x}}$, and that these benefits lie not just in improved $ZT$ but also the potential for reduced cost and better tolerance to overheating and microstructural evolution.

The $\mathrm{Si_xGe_{1\text{-}x}}$ alloy system is a well-established material for high-efficiency thermoelectrics that is used in many niche applications, such as the thermoelectric generators that power deep space probes, where efficiency and reliability take precedence over cost [67]. The alloy forms a fully miscible solid solution at all values of x. The mass disorder of the randomly distributed heavy Ge atoms strongly scatters short-wavelength phonons.

Furthermore, these alloys can be fabricated from hot pressed powder compacts to create materials with ultrafine grain size. The grain boundaries provide strong scattering of long-wavelength phonons, and together, the combination of grain structure and mass disorder leading to a strong suppression of the lattice thermal conductivity and a large $ZT$. The lowest thermal conductivities occur at compositions with x $\sim$ 0.5 [46]. The electronic properties in the numerator of ZT are tuned independent of the phonon scattering by controlling the doping concentration, and to obtain the optimal power factor the doping typically must be supersaturated, which means that the thermoelectric performance of these alloys can be degraded if the material is accidentally heated to a temperature at which dopant becomes mobile and precipitates out of solution. Although Si and Ge are both non toxic, unlike the components of other widely used high efficiency thermoelectric materials (such as PbTe [112, 113] and SnSe [114, 115]), a second drawback of $\mathrm{Si_xGe_{1-x}}$ thermoelectrics is their cost. The price per mol of germanium is roughly two orders of magnitude larger than silicon, and so to reduce the expense (and expand the economic viability) of $\mathrm{Si_xGe_{1-x}}$ thermoelectrics we would like to improve the efficiency of compositions containing a relatively low Ge fraction. For this reason, in this manuscript, we focus exclusively on the $\mathrm{Si_{0.8}Ge_{0.2}}$ alloy composition.

In the sections that follow, we first describe calculations that solve the Boltzmann transport equations for phonons in polycrystalline $\mathrm{Si_{0.8}Ge_{0.2}}$ containing nanoscale extended pores with different cross-sectional shapes. The section following that presents a semiclassical model of electrical transport in *n*-type $\mathrm{Si_xGe_{1-x}}$, along with models of electron scattering by pores and grain boundaries, which were used to compute the electrical conductivity, Seebeck coefficient, and Lorenz number. The final section examines the combination of these in the $ZT$ and discusses the options available for tuning morphology and dopant to optimize it.

## 4.3 Thermal Transport in Nanoporous $\mathbf{Si_{0.8}Ge_{0.2}}$

The effective lattice thermal conductivity, $\kappa_l$, of polycrystalline $Si_{0.8}Ge_{0.2}$ containing nanoscale pores was computed by solving the frequency dependent Boltzmann transport equation [101] to find the steady state distribution of phonons moving between an array of pores under an imposed temperature gradient. The effective thermal conductivity of the material containing a given pore morphology is defined as the ratio of the heat flux carried by the phonon distribution divided by the imposed temperature gradient. These simulations were performed using the *OpenBTE* Boltzmann transport solver [116] making use of materials properties for $Si_xGe_{1\text{-}x}$ computed from first principles. The model incorporated the effects from four different phonon scattering processes: three-phonon scattering, elastic mass impurity scattering, scattering from grain boundaries, and scattering from pores. While the latter of these was modeled as physical obstacles in the simulation domain, the first three scattering processes were modeled implicitly using the single relaxation time approximation with the combined scattering rate from the three processes obtained using Matthiessen's rule.

The second and third order interatomic force constants for bulk $Si_{0.8}Ge_{0.2}$, computed with density functional theory using the virtual crystal approximation, were obtained from the *AlmaBTE* materials database [89]. The phonon dispersion was computed from the second order force constants on a $40 \times 40 \times 40$ point Brillouin zone mesh using *AlmaBTE*.

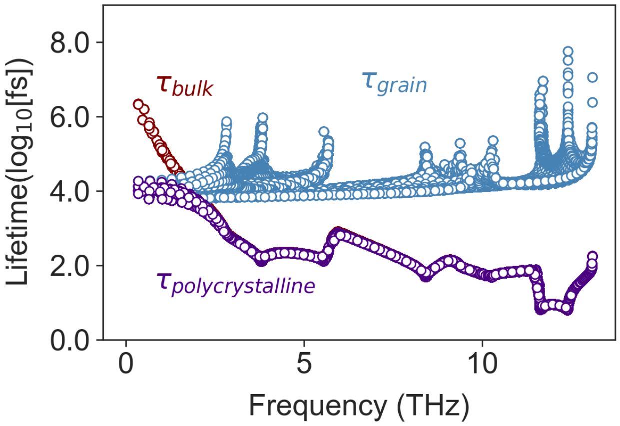

Figure 4.1: Phonon lifetimes vs frequency. The lifetime $\tau_{bulk}$ due to phonon-phonon and phonon-alloy scattering processes in single crystal $\mathrm{Si}_{0.8}\mathrm{Ge}_{0.2}$ at 500 K is plotted in red. The lifetime $\tau_{grain}$ due to grain boundary scattering in a microstructure with $l_g = 50$ nm is plotted in blue, and total lifetime in from the combination of $\tau_{bulk}$ and $\tau_{grain}$ is plotted in purple.

The scattering matrices for three phonon interactions was computed from the third order force constants also using *AlmaBTE* [117], which computes full three-phonon scattering matrix and uses it to solve linearized Boltzmann transport equation for phonons [89]. This method does not account for correlations, local relaxations or changes in electronic structure due to alloying and interatomic force constant disorder, yet gives reasonable prediction for bulk $\mathrm{Si}_{0.8}\mathrm{Ge}_{0.2}$ thermal properties [118]. The rate of elastic phonon scattering by disordered germanium atoms was modeled by treating the Ge as random mass perturbations with the scattering rate given by Tamura's formula for isotopic scattering [119]. The phonon-phonon scattering rate is temperature dependent while phonon-alloy scattering rate is temperature independent, and the phonon lifetime from their combined effect, which we refer to as $\tau_{bulk}$, is plotted in figure 4.1.

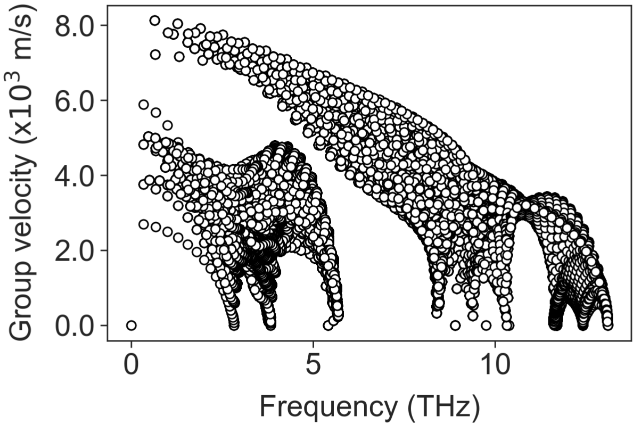

Figure 4.2: The phonon group velocity used in the calculation of $\tau_{grain}$.

The rate of scattering of phonons by grain boundaries was approximated by assuming that the average interval for a free flying phonon to collide with a boundary is $\tau_{grain} = l_g/\nu_g$, where $\nu_g$ is the phonon's group velocity and $l_g$ is an effective grain size. This model acknowledges that phonons with different wavevector and polarization have different speeds, but assumes that all phonons behave the same when they encounter a grain boundary scattering, scattering diffusely. The model is well known to slightly overestimate the thermal resistance from grain boundaries [120, 121, 122]. Figure 4.1 shows the distribution of $\tau_{bulk}$ in red, and $\tau_{grain}$ in blue, computed at 500 K for polycrystalline $\mathrm{Si_{0.8}Ge_{0.2}}$ with an effective grain size of 50 nm. The total lifetime obtained using Matthiessen's rule is plotted in purple. It can be seen that grain boundaries only dominate the scattering of acoustic phonons with frequencies lower than $\sim 2$ THz, while Umklapp and alloy scattering dominates phonons with frequencies higher than that. The phonon group velocities used in the calculation of $\tau_{grain}$ are shown in figure 4.2.

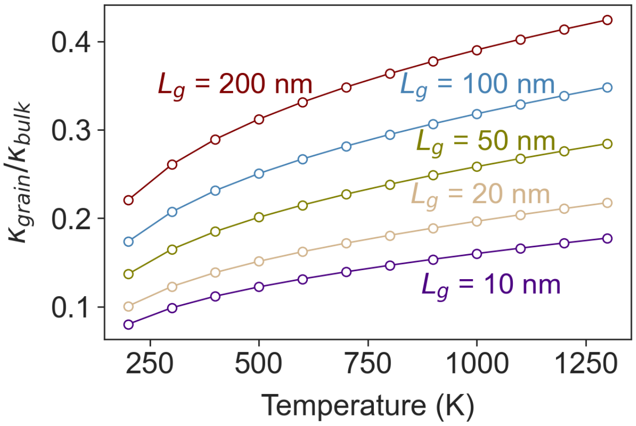

Figure 4.3: Thermal conductivity of polycrystalline $Si_{0.8}Ge_{0.2}$ relative to the conductivity of single crystal material at the same temperature. The red, blue, green, gold and purple plots are for effective grains sizes of 200 nm, 100 nm, 50 nm, 20 nm and 10 nm respectively.

The effect of grain size on the thermal conductivity of polycrystalline $Si_{0.8}Ge_{0.2}$ is plotted in figure 4.3 normalized by the thermal conductivity of the single crystal. For an effective grain size of $l_g = 200$ nm, the largest grain size considered, the thermal conductivity is $\sim 40\%$ of the single crystal alloy at high temperature ($> 1000$ K) and close to $\sim 25\%$ at room temperature. Reducing the effective grain size to $l_g = 20$ nm further decreases the thermal conductivity to below $\sim 20\%$ of the single crystal conductivity at high temperatures and less than $\sim 10\%$ at room temperature.

The effect of phonon scattering from an square array of nanoscale pores was modeled in the transport simulations by explicitly resolving pore geometry in the simulation domain, with the pore/semiconductor interface modeled as a diffusely-scattering adiabatic boundary. This means that the total energy flux incident on an interface is re-emitted back into the simulation domain in all directions distributed over all ordinates and phonon frequencies in proportion to their equilibrium occupancy. The simulation domain was periodic

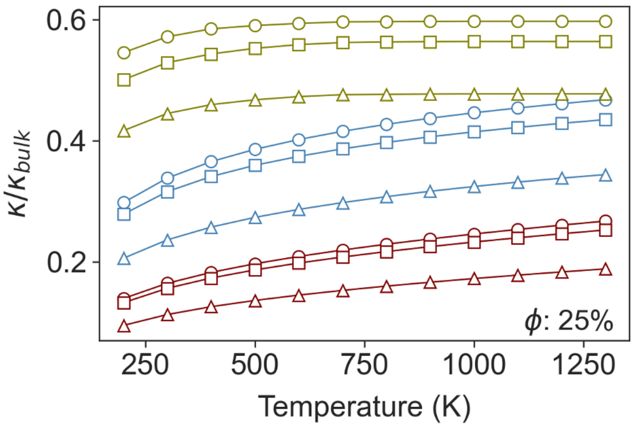

Figure 4.4: Reduction in thermal conductivity of single crystal $Si_{0.8}Ge_{0.2}$ alloy due to the addition of nanoscale porosity. The effects from pores with circular, square and triangular cross-section are plotted using markers of the same shape. The porosity is $\phi = 0.25$ and the red, blue and green lines are for pore-pore distances of 0.1 $\mu m$, 1 $\mu m$ and 20 $\mu m$, respectively.

in all directions, and the pores were prisms that extend through the periodic boundaries in one direction. Three pore geometries were considered: cylinders, square prisms, and triangular prisms. The spacing between pores was adjusted to study the effect of pore density on thermal conductivity, and the pore size was adjusted concomitantly to maintain a constant pore fraction of $\phi = 0.25$ — a pore fraction similar to that of the nanoporous Si films reported in experimental works [46]. As this pore fraction is relatively large, the smallest pore spacing considered was limited to 10 nm to ensure that the spacing between pores remained large enough that the confinement effects were not significant and that the electron and phonon dispersion of the material in the ligature between pores could still be reasonable approximated by those of the bulk crystal.

Figure 4.4 shows the thermal conductivity of a single crystal $Si_{0.8}Ge_{0.2}$ film con-

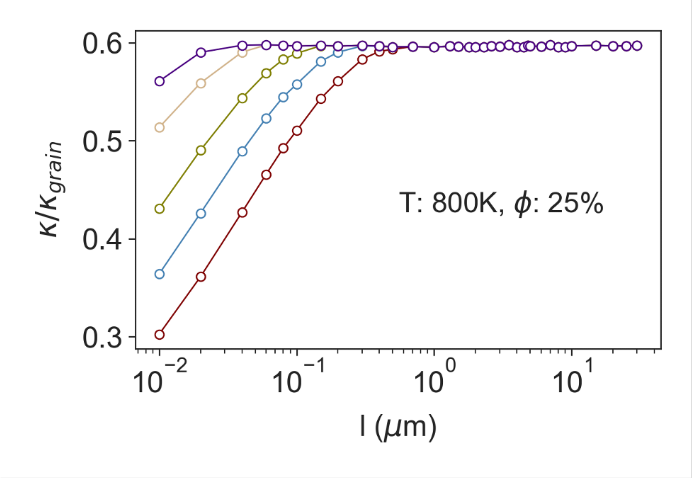

Figure 4.5: Thermal conductivity of polycrystalline $Si_{0.8}Ge_{0.2}$ containing cylindrical nanopores compared to the same polycrystalline material without pores. The thermal conductivity reduction is plotted *vs* pore spacing, $l$, for material with effective grain sizes of 200 nm (red), 100 nm (blue), 50 nm (green), 20 nm (brown) and 10 nm (purple). For all cases the pore fraction is $\phi = 25\%$.

taining an array of nanopores with different shape and spacing. The triangular pores yield the lowest thermal conductivity of the different geometries considered here. This is primarily due to the phonon view factor [84, 94] — a detailed discussion on the effect of the pores' shape is given in APPENDIX. The pore-pore distance is the governing factor in thermal conductivity reduction. For a given porosity, shortening the pore-pore spacing (and therefore increasing the number density of pores) lowers the thermal conductivity and makes it become insensitive to temperature [123]. The increase in the thermal conductivity *ratio* of the $0.1\mu m$ spaced pores in figure 4.4 is entirely due to the decrease of the thermal conductivity of single crystal $Si_{0.8}Ge_{0.2}$ with increasing temperature. This is mainly due to the suppression of long mean free path phonons near the Brillouin zone center — the main contributors to thermal conductivity in $Si_{0.8}Ge_{0.2}$.

While the plots in figures 4.3 and 4.4 show the separate effect on lattice thermal conductivity from grain boundaries and nanopores independently, the synergy of cylindrical pores and polycrystallinity is shown in figure 4.5 for a variety of difference grain and pore sizes. Although nanopores and grain boundaries both present obstacles for phonon scattering that reduce thermal conductivity relative to the monolithic single crystal, the introduction of voids also creates regions in the material where the thermal conductivity is locally zero — a composite of non-conducting fibers within a conductive matrix. In the diffusive limit the thermal conductivity of this composite is described by effective medium theory and, for cylindrical pores, depends on the pore fraction as $\kappa_{\text{composite}} = \frac{1-\phi}{1+\phi}\kappa_{\text{matrix}}$ [79]. From figure 4.5 it can be seen that adding porosity to polycrystalline $\text{Si}_{0.8}\text{Ge}_{0.2}$ *always* further reduces the thermal conductivity. If the pore spacing is significantly larger than the effective grain size the reduction in thermal conductivity is simply that of effective medium limit, however we start to see extra reduction in thermal conductivity even for pore spacings that are several times larger than the effective grain size.

Returning our attention to the diffuse limit, we note that the effective medium limit is also seen in the calculations for porous single crystal $\text{Si}_{0.8}\text{Ge}_{0.2}$ plotted in green in figure 4.4. In this plot we see that while the shape of the pores makes minimal difference to the thermal conductivity reduction in the ballistic limit, when the pore spacing is small, the pore shape does impact the effective medium theory limit. While cylindrical pores yield a 0.6 reduction in thermal conductivity, consistent with the equation above, the pores with triangular cross-section reduce thermal conductivity by $\sim 0.48$ consistent with the $\kappa_{\text{composite}}/\kappa_{\text{matrix}} = 1 - 4.37\phi^3 + 3.47\phi^2 - 2.67\phi$ formula [85].

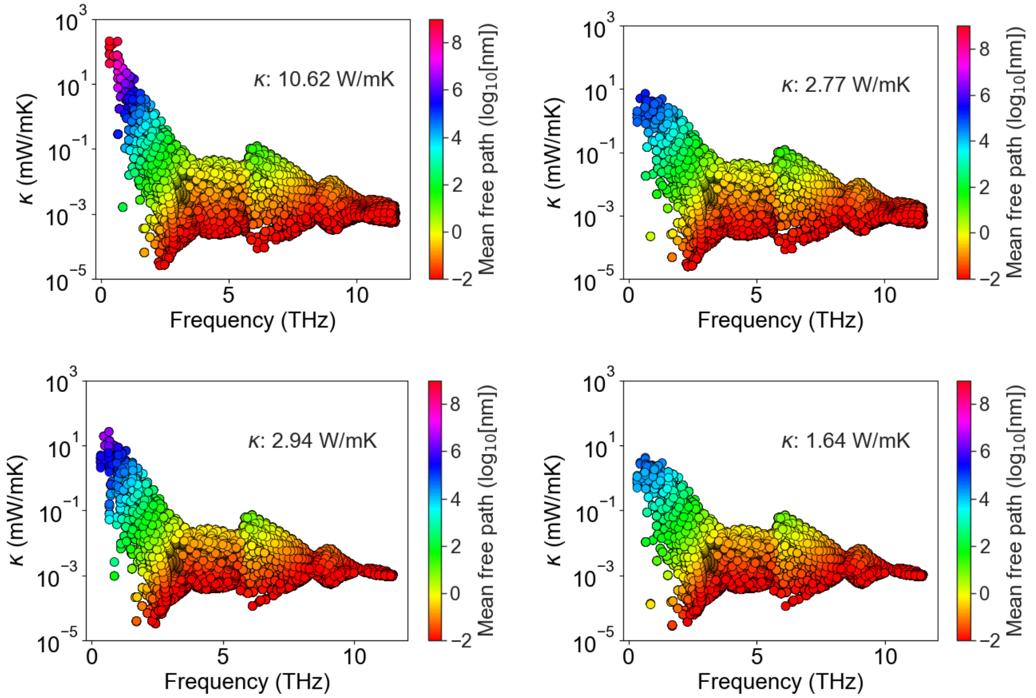

Figure 4.6: The per mode thermal conductivity plotted *vs* mode frequency in $Si_{0.8}Ge_{0.2}$ at 300 K. Plot (top-left) is for monolithic single crystal, (top-right) is for bulk polycrystalline material with effective grain size of 200 nm, (bottom-left) is for single crystal containing cylindrical pores with 500 nm pore spacing, and (bottom-right) is for the same polycrystalline materials as in (top-right) with the addition of the cylindrical pores of (bottom-left). For each point, the mode's mean free path is indicated by marker's color using a log color scale.

Figure 4.6 shows the contribution to thermal conductivity from each phonon mode across the frequency spectrum in single crystal $Si_{0.8}Ge_{0.2}$ (top-left), and how this changes with a 200 nm grain structure (top-right), addition of 500 nm spaced cylindrical pores (bottom-left), and the combination of both figure (bottom-right). This shows that the longest mean free paths in the pristine material are suppressed in structures with defects. Moreover, even though the pore spacing is more than double the distance between grain boundaries there is a significant further reduction in the mean free path of the low frequency modes when both pores and grain boundaries are present. One can also observed some mean free path suppression for high frequency modes with the addition of nanopores.

## 4.4 Charge Carriers Transport in Nanoporous $\mathbf{Si_{0.8}Ge_{0.2}}$

In order to obtain good thermoelectric properties, in most cases, $\mathrm{Si_xGe_{1\text{-}x}}$ thermoelectrics must be doped to high carrier concentrations. This can require the material to be doped beyond its solubility limit, which makes that device properties easily degraded irreversibly if the material is over heated to a point where the dopant becomes mobile and can precipitate out of solution. For phosphorus-doped $\mathrm{Si_xGe_{1\text{-}x}}$, experiments have shown that the carrier concentration varies with temperature as the solubility of the P dopant changes [124]. The variation is more noticeable at temperatures above 1000 K. In the work that follows, we restrict our attention to heavily $n$-type $\mathrm{Si_xGe_{1\text{-}x}}$, such as is obtained by doping with phosphorus, and we study the interplay between electrical and heat transport properties as the nanostructure and carrier concentration are varied.

The electrical properties in many semiconductors are described well by the semiclassical Boltzmann transport equation using the single relaxation approximation, integrating the contribution to transport from the charge carriers over a single electronic band [16]. This method has been used successfully to predict the transport coefficients of $\mathrm{Si_xGe_{1\text{-}x}}$ [39, 34]. In this model, the electrical conductivity, $\sigma$, at temperature $T$ is written as [16]

$$\sigma = -\frac{1}{3}e^2 \int \chi(E,T)\tau(E,T)dE, \tag{4.1}$$

with $\tau(E,T)$ the momentum relaxation time of electrons with energy $E$. The kernel $\chi(E)$

includes all the intrinsic non-scattering terms and is given by

$$\chi(E,T) = \nu^2(E)D(E)\frac{df(E,E_f,T)}{dE}, \tag{4.2}$$

were $E_f$ is the Fermi energy level, $\nu(E)$ is the charge carrier group velocity, $f(E_f,E,T)$ is the Fermi-Dirac distribution, and $D(E)$ is density of electronic states.

The Seebeck coefficient, $S$, and charge carriers' contribution to thermal conductivity, $\kappa_e$, depend on higher moments of $\chi$ with

$$S = -\frac{1}{eT}\frac{\int \gamma\tau dE}{\int \chi\tau dE}, \tag{4.3}$$

and

$$\kappa_e = -\frac{1}{3T}\left(\int \zeta\tau dE - \frac{(\int \gamma\tau dE)^2}{\int \chi\tau dE}\right). \tag{4.4}$$

Here the terms $\gamma$ and $\zeta$ are energy weighted $\chi$ given by $\gamma = \chi\,(E - E_f)$ and $\zeta = \chi\,(E - E_f)^2$, respectively, and the explicit functional dependence of the terms has been dropped from the notation for compactness and clarity.

To evaluate the function $\chi$ in equations 4.1 to 4.4 requires knowing the density of states, carrier group velocity, and Fermi energy. We modeled density of states of the $\mathrm{Si_xGe_{1\text{-}x}}$ conduction band, $D(E)$, using the standard expression for non-parabolic electron band

$$D(E) = \frac{m_e^{\frac{3}{2}}}{\pi^2\hbar}(1+2\alpha E)\sqrt{2E(1+\alpha E)}, \tag{4.5}$$

where $m_e$ is the electrons' *density of state effective mass* (which is separate from the transport effective mass used later). For $\mathrm{Si_xGe_{1\text{-}x}}$ alloys the density of states is found to be well represented across a wide range of compositions using

$$m_e = [1.08(1-\mathrm{x}) + 1.41\mathrm{x} - 0.183\mathrm{x}(1-\mathrm{x})]\,m_o,$$

where $m_o$ is free electron rest mass equal to $9.11 \times 10^{-31}$ kg [28], and with the anharmonicity term, $\alpha = 0.5$ eV$^{-1}$. This later term describes the deviation of the conduction band from parabolic due to the admixture of s-like conduction band states and p-like valence band states [32].

At compositions with less than 85% Ge, the band structure of $Si_xGe_{1-x}$ matches that of Si [28], and so the electron group velocity was obtained from the slope of the conduction band along the conduction band valley in Si obtained from density functional theory (DFT). That is, $\nu = \frac{1}{\hbar} |\nabla_k E|$ along the $\langle 100 \rangle$ directions on the $\Gamma$ to $X$ Brillouin zone path. The Si band structure was computed with the Vienna Ab initio Simulation Package (VASP) [19, 125, 98, 97], and using the generalized gradient approximation (GGA) with the Perdew-Burke-Ernzerhof exchange correlation functional (PBE) [23]. Projector augmented wave (PAW) pseudopotentials were used to represent ion cores and their core electrons [24, 25], and the Kohn-Sham wave functions were constructed using a planewave basis set with a 700 eV energy cutoff. A Monkhorst-Pack $12 \times 12 \times 12$ k-point grid was used to sample the Brillouin zone [26]. The primitive cell and atomic basis were relaxed to minimize forces on the atoms to better than $10^{-6}$ eV/Å. The electronic band structure used to compute $\nu(E)$ were interpolation from a $45 \times 45 \times 45$ k-point grid. Finally, the band structure and therefore group velocity were treated as temperature independent.

The final term that appears in $\chi$ is the Fermi energy. This term is not an intrinsic property and is strongly dependent on the carrier concentration and temperature. For a given carrier concentration, $n_c$, the Fermi energy, $E_f$, was computed self-consistently with the density of states in equation 4.5 by numerically solving the integral equation

$$n_c = \int_0^\infty D(E) f(E, E_f, T) dE, \tag{4.6}$$

using the conduction band edge to set the reference frame.

To complete the transport model, we need to compute the mean time between electron scattering events. In bulk $\mathrm{Si_xGe_{1-x}}$ the dominant electron scattering processes are scattering by acoustic phonons ($\tau_p$), ionized impurities ($\tau_i$) and alloy disorder ($\tau_a$). Ravich has modeled the rate of electron-phonon scattering as [33]

$$\tau_p(E)^{-1} = \frac{\pi D_A^2 k_B T D(E)}{\rho \nu_s^2 \hbar} \left\{ \left[ 1 - \frac{\alpha E}{1 + 2\alpha E} \left( 1 - \frac{D_v}{D_A} \right) \right]^2 - \frac{8}{3} \frac{\alpha E (1 + \alpha E)}{(1 + 2\alpha E)^2} \frac{D_v}{D_A} \right\}, \tag{4.7}$$

where $\alpha$ describes the conduction band shape as in equation 4.5, and $\rho$ and $\nu_s$ are the crystal's density and speed of sound. In $\mathrm{Si_xGe_{1-x}}$, these have values of $\rho = 2329 + 3493\mathrm{x} - 499\mathrm{x}^2$ kg/m$^3$ and $\nu_s = \sqrt{}(B/\rho)$, where $B$ is bulk module which is given by $B = 98 - 23\mathrm{x}$ GPA, with x is the atomic fraction of Ge [28]. The terms $D_v$ and $D_A$ are the electron and hole deformation potentials and are equal to 2.94 eV and 9.5 eV, respectively [32].

For strongly screened Coulomb scattering that occurs when the carrier concentration is high, the electron scattering due to ionized impurities is given by [29]

$$\tau_i(E)^{-1} = \frac{\hbar}{\pi N_i \left( \frac{e^2 L_D^2}{4\pi \epsilon \epsilon_o} \right)^2 D(E)}, \tag{4.8}$$

with $N_i$ is the concentration of ionized impurities which we assume to be equal to the carrier concentration, $N_i = n_c$. The terms $\epsilon$ and $\epsilon_o$ are the relative and vacuum permittivity, with the former represented well with $\epsilon = 11.7 + 4.5\mathrm{x}$ in $\mathrm{Si_xGe_{1-x}}$ alloys [28]. The term $L_D$ in equation **??** is the Debye length, which in doped semiconductors has the generalized form of [30]

$$L_D = \frac{e^2 N_c}{4\pi\epsilon\epsilon_o k_B T}\left[F_{-\frac{1}{2}}(\eta) + \frac{15\alpha k_B T}{4} F_{\frac{1}{2}}(\eta)\right], \tag{4.9}$$

where $N_c = 2\left(\frac{m^* k_B T}{2\pi\hbar^2}\right)^{\frac{3}{2}}$. We modeled the temperature dependence of the conduction band effective mass, $m^*$, as $m^*(T) = m_o^*(1 + 5\alpha k_B T)$ [31]. The term $m_o^*$ is equal to $0.28m_o$, where $m_o$ is free electron rest mass as in equation 4.5. The effective mass is temperature dependent because the different sampling of the conduction band curvature as the Fermi window increases with temperature.

The rate of electron scattering due to the disordered arrangement of Ge atoms on the Si lattice is modeled as [126]

$$\tau_a(E)^{-1} = 0.75\frac{\mathrm{x}(1-\mathrm{x})3a^3\pi^3 U_A^2 {m^*}^{\frac{3}{2}}\sqrt{E}}{8\sqrt{2}\pi^2\hbar^4}, \tag{4.10}$$

where x is the atomic fraction of Ge, $a$ is the lattice parameter given as $a = 5.431 + 0.2\mathrm{x} + 0.027\mathrm{x}^2$ [28] (5.47 Å for $\mathrm{Si_{0.8}Ge_{0.2}}$). The term $U_A$ is the alloy scattering potential and is equal to 0.7 eV for $\mathrm{Si_{0.8}Ge_{0.2}}$ [32].

The three electron scattering terms above are sufficient to model single crystal $\mathrm{Si_xGe_{1\text{-}x}}$ with no porosity. We have validated this model against a set of phosphorous doped $\mathrm{Si_{0.7}Ge_{0.3}}$ experiments reported by Vining [3]. Figure 4.7 shows the comparison of the model prediction of electrical conductivity and Seebeck coefficient with the experimental data for $\mathrm{Si_{0.7}Ge_{0.3}}$ with three different doping concentrations. We compared the results up to 1000 K. The model is in good agreement with experimental data in the whole range of temperature for the electrical conductivity. The prediction for $S$ is less accurate, showing a small systematic underestimate of the Seebeck coefficient due to its sensitivity to the band shape and doping concentration. We remark that Vining only reported a single carrier

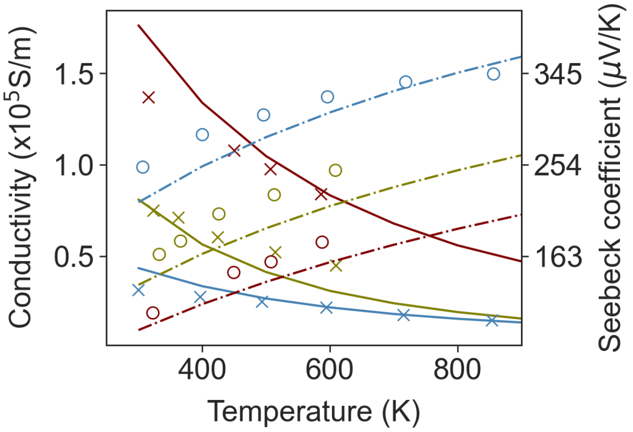

Figure 4.7: Comparison of the model prediction (lines) of electrical conductivity and thermopower in $Si_{0.7}Ge_{0.3}$ with experimentally reported results (markers). The measured and predicted electrical conductivity are shown with crosses and solid lines, respectively, and the measured and predicted Seebeck coefficients with circles and dashed lines. The data is for three different doping levels that have carrier concentrations of $1.45 \times 10^{20}$ 1/cm$^3$ (red), $6.75 \times 10^{19}$ 1/cm$^3$ (blue) and $2.2 \times 10^{19}$ 1/cm$^3$ (green). The experimental data is taken from reference [3]. The overall agreement is good, although the model gives a small systematic underestimate of Seebeck coefficient.

concentration for each sample, so we had to assume that carrier concentration is constant across the span of temperature; however, it is likely that carrier concentration changes with temperature. The transport model was implemented as part of a python package called *Thermoelectric.py* that has been made available for public use at the GitHub repository in reference [99].

In the nanostructured $Si_{0.8}Ge_{0.2}$ of interest in this study, there are two additional electron scattering processes that arise as a result of the morphology: electron scattering at grain boundaries, and scattering from pores. The rate of electron momentum relaxation due to elastic scattering from a uniform dispersion of pores can be modeled as [34]

$$\tau_{np}(s)^{-1} = \frac{N}{8\pi^3}\int SR_{kk'}(1-\cos(\theta_{kk'}))dk'. \tag{4.11}$$

Here $N$ is the number density of pores, and the term $SR_{kk'}$ is the rate of transition of an electron from an initial state with wave vector $k$ and energy $E$ to a state $k'$ with energy $E'$ due to a single pore. The $1-\cos(\theta_{kk'})$ term accounts for the change in momentum that accompanies this transition, with $\theta_{kk'}$ the angle between initial and scattered wavevectors. For a time-invariant potential, the transition rate $SR_{kk'}$ is given by Fermi's golden rule, $SR_{kk'} = \frac{2\pi}{\hbar}\left|M_{kk'}\right|^2 \delta(E-E')$, where the matrix element operator $M_{kk'}$ describes the strength which the pore couples the initial and final states and the number of ways the transition can occur, and $\delta$ is the Dirac delta function. For Bloch waves, $M_{kk'}$ is given by the integral of the overlap of the initial and final state with the pore potential $U(r)$ so that [35]

$$M_{kk'} = \int e^{i(k'-k).r}U(r)dr. \tag{4.12}$$

For energy conservative (elastic) scattering between eigenstates with the same energy equation 4.11 can be recast as a surface integral over the isoenergetic k-space contour $\Gamma$ that satisfies $E(k') = E(k)$

$$\tau_{np}^{-1}(s) = \frac{N}{(2\pi)^2\hbar}\oint_{\Gamma}\frac{\left|M_{kk'}\right|^2}{\nabla E(k')}(1-\cos\theta)dS(k'), \tag{4.13}$$

where $dS$ is the incremental area of the isoenergetic k-space surface. In most indirect bandgap semiconductors such as $\mathrm{Si}_{0.8}\mathrm{Ge}_{0.2}$ the contours of isoenergy states near to conduction band valley have ellipsoidal shape in momentum space that can be approximated as $E(k) = \hbar^2[(\frac{(k_l-k_{ol})^2}{2m_l^*} + \frac{(k_t-k_{ot})^2}{m_t^*}]$, where $E(k)$, $k_o = (k_{ol}, k_{ot}, k_{ot})$, $m_l^*$, $m_t^*$ are energy level from conduction band edge, the location of the conduction band minimum, longitudinal and transverse effective masses, respectively. We used $m_l^* = 0.98m_o$, $m_t^* = 0.19m_o$ where $m_o$ is free electron rest mass, and $k_o = 2\pi/a(0, 0, 0.85)$, where $a$ is the lattice parameter. The pore potential, $U(r)$, in equation 3.6 is assumed to be

$$U(r) = \begin{cases} U_o & \text{for r inside the pore} \\ 0 & \text{otherwise} \end{cases}, \tag{4.14}$$

where $\mathrm{U_o} = 4.05$ eV is the electron affinity of bulk $\mathrm{Si_{0.8}Ge_{0.2}}$. For an infinitely long cylindrical pores with radius $r_o$, and aligned with axis parallel to $z$, this gives the scattering matrix element operator

$$M_{kk'}^{cylinder} = 2\pi r_o U_o l_z \left( \frac{J_1(r_o q_r)}{q_r} \right) \delta_k(q_z). \tag{4.15}$$

In this equation, $q = k - k'$ is the scattering vector, and $q_z$ and $q_r$ are the components of $q$ parallel and perpendicular to the cylinder axis. The term $\delta_k$ is the Kronecker delta function, and $J_1$ is the first-order Bessel function of the first kind, and $l_z$ is the pore's length perpendicular to transport direction. We have previously computed the scattering matrix operators for pores with rectangular and triangular cross-sections and these can be found in reference [36]. The number density of pores is related to porosity, $\phi$, and the pore size through the relationship $N = \phi/V_p$, where $V_p$ is the volume of the pores.

A similar use of Fermi's Golden rule can be used to model the rate of electron scattering by grain boundaries. Minnich et al have suggested that grain boundaries provide a scattering potential of magnitude $U_{GB}$ that decays away from the grain boundary over distance $z_o$ [39]. From this, they derived the scattering operator matrix element for a small disc of grain boundary with radius $r_o$ as

$$M_{kk'} = 4\pi U_g \left[ \frac{z_o}{1 + (q_z z_o)^2} \right] r_o^2 \left[ \frac{J_1(q_r r_o)}{q_r r_o} \right], \tag{4.16}$$

where $q_r$ and $q_z$ are the components of the scattering vector $q$ that are parallel and perpendicular to the boundary, respectively. The scattering potential, $U_{GB}$, is defined as

$$U_{GB}(r) = \begin{cases} U_g e^{\frac{-|z|}{z_o}} & r < r_{GB} \\ 0 & \text{otherwise} \end{cases} . \tag{4.17}$$

In this equation $z_o$ is a constant related to the thickness of the depletion region at the grain boundary, and $U_g$ was proposed to be $U_g = \frac{e^2 N_t^2}{8\epsilon\epsilon_o N_i}$. Here, $\epsilon$ is the permittivity, and $N_t$ is the number density per area of electron traps in the depletion region. To compute the total scattering rate from all boundaries the number density of grain boundary scattering centers is defined as $N = 4f/(l_g r_0^2)$, where $0 < f < 1$. Unfortunately, exact values of $r_o$, $z_o$, $f$, $N_t$ are unknown. In this manuscript we use the values proposed by Minnich et al. in their original paper on $\mathrm{Si_{0.8}Ge_{0.2}}$ ($r_o = 1$ nm, $z_o = 2$ nm, $f = 0.7$, $N_t = 10^{13}$ $1/\mathrm{cm}^2$, and we refer the reader to their work for the full details of the approach [39].

Figure 4.8 shows the variation in the electron lifetimes versus energy for the different scattering processes described above in $\mathrm{Si_{0.8}Ge_{0.2}}$ doped to a carrier concentration of $10^{20}$ $1/\mathrm{cm}^3$ at 500 K. At this doping level and temperature impurity scattering is the strongest scattering process for low energy electrons, while high energy electrons are predominantly scattered by phonons; however, alloy, impurity, and phonon scattering all make a non negligible contribution to the total rate of scattering. The scattering time due to grain boundaries in polycrystalline material with effective grain size 50 nm, and the scattering time due to 20 nm spaced cylindrical pores (for $\phi = 25\%$) are also plotted in figure

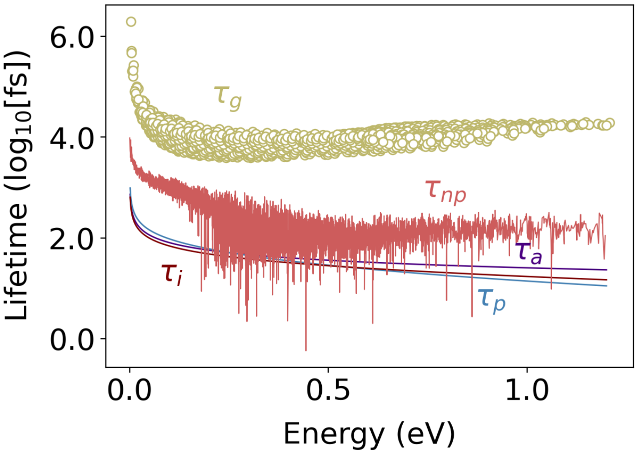

Figure 4.8: Electron lifetime for the different scattering mechanisms in $Si_{0.8}Ge_{0.2}$ at 500 K with a carrier population of $10^{20}$ 1/cm$^3$. In low energy states electron-impurity is the strongest scattering term. For higher energy levels electron-phonon is the main source of scattering. The electron-grain boundary ($l_g = 50$ nm) and electron-pore (pore-pore spacing of 20 nm) for 25% porosity are two additional scattering terms in polycrystalline porous $Si_{0.8}Ge_{0.2}$ that are shown in green and light red, respectively.

4.8. For the extended pores considered here, scattering is only possible into states with the same component of wave vector along the pore axis, i.e., $q_z = 0$. This condition, combined with the isoenergetic constraint, reduces the scattering integral to an elliptical line, drastically reducing the number of states that can participate in scattering, and means that the extended pores cause next to no change in the electron momentum along the axis of the pores.

There is one final adjustment that must be made to the electrical transport model for the case of porous $Si_xGe_{1-x}$. Although pores do not change the local material properties such as carrier concentration, density of states, or Fermi energy, away from the pores, they do change the volume-averaged carrier concentration due to the reduction in the volume-averaged density of states. This will impact the conductivity, and thus the effective electrical conductivity of porous materials is modeled as $\sigma = (1-\phi)\sigma_{\mathrm{np}}$. This change does not affect the Seebeck coefficient since it describes the relationship between two intensive quantities and so the changes in the density of state cancels out for the denominator and numerator in equation 4.3. This means that the extended pores lower the power factor as $PF = (1-\phi)PF_{\mathrm{np}}$.

## 4.5 Thermoelectric $ZT$ of Nanoporous Polycrystalline $\mathbf{Si_{0.8}Ge_{0.2}}$

To compute the total $ZT$ of $\mathrm{Si_xGe_{1\text{-}x}}$ we combine the computed electrical and phonon transport properties described in the sections above with the electronic contribution to thermal conductivity computed using equation 4.4. While phonons are the main contributors to thermal conductivity in crystalline dielectrics, in nanoengineered semiconductors where fine grain boundaries significantly suppressed lattice thermal conductance, the electron contribution to heat conduction is considerable — this is of especial importance for designing TEs for high temperature working condition where maximum PF takes place at higher carrier concentration as can be seen in figure 4.11 in the APPENDIX.

Figure 4.9 shows the best $ZT$ performance that could be obtained by tuning the carrier concentration at each temperature, along with the corresponding optimal carrier concentration. It can be seen that both the addition of grain boundaries and nanopores produce a significant improvement in $ZT$ with the grain boundaries having the stronger effect. The enhancements are not additive, so that there is little additional benefit to adding 5% porosity to polycrystalline $\mathrm{Si_{0.8}Ge_{0.2}}$, but there is a significant gain to be had by adding

25% porosity. Most importantly, with addition of nanostructure, the carrier concentration at which peak $ZT$ occurs is reduced. Pores and grain boundaries have negligible effect on electron scattering, but pores reduce the overall density of carriers reducing electrical conductivity. With the combination of pores and grain boundaries phonon conductivity can be sufficiently suppressed that the electric heat transport becomes significant. In this regime ZT can be further enhanced by reducing the carrier concentration to reduce the electrical conductivity and electronic thermal conductivity while increasing the thermopower.

The solubility of P in Si at 1000 K, is $10^{21}$ Atoms/cm$^3$ [127], and the electrically active fraction of that is significantly lower. The solubility of P in $Si_{0.8}Ge_{0.2}$ is around half that of P in Si [128]. The carrier concentrations required to obtain peak $ZT$ in single crystal $Si_{0.8}Ge_{0.2}$ are likely to require a super saturated concentration of P. This not only requires heating additional processing steps to achieve, it is easily destroyed during service if the material in inadvertently heated to a point when the dopant becomes mobile. With the addition of nanostructuring $Si_{0.8}Ge_{0.2}$ requires only half the carrier concentration to obtain peak $ZT$ making material easier to process and more thermally robust.

## 4.6 Conclusion

To summarize we have used quasiballistic semiclassical Boltzmann transport model to elucidate the effect of extended nanopores with different shapes on thermoelectric performance of $Si_{0.8}Ge_{0.2}$ based TE materials. We have shown that while the pristine $Si_{0.8}Ge_{0.2}$ alloys' thermal conductivity varies from about 12.5 W/mK at 200 K down to 5.4 W/mK at 1300 K, only 5% porosity of extended pore (100 nm spacing) can lower the conductivity

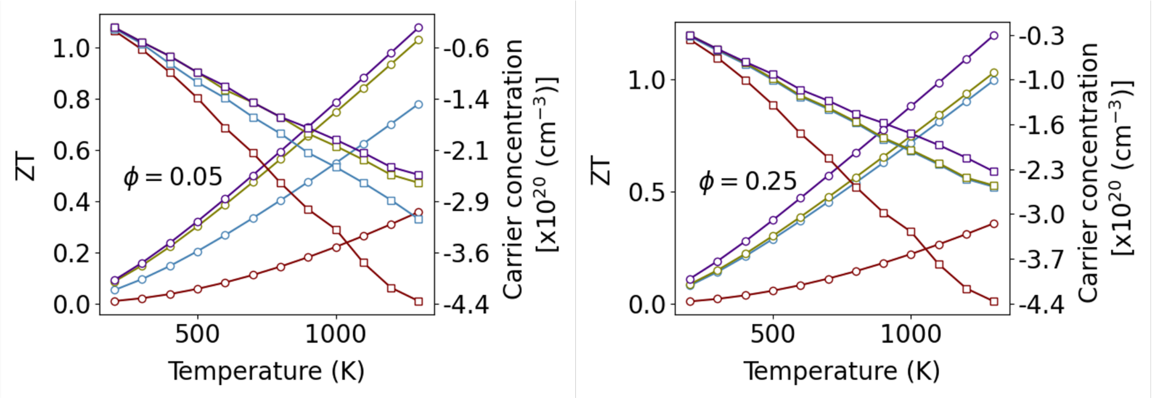

Figure 4.9: Plots of the maximum $ZT$ that can be obtained by tuning the carrier concentration at each temperature. The data plotted with circles is the $ZT$ and corresponds to the left hand axis, while data plotted with squares is the carrier concentration that produces the best $ZT$. The red line is for monolithic single crystal $\mathrm{Si}_{0.8}\mathrm{Ge}_{0.2}$, the same material containing porosity $\phi$ in the form of cylindrical pores with a 20 nm spacing in blue, and polycrystalline $\mathrm{Si}_{0.8}\mathrm{Ge}_{0.2}$, with 20 nm grain size in green, and polycrystalline material with the 20 nm grain size and pores with a 20 nm spacing is plotted in purple. The top plot (left) is for 25% porosity, while plot (right) is for 5% porosity.

to around 3 W/mK. Further increasing porosity to 25% lower thermal conductivity to less than 1.7 W/mK. The porous alloys show very weak dependency on temperature as the rate of scattering of heat carrying phonons by the phonon bath is superseded by scattering at interfaces. We further evaluated the effect of porosity on polycrystalline $\mathrm{Si}_{0.8}\mathrm{Ge}_{0.2}$ with effective grain sizes from 10 nm up to 200 nm. Cylindrical pores with 100 nm spacing reduced the thermal conductivity more than 40% compare to the polycrystalline material with 50 nm grains but no pores. We have also modeled electron-pore scattering rate. The model demonstrated that electron has very weak coupling with extended pores and therefore the changes in the power factor is only due to changes in the volume averaged density of state. This model shows that introducing 20 nm spacing cylindrical nanopores in polycrystalline $\mathrm{Si}_{0.8}\mathrm{Ge}_{0.2}$ with 20 nm nanograins thermoelectrics can further improve the ZT up to 20%.

## 4.7 Appendix

### 4.7.1 Appendix A: Importance of Pore's Shape on Thermal Conductivity

Figure 4.10 shows the fractional thermal conductivity of pores with different shapes of cylindrical (marked with circle), cubic (marked with square), and triangular prism (marked with triangle). The cylindrical pores show the highest thermal conductivity while the triangular prism pores show the lowest thermal conductivity among the pores studied here ($\sim$ 80% of the cylindrical pores for the same spacing). This can be explain using phonon view factor — the possibility of a phonon successfully traveling through the film thickness without colliding with voids. For cylinder ($F_c$), square prism ($F_s$) and triangle prism($F_t$), the view factors are defined as [85]

$$F_c = 1 - \sqrt{\frac{4\phi}{\pi}}\left(\frac{\pi}{2} - \left[\sin^{-1}\left(\sqrt{\frac{4\phi}{\pi}}\right) + \sqrt{\frac{\pi}{4\phi} - 1} - \sqrt{\frac{\pi}{4\phi}}\right]\right) \tag{4.18}$$

$$F_s = 1 - 2\sqrt{\phi}\left(1 - \frac{1}{2}\left[\sqrt{1 + \left(\frac{1}{\sqrt{\phi}} - 1\right)^2} - \left(\frac{1}{\sqrt{\phi}} - 1\right)^2\right]\right) \tag{4.19}$$

$$F_t = \sqrt{4\frac{\phi}{\sqrt{3}} - 2\sqrt{\frac{\phi}{\sqrt{3}}} + 1} - 2\sqrt{\frac{\phi}{\sqrt{3}}} \tag{4.20}$$

For $\phi = 0.25$, the view factors are $F_c = 0.2776$, $F_s = 0.2071$, $F_t = 0.1443$. The cumulative lattice thermal conductivity of bulk materials is generally describe by a uniparameter logistic function (in logarithmic abscissa) with form of $K(\Lambda) = \frac{\kappa_l}{1+\frac{\Lambda_o}{\Lambda}}$. In this equation, $K$ and $\Lambda$ are the cumulative lattice thermal conductivity in bulk material and phonon mean free paths, respectively. The $\Lambda_o$ term is a uniparameter used to fit cumulative thermal conductivity with the logistic function. We remark that $\Lambda_o$ roughly estimates the

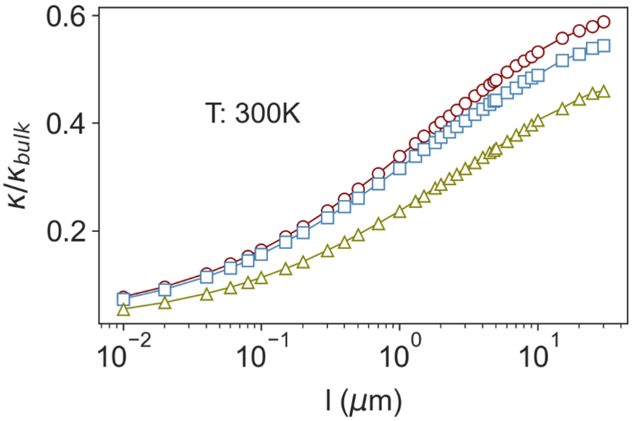

Figure 4.10: Fractional thermal conductivity *vs* pore spacing for pores with different shapes of cylindrical in red, cubic in blue and triangular prism in green at 300 K.

feature size at which nanostructuring dominates over anharmonic scattering [89].

We use the same model for the porous $Si_{0.8}Ge_{0.2}$ and fit the cumulative thermal conductivity versus mean free path to the proposed kernel to find $\Lambda_o$ for structures with different shaped pores — we noticed that this model does not fit well for materials with grain boundaries. In the bulk, $\Lambda_o$ is equal to 620 nm. For 500 nm pore-pore spacing, $\Lambda_o$ is 165 nm, 150 nm, and 130 nm for circular, cubic and triangular pores, respectively. These values are well bellow the $\Lambda_o$ in bulk, emphasizes that the pores are the dominant scattering term. We note that the structure containing triangular pores has the lowest $\Lambda_o$ and therefore to further tune thermal conductivity using secondary type of defects (e.g. grain boundary), the feature size of the additional defects should be lower for structures with triangular shaped pores.

Figure 4.11 shows the mode-resolved thermal conductivity across the frequency spectrum in porous $Si_{0.8}Ge_{0.2}$ with 5 $\mu m$ pore-pore spacing with cylindrical pore and trian-

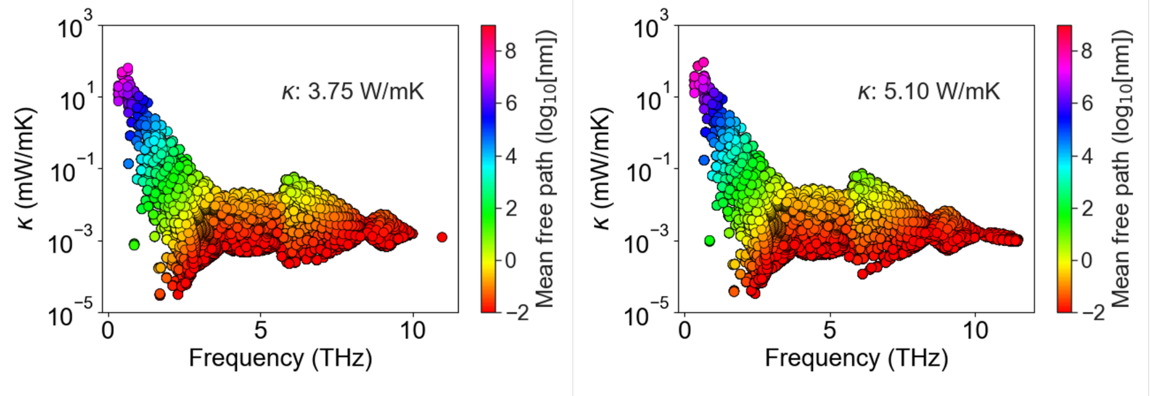

Figure 4.11: Mode-resolved thermal conductivity across the frequency spectrum in porous $Si_{0.8}Ge_{0.2}$ with 5 $\mu m$ pore-pore spacing with (left) cylindrical pore and (right) triangular prism pore.

gular prism. The mean free path is indicated by color intensity. We observed some missing long mean free path in materials with prism pore that exist in materials with cylindrical pore. Overall, the mean free path and thereby modal thermal conductivity in porous $Si_{0.8}Ge_{0.2}$ with cylindrical pores are higher across the spectrum.

### 4.7.2 Appendix B: Importance of Electrical Contribution to Thermal conductivity

Figure 4.12 (left) shows the ratio of electron thermal conductivity to lattice thermal conductivity for the best $ZT$ performance in crystalline $Si_{0.8}Ge_{0.2}$ in red, $Si_{0.8}Ge_{0.2}$ with cylindrical pores of pore-pore spacing of 20 nm in blue, the polycrystalline $Si_{0.8}Ge_{0.2}$ with $L_g = 20$ nm in green and nanoporous polycrystalline $Si_{0.8}Ge_{0.2}$ with cylindrical pores of 20 nm spacing and $L_g = 20$ nm in purple. In nanostructured $Si_{0.8}Ge_{0.2}$, charges carry a significant amount of heat especially at high temperatures. Figure 4.12 (right) shows the variation of ZT with carrier concentration in crystalline $Si_{0.8}Ge_{0.2}$ in red, $Si_{0.8}Ge_{0.2}$ with

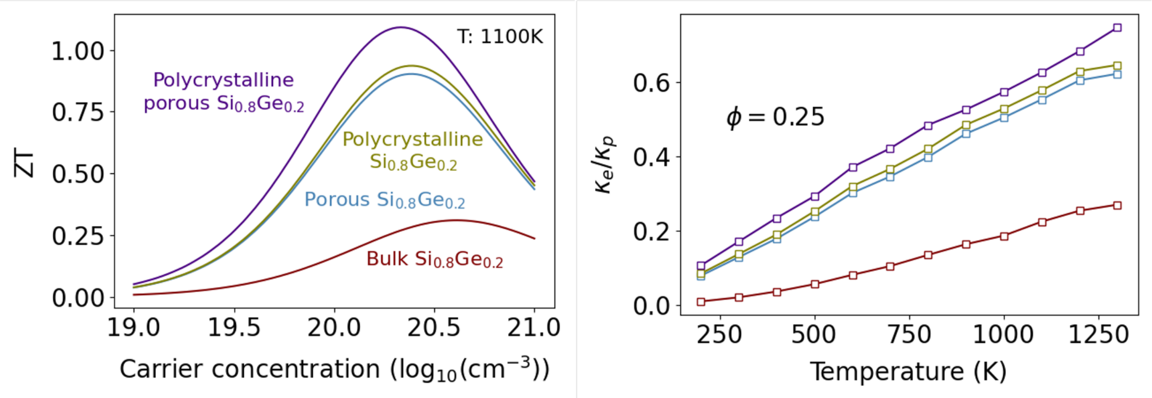

Figure 4.12: (Left) The electron thermal conductivity to lattice thermal conductivity ratio versus temperature and (right) variation of ZT with carrier concentration at 1100 K in bulk pristine $Si_{0.8}Ge_{0.2}$ in red, porous $Si_{0.8}Ge_{0.2}$ in blue, polycrystalline $Si_{0.8}Ge_{0.2}$ in green and polycrystalline porous $Si_{0.8}Ge_{0.2}$ in purple.

cylindrical pores with 20 nm spacing in blue, the polycrystalline $Si_{0.8}Ge_{0.2}$ with $L_g = 20$ nm in green and nanoporous polycrystalline $Si_{0.8}Ge_{0.2}$ with cylindrical pores of 20 nm spacing and $L_g = 20$ nm in purple at 1100 K. The maximum achievable $ZT$ is shifted to lower carrier concentration in nanoengineered structures.

## Chapter 5

# Heat Current Anticorrelation Effects Leading to Thermal Conductivity Reduction in Nanoporous Si

### 5.1 Abstract

Prevailing nanostructuring strategies focus on increasing phonon scattering and reducing the mean-free-path of phonons across the spectrum. In nanoporous Si materials, for example, boundary scattering reduces thermal conductivity drastically. In this work, we identify an unusual anticorrelated specular phonon scattering effect which can result in additional reductions in thermal conductivity of up to $\sim 80\%$ for specific nanoporous

geometries. We further find evidence that this effect has its origin in heat trapping between large pores with narrow necks. As the heat becomes trapped between the pores, phonons undergo multiple specular reflections such that their contribution to the thermal conductivity is partly undone. We find this effect to be wave-vector dependent at low temperatures. We use large-scale molecular-dynamics simulations, wave- packet analysis, as well as an analytical model to illustrate the *anticorrelation effect*, evaluate its impact on thermal conductivity, and detail how it can be controlled to manipulate phonon transport in nanoporous materials.

## 5.2 Introduction

Nanostructuring has enabled an unprecedented control of phonon transport with widespread applications ranging from microelectronic devices [129] to data storage [130], and microelectromechanical systems [131, 132]. Strong focus has been placed on reducing thermal conductivity for thermoelectric and heat insulation applications [68, 69, 46, 133]. This is largely because nanostructuring can significantly reduce a material's thermal conductivity—particularly in semiconductors and dielectrics. Reductions of up to two orders of magnitude have been observed over the last few years in several Si-based nanostructures, including rough Si nanowires [134, 135], thin films [136, 137], and Si-based alloys and superlattices [138]. Recent works concerning Si-based nanoporous materials have also shown that the room-temperature thermal conductivity can be reduced beyond the material's amorphous limit [68, 69, 46]. The consensus is that porosity reduces the heat capacity of the material and thus its thermal conductivity to some degree, but the additional scattering of phonons on the pore surfaces reduces the thermal conductivity even below the amorphous limit.

Existing nanostructuring strategies largely focus on alloying and introducing defects at different length scales to increase "incoherent" phonon scattering and thereby reduce the relaxation times of phonons across the spectrum. Most often, the phonon-gas picture suffices to describe thermal conductivity, even in nanoporous materials [103, 139, 140]. How- ever, the issue as to whether "coherent" wave effects alter the phonon dispersion relations—changing group velocities, the density of states, and creating phononic band gaps—or result in the localization of modes is still an open topic [69, 140, 141, 142, 143]. Herein, we report the emergence of anticorrelated (AC) specular phonon scattering (and thus heat flux) as a result of heat trapping between the pores, which can provide up to $\sim 80\%$ *additional* reduction in thermal conductivity for specific nanoporous geometries. Anticorrelated heat flux has been observed in amorphous and fluid materials, but not in crystalline materials [144, 145, 146, 147]. The AC effect can benefit thermoelectric applications, but also find wider application for the control and manipulation of heat-carrying phonons in nanophononic metamaterials in general. In this work we use large-scale equilibrium molecular dynamics (EMD), wavepacket simulations, and develop an analytical model to: (1) describe the anticorrelated heat-flux behavior and the conditions that preclude it (heat trapping), (2) evaluate its impact on thermal conductivity, and (3) detail how this effect can be controlled to manipulate phonon transport in nanoporous materials. We begin by describing the approaches used (Sec. II), followed by the observations of anticorrelated heat-flux behavior as a function of the nanoporous geometries (Sec. III), obtained with the Green-Kubo approach. In Sec. IV, we discuss the results of wave-packet simulations, which provide an illustrative picture of the underlying physical mechanism for the heat-flux anticorrelation. These results indicate that heat trapping and multiple reflections between the pores is what manifests as anticorrelation effects in the heat flux and further suggest the effect to be wave-vector dependent. Finally (in Sec. V), a simple ray-tracing model is introduced, which connects the behavior observed in Secs. III and IV by showing, in a simple manner, how specular phonon reflections between the pores with multiple reflections can lead to heat-flux anti- correlation effects. Section VI offers a conclusion for the bulk of the work presented.

## 5.3 Methods

Thermal transport in nanostructured geometries requires an understanding beyond what is achievable at a continuum level, and yet simulation domains larger than can be accommodated by first-principles approaches. Methodologies available to study nanoporous morphologies are thus limited to classical molecular dynamics (MD) [148, 149, 150, 151], or semiclassical approaches involving the numerical solution of the Boltzmann transport equation (BTE) [152, 153, 123, 154, 101], and, to some extent, lattice dynamics [148, 155, 156]. In this work, we use a combination of both equilibrium molecular dynamics (EMD) and wave-packet simulations to evaluate thermal transport in Si nanoporous structures. We further develop a simple statistical model of a gray population of heat-carrying acoustic phonons to illustrate how heat trapped between the pores can lead to anticorrelated behavior in the heat-current autocorrelation function (HCACF). The model is described in Sec. V.

The Green-Kubo is a well-established approach to deter- mine the thermal conductivity of a system from its thermal fluctuations at equilibrium, such that the thermal conductivity along $x$ [i.e., the length of the simulation cell as shown in the inset in Fig. 5.1(a)], $\kappa_x$ , is given by

$$\kappa_x = \frac{V}{k_B T^2} \int_0^\infty \langle J_x(t) J_x(t+\tau) \rangle d\tau. \tag{5.1}$$

where $V$ and $T$ are the volume and temperature of the system respectively, $k_B$ is Boltzmann's constant, and $\langle J_x(t) J_x(t+\tau) \rangle = A(\tau)$ is the averaged but non-normalized HCACF of the x component of the instantaneous heat-flux, $J_x(t)$, at simulation time $t$. The HCACF measures the size and longevity of thermal fluctuations in the heat flux of a system in equilibrium, and is central to revealing the anticorrelated behavior that we describe below.

Simulations were performed with the large-scale molecular-dynamics software LAMMPS [157], using the Stillinger-Weber (SW) potential [158]. We have opted to use the SW potential in this work in part because it is commonly used to model heat transfer in silicon [148, 159], and for consistency with our previous work [103]. Although it overestimates the thermal conductivity [160], the Stillinger-Weber potential provides a reasonable match for the phonon dispersion relations, in particular for the acoustic phonons [161]. The results were averaged for sets of 15–20 simulations to mitigate the large uncertainty in the Green-Kubo approach [103], and smaller simulation cell sizes were used where possible to reduce computational expense. Simulation cell sizes varied between $40 \times 10 \times 10$ and $200 \times 10 \times 10$ unit cells for the simulations associated with Figs. 5.1 and 5.3, and $100 \times 10 \times 10$, and $100 \times 24 \times 10$ unit cells for the simulations in Fig. 5.2. This corresponds to dimensions $\sim 21.72 \times 5.43 \times 5.43$ to $\sim 108.6 \times 5.43 \times 5.43$ nm$^3$ for Figs. 5.1 and 5.3, and $\sim 108.6 \times 5.43 \times 5.43$ to $108.6 \times 13.03 \times 5.43$ nm$^3$ for Fig. 5.2, respectively. System sizes are indicated in the figures, and following common practice we report the fractional change in thermal conductivity compared to the pristine system, $\kappa_{\text{porous}}/\kappa_0$. We considered porous Si as illustrated in the inset of Fig. 5.1(a), where the pores are empty cylindrical regions "etched" from the top all the way to the bottom of the material. The systems were brought to and equilibrated at $\sim 300$ K, such that each system has its own initial configuration. Temperature equilibration is done in two parts: (1) the systems are brought to room temperature and allowed to thermally expand in the isothermal, isobaric ensemble (NPT) for 125 ps, and (2) equilibrated in the microcanonical ensemble (NVE) for an additional 125 ps, before any calculations are performed, also in NVE, for 10 ns. Equilibration is performed using a 0.5-fs interval, whereas a 2-fs time step is used to record the heat flux for the HCACF calculation. Transport properties reported in this work are computed along the $x$ axis, that is, along the long direction of each simulation cell [as shown in the inset in Fig. 5.1(a)], which is aligned with the [1 0 0] crystal direction. Additional simulation details can be found in our recent work [103].

For illustration of phonon propagation in the structures we simulate, we form Gaussian phonon wave packets and let them propagate while we monitor their trajectory. A Gaussian phonon wave packet is a propagating wave function formed by a linear superposition of plane waves weighted by a Gaussian distribution around a localized wave vector, and defined by

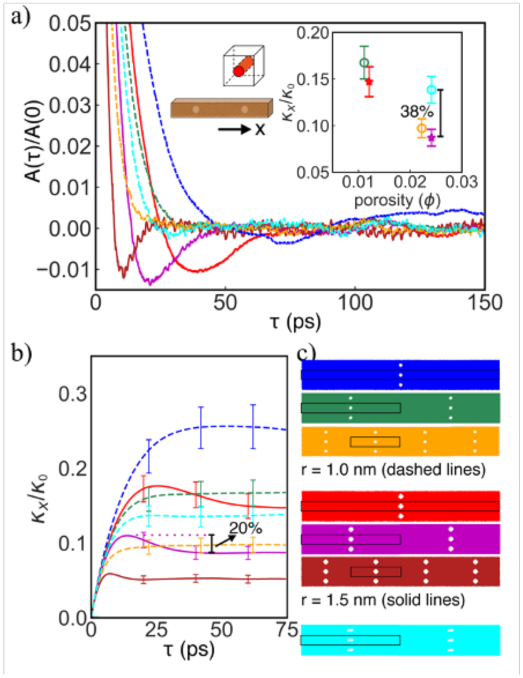

Figure 5.1: (a) Normalized HCACFs, $A(\tau)/A(0)$, for the geometries in (c). (Inset) $\kappa_x/\kappa_0$ (extracted at the 75-ps cutoff) as a function of porosity. (b) Evolution of $\kappa_x/\kappa_0$ as a function of the HCACF time, $\tau$. The dashed/solid lines correspond to geometries without/with anticorrelated heat flux (r = 1 nm/r = 1.5 nm). The cyan geometry has an elongated pore, with a vertical (y direction) spacing of 3.43 nm such that the neck size is equivalent to the geometries with r = 1 nm. It has the same porosity and number of scatterers as the purple geometry. The error bars correspond to the standard error across the simulations performed for each geometry. (c) Cross section of the xy plane (for a 108.6-nm width), for the geometries plotted in (a) and (b). The actual simulation cell is indicated by the black box.

$$u_{lj\mu\gamma} = \sum_q A_o \left(\frac{1}{\sigma\sqrt{2\pi}}\right)^2 e^{\left(\frac{q-q_o}{\sigma\sqrt{2}}\right)^2} \epsilon_{j\mu} e^{-i(r_l q+\omega_\gamma t)}. \tag{5.2}$$

Here, $u_{lj\mu\gamma}$ is the displacement of the $j$th atom in the $l$th unit cell along a direction $\mu$ (in x, y or z) for a given mode, $\gamma$. $A_o$ is the amplitude of the wavepacket, which can be tuned to a desired wavepacket energy.

The wavepacket is centered at a desired carrier wavevector, $q_o$, with an uncertainty in momentum space specified by $\sigma$. The term $\omega_\gamma$ is the frequency of the mode $\gamma$ at $q_o$, and $\epsilon_{j\mu}$

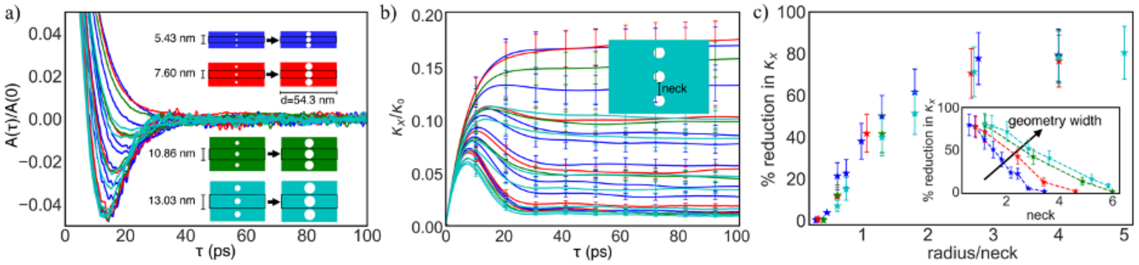

Figure 5.2: (a) $A(\tau)/A(0)$ for a range of geometries with the same number of pores, but varying pore radius and neck size. Simulation cell sizes are indicated in the inset. Pore radii vary between 1 and 2.5 nm for the geometries in blue, 1.5 and 3.59 nm for the geometries in red, 2.44 and 4.83 nm for the geometries in green, and 3.6 and 5.92 for the geometries in cyan. (b) Evolution of $\kappa_x/\kappa_0$ as a function of $\tau$ for the same geometries. (c) Plot of the percentage reduction in $\kappa_x$ due to the AC effect as a function of the radius to neck ratio. (Inset) Reduction in $\kappa_x$ as a function of the neck.

is the eigenvector of the $j$th atom along $\mu$ at the selected mode, $\gamma$. $r_l$ is a vector that points to the $l$th unit lattice, and $t$ is the time. The sum over $q$ is performed for all wavevectors in the first Brillouin zone that are commensurate with the compute cell. The phonon wavepacket simulations are centered at wavevectors $q_o \simeq 0.46, 0.93, 1.45, 1.74, 2.89, 4.05,$ and $5.21\ \text{nm}^{-1}$ along the [1 0 0] crystal direction for both the longitudinal and transverse acoustic modes ($\gamma$). Large simulation cells, consisting of 800 × 10 × 10 primitive cells for Si are used to precisely model the wavepackets with very fine uncertainty in momentum space ($\sigma = 0.05\ \text{nm}^{-1}$). The initial position of the atoms in the MD simulation is computed using Eq. 5.2 and the initial velocity is computed from the derivative of $u_{lj\mu\gamma}$ with respect to time ($v_{lj\mu\gamma} = \frac{d}{dt}u_{lj\mu\gamma}$).

In our wavepacket simulations, the system is initially at 0 K and the wavepackets are added with $A_o$ for each wavepacket tuned so that it raises the temperature of the system by around $\sim 5\ K$, rather than adding one phonon, $\hbar\omega$, of energy. The reason is that in the system sizes modeled, $\hbar\omega$ for wavepackets near the Brillouin zone center is too small to be resolved above the numerical noise, while a single $\hbar\omega$ would raise the system temperature by hundreds of Kelvin for wavepackets near the Brillouin zone edge. While the Green–Kubo calculations were performed at 300 K, performing the wavepacket simulations at lower energy ($\sim 5\ K$) helps keeping phonon thermalization at bay, such that the acoustic frequencies selected for the packets don't easily decay into other modes/frequencies due to anharmonicity. This allows us to observe the scattering behavior of specific wavevector phonons at the nanopores, as they are less likely to be obfuscated by anharmonic effects. The actual values of $A_o$ are included in the Supplemental Material [52].

## 5.4 The Anticorrelation Effect

In this section, we clarify and demonstrate the emergence of anticorrelations in the heat flux and quantify its effect on the thermal conductivity as a function of pore and neck sizes, as well as pore periodicity. Three sets of geometries are considered in Fig. 5.1 (1) pores with a 1-nm radius (blue, green, orange), (2) pores with a 1.5-nm radius (red, purple, and maroon), and (3) an elongated pore (cyan), such that the "neck," i.e., the distance between the edges of the pores perpendicular to the direction of transport (i.e., in the y direction), is 1 nm, but its porosity is the same as that of the geometry in purple. A cross section along the xy plane is shown in Fig. 5.1(c) for each of the geometries. The length of the simulation cell varies between $\sim 27.2$ and 108.6 nm, and the width along the y direction is $\sim 5.43$ nm for all of the geometries shown in Fig. 5.1. The moving average of the HCACFs and the HCACF cumulative integrals for these geometries are plotted in Figs. 5.1(a) and 5.1(b), respectively.

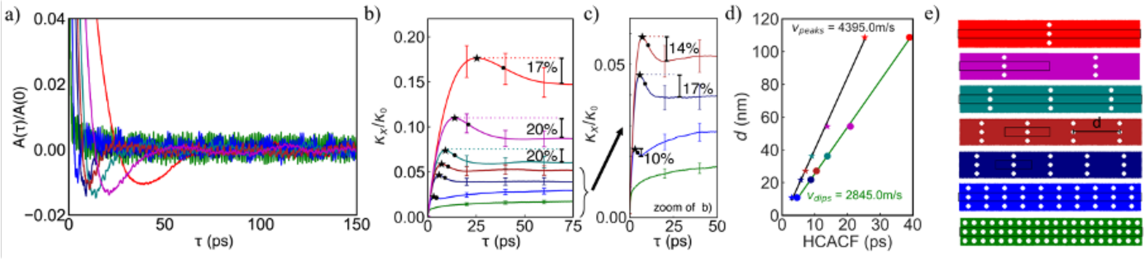

Figure 5.3: (a) $A(\tau)/A(0)$ for the geometries in (e). All geometries have the same radius, r = 1.5 nm, but different pore concentrations. (b) Evolution of $\kappa_x/\kappa_0$ as a function of $\tau$ for the same geometries. The percentage change in $\kappa_x$ due to AC is also indicated. (c) Zoom in of the higher-porosity geometries. (d) Plot of the HCACF time at which point each HCACF dip minima (circles) occurs as a function of the horizontal (x-axis) distance between the pores, and corresponding linear fit (green line); equivalent plot for the HCACF dip maxima (corresponding to where the HCACF becomes negative) (stars/black line). The slope of each line is also shown. The circles and stars match the color of the geometries. (e) Cross section of the xy plane for the geometries plotted in (a), (b), and (c).

The HCACF can be decomposed into contributions from short- and long length-scale interactions by fitting the HCACF to a sum of exponentials [144], from which the relaxation times for different length-scale phonon processes can be extracted. The rate of decay of the HCACF is thus a measure of the relaxation times of the heat-carrying phonons in the system. The typical HCACF for Si decays exponentially and monotonically to zero. In our simulations, the geometries with pore radius $r = 1$ nm [first triad of Fig. 5.1(c) structures], and the elongated pore geometry (cyan), all match this behavior; the small oscillations around zero stem from statistical noise in the HCACF and are to be expected [103, 162]. However, the HCACFs of geometries containing uniformly distributed 1.5-nm pores show anomalous behavior [second triad of Fig. 5.1(c)]. The HCACFs become negative and decay to zero from below the $x$ axis. The negative correlation or, equivalently, the anticorrelation [shown in Fig. 5.1(a) as the region of the HCACF that is below zero] in the narrow neck systems occurs when heat-flux fluctuations in one direction are followed by fluctuations in the opposite direction. This anticorrelation reduces the system's thermal conductivity, creating a peak in the cumulative HCACF integral at the point where the HCACF crosses the $x$ axis as shown in Fig. 5.1(b). We can observe in Fig. 5.1(a) that there are variations in the width, the minimum, and the time after which each minimum occurs for the geometries shown. How these characteristics are affected by the geometry is discussed later in the text. We begin by quantifying the reduction in thermal conductivity that is due to the anticorrelation of the heat flux.

As a metric of the reduction in the thermal conductivity, $\kappa$, due to the anticorrelation we consider the height of the peak in the cumulative HCACF integral above its final converged value. This value is indicated in Fig. 5.1(b) for the geometry in purple, and corresponds to a $21.5 \pm 6.5\%$ decrease in the accumulated $\kappa$. For a more realistic comparison of the decrease in thermal conductivity due to this effect, we considered a reference geometry (in cyan) without AC effects [its pores are elongated, such that the neck matches those of the geometries in the first triad (top) of Fig. 5.1(c)], but with equivalent porosity and number of scatterers as the geometry in purple [which belongs to the second triad (bottom) of Fig. 5.1(c)]. Comparing the two geometries, the purple system yields a $37.4 \pm 9.0\%$ decrease in thermal conductivity [see inset in Fig. 5.1(a)].

This estimated $37.4 \pm 9.0\%$ reduction in thermal conductivity suggests that using the HCACF peak height to estimate the effect of AC, which yields an estimated $21.5 \pm 6.5\%$ change in thermal conductivity [see Fig. 5.1(b)] underestimates the total reduction in $\kappa$. However, it would be too computationally expensive to compute similar elongated pore geometries to match each of the other geometries investigated herein, and henceforth we use the peak height to compare the impact of each geometry on the thermal conductivity. Overall, the AC effect provides an additional path to reduce the thermal conductivity, and the scale of the reduction is comparable to that achieved by increasing the number and surface area of the scattering features. For instance, the thermal conductivity of the geometry in red (with AC effects) has a similar porosity to the geometry in green (without AC effects), which has a higher number of scatterers and thus also surface area [see insets in Fig. 5.1(a) and Fig. 5.1(c)]. The same equivalence can be observed between the geometry in purple and the system in orange.

To further determine how the AC effect emerges with respect to the porous geometry, in Fig. 5.2 we examine multiple geometries with different pore and neck sizes. To vary the pore and neck sizes independently, we selected four equal- length sets of geometries, but with varying width (i.e., the y direction in the simulation cell), as illustrated in the insets in Figs. 5.2(a) and 5.2(b). This allows us to consider geometries with the same neck size, but different pore size, and vice versa, and in general various neck and pore sizes. Multiple pore sizes are considered for each set of the characteristic geometries of different widths [blue, red, green, and cyan as shown in the insets of Fig. 5.2(a)]. Pore sizes are indicated in the caption of Fig. 5.2. In all cases the distance between the pores' center is kept constant. The length of the simulation cell is also fixed at 54.3 nm. Figure 5.2 shows the HCACFs [Fig. 5.2(a)], and corresponding cumulative integrals [Fig. 5.2(b)] for the various geometries. Much larger dips in the HCACF can be engineered compared to Fig. 5.1, some affecting the cumulative integrals and the thermal conductivity in a drastic way.

If we again consider the height of the peak created in the cumulative integral of the HCACF [Fig. 5.2(b)] to estimate the effect of the AC in the heat flux, as we have done before, we find that for any given geometry type (blue, red, green, and cyan geometries), the percentage change in $\kappa$ plateaus as a function of the ratio between the pore radius and the neck [Fig. 5.2(c)]. The neck [see inset illustration in Fig. 5.2(b)] plays a major role in producing an anticorrelation in the heat flux. Figure 5.2(c) illustrates that (1) the AC effect is better correlated to the ratio of the neck to pore radius than to either the pore radius, or neck width alone [see inset in Fig. 5.2(c)]. In other words, a smaller pore system requires a smaller neck to yield the same dip minima as a larger pore system, and the ratio between the neck and pore diameter is a better metric of the total thermal conductivity than either the neck or pore diameter alone (see Fig. S5 in the Supplemental Material [40]). This is consistent with results from Monte Carlo simulations as well [163]. Similarly, we intuitively expect a smaller neck and a larger radius to reflect (back) phonons more effectively and create a stronger anticorrelation effect. The results in Fig. 5.2(c) further indicate that beyond a certain point it makes no difference if the neck is further reduced for a given pore size. One possibility for this plateau, which is reached at a $79.3 \pm 12.6\%$ reduction in $\kappa$ for a fixed pore periodicity of 54.3 nm [see Fig. 5.2(c)], is that a limit is reached at which point the remaining phonons, with short mean-free paths (smaller than the pore periodicity), will thermalize before anticorrelated behavior can take place.

It follows from Fig. 5.2 that the extent to which the heat flux is anticorrelated can be controlled by carefully selecting the pore and neck sizes, that is, the lateral spacing between pores. Next, we show that the spacing between the pores in the direction of transport can also affect the location of the HCACF dip minima. We consider a set of geometries of periodically arranged pores, depicted in Fig. 5.3(e), with the same pore radius (r = 1.5 nm) but varying pore density. All of the geometries in Fig. 5.3(e) exhibit anticorrelated heat-flux behavior to some extent, with the exception of the higher pore concentration geometry (in green). Each of the dips in the (moving average of the) HCACFs shows up at a different instance of the HCACF time, as seen in Fig. 5.3(a). Similarly, the HCACF cumulative integral [Fig. 5.3(b)] shows peaks (labeled with stars) moving to the left. The percentage change in thermal conductivity due to the AC effect is indicated in Figs. 5.3(b) and 5.3(c). Notice that the peaks occur earlier than the dip minima (labeled with dots), as they correspond to the instance where the HCACF becomes negative. Interestingly, we find that there is a linear correlation between the distance between the pores, $d$ [see Fig. 5.3(e)], and when the anticorrelation dip minima and integral peak maxima occur [Fig. 5.3(d)]. The slopes of the aforementioned relationships are also indicated, in units of velocity.

The dip minima indicate the simulation time intervals at which the anticorrelation effect is strongest. Using this measure, we find the slope of the correlation between when the anticorrelation effect is strongest (i.e., the dip minima) and d to be $\nu_{dips} = 2845$ m/s. (If instead we use the peaks of the cumulative HCACF, we obtain $\nu_{peaks} = 4395$ m/s.) As a reference to the reader, near the $\Gamma$ point of the Si phonon spectrum obtained with the Stillinger-Weber potential, the velocities for the (dominant) longitudinal acoustic and transverse modes are $\sim 8100$ and $\sim 5000$ m/s, respectively, yielding an average speed of $\sim 6033$ m/s for the three modes. There is clearly a linear relation between the appearance of the anticorrelation effects and the pore distances.

## 5.5 The Heat-Trapping Origin of the Anticorrelation Effect

To investigate the origin of the AC effect on the porous structures, wave packets centered at a wave vector $q_o$, as detailed in Sec. II, are propagated through two sets of systems with pore radii of 1 nm [left-hand plots of Figs. 5.4(a)–5.4(h)] and 2 nm [right-hand plots of Figs. 5.4(a)–5.4(h)] with corresponding 3.4- and 1.4-nm necks. When we evaluate the thermal conductivity of the structures in the left and right columns with the Green-Kubo approach, the structure in the left column does not show AC effects, whereas the one in the right does. Both longitudinal and transverse modes are considered for several values of $q_o$, for which heat maps are obtained showing the evolution of the kinetic energy of the wave packets in the geometries during simulation time. The values of $q_o$ are noted in each subfigure, and they are also indicated by the vertical lines in Fig. 5.4(k) on the $q$ axis, where the frequencies and velocities of the modes are plotted as well. This is shown in Figs. 5.4(a)–5.4(h) for the transverse mode with polarization perpendicular to the pore height [labeled TA $\perp$ in Fig. 5.4(i)]. The longitudinal (LA) and parallel transverse (TA $\|$) modes, as well as other $q_o$-centered packets for the same (TA $\perp$) mode are shown in the Supplemental Material [40]. In the heatmaps [Figs. 5.4(a)–5.4(h), 5.4(j), and 5.4(l)] the ordinate indicates the propagating time and the abscissa the length direction. The positions of the pores are indicated by the white vertical lines and are located at 216 and 270 nm.

From Figs. 5.4(a)–5.4(h) it is evident that (1) the amount of heat reflected at the first pore is consistently greater for the larger pore, narrower neck geometries (center column in Fig. 5.4), and (2) the amount of heat that is transmitted after the second pore is significantly reduced for the same narrow-neck geometries. As a consequence of hindering

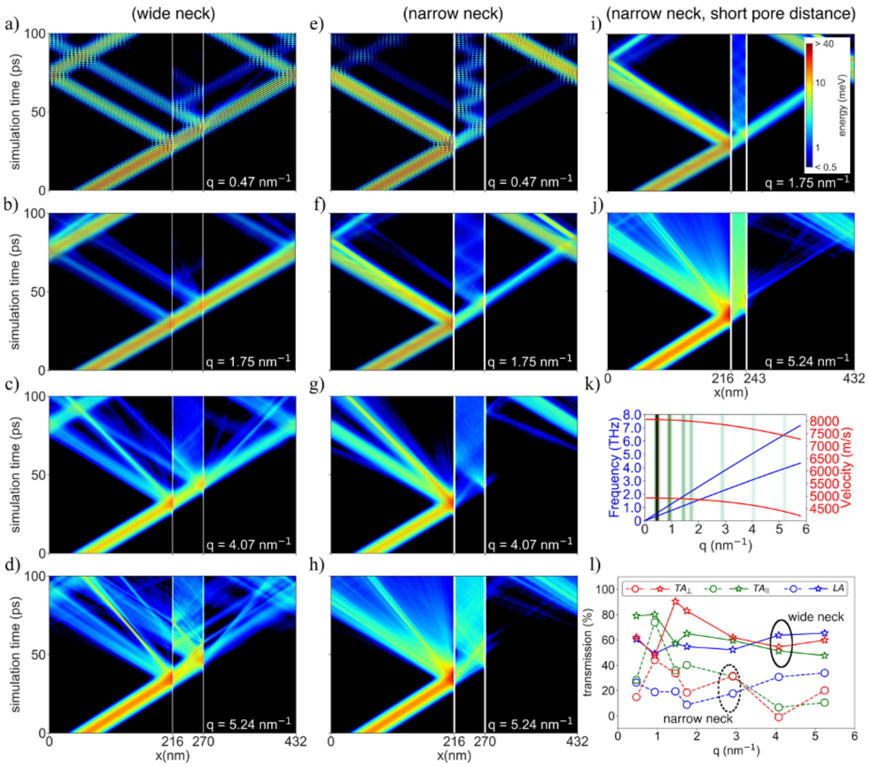

Figure 5.4: (a)–(h) Heatmap of the evolution of the wave-packet kinetic energies during the simulation time along the width of the nanoporous geometries. (i) Transmissions (i.e., the amount of kinetic energy that goes through) on the left-hand side pore, for the 2-nm (dashed lines with circle markers) and 1-nm (solid lines with star markers) pore geometries. (j) Heatmap for a wave packet centered at $q_o = 1.75$ nm$^{-1}$ with a pore distance of 27 nm. (k) Dispersion relation showing the acoustic transverse and longitudinal mode frequencies, as well as velocity. (l) Heatmap for a wave packet centered at $q_o = 5.24$ nm$^{-1}$ with a pore distance of 27 nm. (m) Example of geometry with a packet propagating through it.

heat propagation through the spacing between the pores, it can also be seen that for the narrower neck geometry (center column of Fig. 5.4) phonons become trapped between the pores, causing the packets to oscillate back and forth. This effect is also clearly shown to be $q$ dependent, in that it is more or less prevalent at different wave vectors; roughly, the heat blocking and accumulation becomes stronger for phonons with larger wave vectors. This is most noticeable by considering the trans- mission at the second pore (i.e., the amount of kinetic energy that reaches past the second pore, located at 270 nm), which disappears for

$q_o$ values of 4.07 and 5.24 nm$^{-1}$, but is present at other values of $q_o$.

We remark that, in the case of the wave packets, the pore neck/size controls the amount of energy trapped between the pores not only by not allowing heat to escape once through the first pore, but also by limiting the amount of heat that goes through the first pore. For instance, for $\mathrm{q_o} = 4.07\mathrm{nm}^{-1}$ in the narrow-neck structure [Fig. 5.4(g)] the intensity of the heat bouncing back and forth is somewhat less than that in the wider neck case [Fig 5.4(c)]; however, this is most likely because most of the kinetic energy is reflected at the first pore, and less energy is therefore available to be reflected between the pores. The multiple reflections observed in the geometries with narrower neck/larger pores corroborate the EMD simulation results discussed in the previous section, which exhibit HCACFs with negative values evidencing an anticorrelation of the heat flux. In short, like the packets which bounce back and forth between the pores for geometries with narrower neck, in the equilibrium calculations, heat similarly fluctuates back and forth between the pores. As the necks become smaller and the pores larger, more heat is trapped and scattering between the pores is intensified. This agrees with the observations in Fig. 5.2, which show an increase in the (proportional) amount of anticorrelated heat flux for narrower neck geometries (over positively correlated heat flux). In Fig. 5.2(a), this is evident in how negative the HCACF becomes as the pore sizes increase and necks decrease.

The transmission through the first pore as a function of $q_o$ is shown in Fig. 5.4(i) (see the Supplemental Material [40] for calculation details) for all acoustic modes. Overall, the trans- mission is lower for larger wave vectors (and thus also higher frequencies). This could account for why $\nu_{dips}$ [Fig. 5.3(d)] is *less than* exactly half the speed of the average of the acoustic modes. In other words, if higher $q_o$ phonons are most noticeably trapped between the pores, the overall velocity of these modes would be lower than their velocity at $\Gamma$, because the velocity of the modes decreases a function of q [see Fig. 5.4(k)]. In fact, higher-frequency modes are more likely to be scattered between the pores, while larger wave vectors are less likely to "see" small-size features [43]. That said, the increased scattering rate between pores for larger pores/smaller necks is nevertheless still present at low wave vectors [see Fig. 5.4(a)]. Due to their weaker Umklapp scattering, phonons with small wave vectors are known to contribute more to the overall thermal conductivity than large wave-vector phonons. On the other hand, it is also known that the contribution of higher $q$ values becomes more noticeable once lower $q$ values have been scattered, for instance due to defect scattering [122, 164, 165, 166].

The trend observed in Fig. 5.3(a), whereby the HCACF dip moves left as the periodicity between the pores becomes smaller (i.e., as the pores become closer together in the direction of thermal transport) can be understood as a function of the maximum possible correlation distance (and thus time) for heat scattering between the pores in each case. Consider the heat trapped between the pores in the packet simulations: the distance between the pores dictates the maximum distance heat may travel from the moment it first crosses the left-hand side pore until it finally dissipates. For this reason, the maximum correlation interval, $\tau$, is smaller when the pores are closer together: see Figs. 5.4(f) and 5.4(h), where the pores are 54 nm apart, in contrast with Figs. 5.4(j) and 5.4(l), in which the pore separation is 27 nm. In other words, this is why the HCACF correlation time, $\tau$ , shifts to the left in Fig. 5.3(a), as the geometries become more densely packed [see corresponding geometries in Fig. 5.3(d)]. In short, Fig. 5.3(d) shows that the duration of heat-flux fluctuations before the reversal process scales linearly with the distance, d, between the ranks of pores—indicating that the fluctuation duration depends on the time of flight to strike the pores and that pores must be causing the reversal. Finally, a reduction in the $x$ component of the wavepackets' velocity after scattering at the pore surfaces, as observed in Ref. [148], can also be observed in this work. In other words, the split velocity observed in some of the packets in Fig. 5.4 is likely the wave packet being scattered laterally by the curved pore, which allows for different $x$-directed velocities (i.e., in the direction of propagation explicitly shown in the heat map). Given that the simulation cell has a finite width $w$, there are only a set number of directions $\theta$ that a lattice wave of a wavelength can travel, while remaining coherent with itself across the periodic boundaries of the computed cell. Mathematically the periodic boundaries impose the condition $n\lambda = w \sin\theta$, where $n$ is an integer, $\lambda$ the wavelength of the carrier wave, and $\theta$ the direction of the wave vector relative to the long axis of the simulation cell. In Fig. 5.4 the wavepackets have wavelengths of $\lambda = 13.4, 3.6, 1.5,$ and 1.34 nm, and the cell width is $w = 5.4$ nm. For the longest-wavelength wave packet there is no oblique path that is commensurate with the box boundaries (the equation above is only satisfied for $\theta = 0$). For the next-largest wavelength of $\lambda = 3.6$ nm, there is one oblique direction possible at $\theta = 41.7$. The wave packet traveling along this direction would have an x component of velocity that is 0.75 of that of the incident wave packet with $\theta = 0$, and so would leave a trace on the heat map with a slope 1.34 times steeper than the incident wave. This second possible ray is seen in Figs. 5.4(f) and 5.4(j). The other waves in the wave packet would not be commensurate with the box boundaries and so the wave packet reflected along this oblique direction will be dispersed. For the wave packets with $q = 4.07$ and $5.24$ oblique reflections are permitted that would leave traces on the heat map with slopes of $[1.04, 1.22, 1.94]$ and $[1.03, 1.12, 1.34, 2.18]$ times that of the incident wave packet, and oblique reflections corresponding to these are seen in the heat maps for these wave packets. (See Fig. S5 and the Supplemental Material [52] for more details.) We note, however, that there are still some issues that are not yet clear and would be revisited in future studies, for example why some transmissions show an increase and then a decrease as a function of $q$.

## 5.6 Ray-Tracing Model

We develop a simple analytical model, as a gedanken experiment, to show how different types of phonon scattering manifest as signatures in the HCACF. The purpose of this is to ensure that we are correctly interpreting the anticorrelation features in the HCACF seen in panel (b) of Figs. 5.1–5.3. This model is not intended to be predictive, but to illustrate how heat trapped between the pores, as shown by the wave-packet simulations (Fig. 5.4), can lead to the negative values in the HCACF. We consider a simple statistical model of a gray population of heat-carrying acoustic phonons that pop in and out of existence completely uncorrelated (for example from scattering with a bath of optical phonons, although the details of this are not required for this exercise) with a lifetime $\tau_o$. Each acoustic phonon contributes a stepwise heat current, $J_p(\tau)$, which has an autocorrelation function $A_p(\tau)$ [dashed blue and green lines in Fig. 5.5(a), respectively], that is positive and linearly decreases over time. The instantaneous heat current of the entire system is the superposition of $J_p(\tau)$ from all active phonons, but as the acoustic phonons are not correlated with one another, the system's HCACF is simply the phonon density times the average of each phonon's correlation with itself. The dashed red line in the lower panel of Fig. 5.5(a) shows the integrated average of $A_p(\tau)$. To explore the effect of specular (perfectly correlated) scattering on the HCACF, we assume that each acoustic phonon experiences some scattering at a time $\alpha\tau_o$ (where $0 < \alpha < 1$) during its flight, that reflects the phonon, reversing its direction, and causing the flux and HCACF plotted with solid lines in Fig. 5.5(a). This correlated scattering allows the autocorrelation to become negative. We have further considered a Poisson distribution of lifetimes $\tau_o$, and the distribution of scattering times, $P_\alpha$, such that the duration of the AC is controlled by the scattering time, $\alpha\tau_o$, and the amount of the AC is controlled through the probability of reflection at $\alpha$, $P_\alpha(\alpha)$. The Poisson distribution implies that the scattering event that annihilates the phonon is completely uncorrelated with the event that created it, and is commonly used in kinetic Monte Carlo simulations to describe the free path distribution of particles in an ideal gas [167]. Averaging over a Poisson distribution of phonon lifetimes and directions, and also the distribution of scattering times one can show that this correlated scattering reduces the thermal conductivity by

$$\frac{\kappa_x}{\kappa_o} = \int_0^1 P_\alpha(1-2\alpha)^2 d\alpha \tag{5.3}$$

where $P_\alpha$ is the probability distribution that a phonon is reflected at fraction $\alpha$ of the way through its flight. Additional details, and a derivation of the model are included in the Supplemental Material [52].

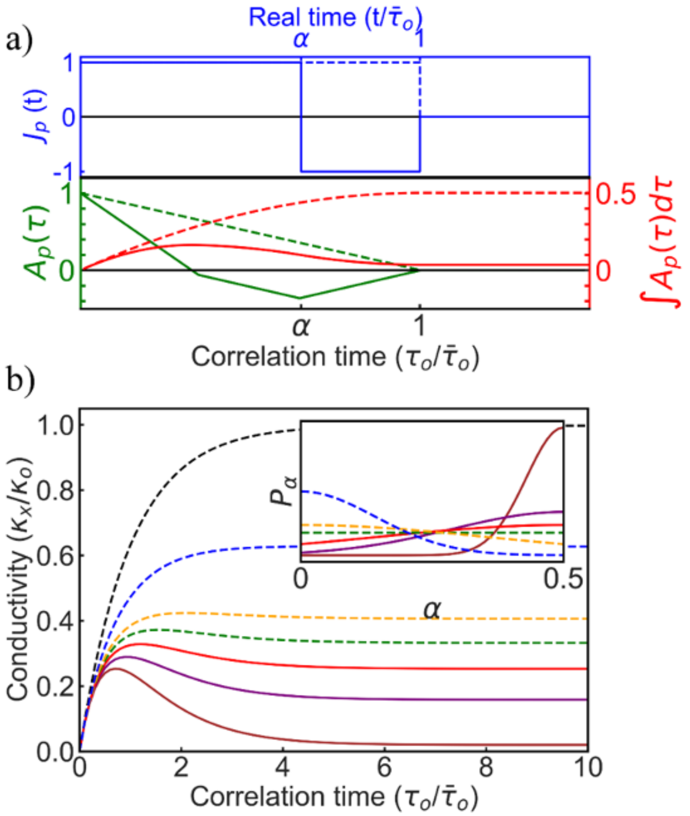

Figure 5.5: Stochastic model results. (a) (Solid blue) Contribution to the heat current from a single phonon with lifetime $\tau_o$ that is reflected after time $\alpha\tau_o$, its ACF (solid green), and the integral of its ACF (solid red). The dashed lines show the corresponding functions if the phonon was not reflected. (b) The net HCACF averaged over all $\tau_o$, and $\alpha$ for varying scattering probability distributions (inset). The black line is for no scattering. The green curve is for scattering with a uniform probability in $\alpha$, and shows a 10.6% dip in the ACF due to anticorrelation. In purple and brown, we show the case where the scattering probability is strongly skewed to the middle of the phonon lifetime with much larger dips in the ACF.

During diffuse scattering the incident and scattered phonon trajectories are uncorrelated which in the stochastic phonon model has the same effect as reducing the mean phonon lifetime $\bar{\tau}_o$. This hastens the decay of the HCACF, reducing thermal conductivity, but it does not lead to the HCACF becoming negative. Specular scattering on the other hand can be significantly more resistive for heat transport in geometries that allow anticorrelation effects, particularly if phonons live long enough after they are reflected that they undo the heat current they generated before scattering. Enforcing specularity causes anticorrelated heat-flux fluctuations similar to those observed in MD.

Figure 5.5(b) shows the collective effect on correlated scattering on the net HCACF computed for a series of $P_\alpha$ distributions (plotted inset) for which the probability of scattering is shifted systematically from near the ends of the phonon flight to its middle. If the likelihood of reflection is evenly distributed throughout each phonon's lifetime [$P_\alpha = 1$, green line in Fig. 5.5(b)] then the total thermal conductivity is reduced to one-third of its intrinsic value, and a 10.6% dip emerges in the integrated HCACF. A larger reduction in the thermal conductivity and a more prominently peaked integrated HCACF are obtained when the probability of reflection is weighted towards the middle of the phonon flight, i.e., $\alpha = 0.5\tau_o$, to maximize the anticorrelation time (e.g., the purple and brown plots in Fig. 5.5(b) show 45 and 92% reduction, respectively, similar values to those observed in some of the MD simulations). The key result from this model is that the anticorrelated heat flux observed in MD can only be achieved if phonons live long enough after they are reflected that they undo the heat current they generated before scattering. In the wave-packet simulations the phonon reflections are not limited to a single back and forth oscillation, and instead multiple reflections are observed. When multiple reflections are included in the ray-tracing model multiple oscillations show up in the computed ACFs. As only one dip is observed in the ACF of the Green-Kubo molecular dynamics simulations (the first panel of Figs. 5.1–5.3) this implies that, in contrast to the wave-packet simulations, at 300 K phonons only remain (anti)correlated for about one reflection. One reason for this is that the wave-packet simulations are performed at low temperatures and thus phonons have a much longer mean-free path than in the Green-Kubo simulations at 300 K. A second probable reason is that, since the pores are cylindrical, the wave packets can reflect off the pores in different directions, as can be seen, for instance, in Fig. 5.4(h). A phonon's contribution to the ACF along the $x$ direction is proportional to its velocity along $x$ squared. Thus elastic scattering that bends a wave packet away from $x$- will quash the $x$-direction HCACF.

In light of the model, we can now explain the behavior observed in Figs. 5.2 and 5.3 regarding dip "height" and "location." In Fig. 5.2, what causes the peaks to change height is the density of inversely correlated phonons due to changes in pore size and neck width, which control the strength of the reflections. In Fig. 5.3, the location of the peaks shifts according to the duration for which the phonons are inversely correlated, which is in turn a function of the distance between the pores. For the geometry in green, the distance between the pores along the direction of transport, $d$, is small and, therefore, the AC effect is not visible on the HCACF. In previous work, we concluded that merely reducing the *line of sight* of phonons, i.e., narrowing the region available for phonon propagation, is the most important mechanism in reducing thermal conductivity in nanoporous materials [103]. The same mechanism is at play here, with the additional reduction effect due to the anticorrelation of the backscattered phonons.

Finally, we note that the effect we observe is a negatively correlated heat current which undoes its own work, which could happen in the case of coherent, or incoherent phonon propagation. Phonons need to be anticorrelated (i.e., propagate in the exact inverse direction), and in that way, they do "interfere" with each other in that they annihilate each other in the heat-transfer accountancy. This coherence is coherence over time, not the spatial coherence and wave superposition that leads to constructive/destructive interference. This is independent of wave-coherent or -incoherent transport conditions (superposition and constructive/destructive interference), and it can show up in either case. In fact, the simple model above demonstrates that an "incoherent" particle phonon picture can explain this. However, as phonon transport involves a range of phonon mean-free paths and coherence lengths, it could be possible that both effects are present. In our MD simulations it is quite possible that phonons can scatter specularly on the pores, reflect, and travel backwards to meet the previous array of pores before they undergo phonon-phonon scattering and lose coherence (the mean-free path for scattering in Si is $\sim$ 130 nm, more than twice as large as the pore separation). In that case they can interfere coherently with "themselves" and undo their work. Physically this leads to heat trapping within the pore regions, as suggested by our wave-packet simulations in Fig. 5.4. It is also possible that phonons with short coherent lengths can undergo an incoherent diffusive reflection, but with a sizable $x$-directed component and reflect backwards. Our results indicate that the magnitude of the AC effect is tied to the neck to pore ratio, not merely the neck size. This suggests that scattered phonons, possibly from across the spectrum, affect the negatively correlated HCACF regions. These phonons do not need to be spatially coherent, but could lose coherence after scattering and yet travel back and forth between the pore, thus giving rise to the "AC" effect in time, essentially canceling their contributions to thermal conductivity.

## 5.7 Conclusion

To conclude, we have shown that special arrangements of closely packed pores in nanostructured Si can lead to anticorrelation effects in the heat flux, due to the specular backscattering of phonons at the pores. This can result in additional thermal conductivity reductions of up to $\sim$ 80% for certain porous geometries. We surmise that AC effects could be present at experiments reporting remarkable thermal conductivity reductions in Si nanomeshes [68, 168]. To investigate the origin of the anticorrelated behavior of the heat flux, we propagated wave packets through two sets of geometries (with and without AC effects). These indicate that heat can become trapped between the pores. We have observed the AC effect in (wave-based) MD simulations and have been able to replicate it with a simple (particle-based) model assuming specular reflection between the pores. References [142, 169] indicate that coherent reflections are only possible when surface roughness is on the order of 2–3 atomic layers, and that other-wise boundary scattering is incoherent. This is consistent with the degree of roughness in our simulations. However, while specular reflections are a necessary requirement for coherent interference [142], the mere presence of specular reflections is not in itself sufficient evidence that phonon (waves) are interfering with each other or that the AC effect is due to phonon coherence. It is possible that both coherent wavelike phonons, and incoherent particle-like phonons are present, and both to some degree undo their own work of heat propagation.

We have furthermore determined that the AC can be controlled in terms of both the amount and duration of anticorrelated specular phonon scattering. The pores provide two functions: the periodicity (along the transport direction) controls the lifetime over which a phonons' momentum is correlated, and the packing, determined by pore sizes and necks (perpendicular to transport), controls the strength of correlated phonon reflections. These functions can be engineered by tuning the spacing/periodicity between pores along the transport direction, and the pore and neck sizes, respectively. Our results suggest that the AC effect is determined by the diameter/neck ratio, and AC effects are observed for necks of at least up to $\sim 6$ nm. This result suggests that the porous structures can be scaled to such technologically feasible pore/neck sizes, making it easier to be used as a design tool to control thermal conductivity beyond traditional boundary scattering.

# Chapter 6

# Nondiffusive Correction Model to Estimate the Effective Thermal Conductivity in Nongray, Nanostructured Materials

## 6.1 Abstract

Nanostructured materials enable high thermal transport tunability, holding promises for thermal management and heat harvesting applications. Predicting the effect that nanostructuring has on thermal conductivity requires models, such as the Boltzmann transport equation (BTE), that capture the nondiffusive transport of phonons. Although the BTE has been well validated against several key experiments, notably those

on nanoporous materials, its applicability is computationally expensive. Several effective model theories have been put forward to estimate the effective thermal conductivity; however, most of them are either based on simple geometries, e.g., thin films, or simplified material descriptions such as the gray-model approximation. To fill this gap, we propose a model that takes into account the whole mean-free-path (MFP) distribution as well as the complexity of the material's boundaries. We validate our approach, which is called the "nondiffusive correction" (NDC) model, against full BTE simulations of a selection of three base materials (GaAs, InAS and Si) containing nanoscale porosity, obtaining excellent agreement in most cases. While the key parameters of our method, associated with the geometry of the bulk material, are obtained from the BTE, they can be decoupled and used in arbitrary combinations and scales. We tabulated these parameters for a few cases, enabling the exploration of systems that are beyond those considered in this work. Providing a simple yet accurate estimation of thermal transport in nanostructures, our work sets out to accelerate the discovery of materials for thermal-related applications.

## 6.2 Introduction

Engineering semiconducting nanostructures has enabled unprecedented control on nanoscale heat flow for a wide range of applications, from microelectronic devices [53, 54] to optoelectronics [55, 56] and thermoelectrics (TE) [57, 58, 59, 60]. Successful control of thermal transport in TE nanomaterials has been shown in thin films, [43, 44] superlattices, [47, 48, 49] nanowires [42, 42], nanomeshes [45, 46], nanocomposites [65, 66], and nanoporous structures [50, 51, 52], all of them featuring extremely low thermal conductivity.

In multiphase materials that have macro- or micro- scale heterogeneity, heat transfer is often modeled by replacing the detailed microstructure with a homogeneous *effective medium* that has thermal conductivity matching the macroscopic thermal conductivity of the real material. For coarse microstructures, where heat conduction is diffuse and Fourier's law holds, analytical models exist to supply the thermal conductivity of this effective medium based on the volume fraction and conductivity of the constitutive phases in the material it replaces. For example, the effective medium thermal conductivity of materials containing cylindrical pores is given by the Maxwell-Garnett theory [77], which predicts the thermal conductivity suppression $(1-\phi)/(1+\phi)$, due to the presence of pores with a total volume fraction $\phi$.

While accurate models exist for the diffusive regime, conceiving their nanoscale counterparts is more challenging. In fact, nondiffusive thermal transport, which is captured by the Boltzmann transport equation (BTE) [101, 170], needs to include the whole distribution of phonon mean-free-paths (MFP)—an aspect that has been difficult to capture in analytical models. For this reason, early approaches are based on single-MFP approximations, e.g., gray material approximation [84] or simple geometries [171].

In this work, we fill this gap by providing a simple analytic model for the effective thermal conductivity, $\kappa_{\text{eff}}$, that includes the full MFP distribution and is suitable from the nano- to the macro- scales and for complex structures. Our approach, referred to as the "NonDiffusive Correction" (NDC) model, is based on the logistic approximation of both the bulk cumulative thermal conductivity and the phonon suppression function. In practice, it is a simple formula that provides $\kappa_{\text{eff}}$ given the relevant geometry's feature size, the characteristic bulk MFP, and the macroscopic suppression factor. All these parameters are computed for a few cases, using the BTE and Fourier's law, and tabulated, enabling a wide space of systems to be explored. We validate the NDC model against BTE calculations on Si, GaAs and InAs, obtaining excellent agreement in most cases.

The paper is structured as follows. We first report on BTE calculations, applied to Si, GaAs, and InAs membranes with different temperatures and porosities. Then, we detail on the building blocks leading to the NDC model, provided in different sections: i) The derivation of the formula for $\kappa_{\mathrm{NDC}}$, validated against BTE simulations, ii) the calculation of the material diffusive limit (MDL) for a given geometry, and iii) the integration of the MDL and the nondiffusive correction to provide a material- and scale- free model for $\kappa_{\mathrm{NDC}}$. Finally, we outline the procedure to assess $\kappa_{\mathrm{eff}}$. The proposed model may help identify novel nanostructures with minimal computational efforts, thus accelerating the search of materials for thermal-related applications.

## 6.3 BTE modeling

We employ the recently developed anisotropic-MFP-BTE, which solves the BTE for uniformly space vectorial MFPs, $\mathbf{F}_{ml}$, i.e.

$$\mathbf{F}_{ml} \cdot \nabla \Delta T_{ml}^{(n)} + \Delta T_{ml}^{(n)} = \sum_{ml} \alpha_{ml} \Delta T_{ml}^{(n-1)}. \tag{6.1}$$

We compute space-dependent nondiffusive transport using the steady-state BTE in its temperature formulation

$$\tau_\mu \mathbf{v}_\mu \cdot \nabla \Delta T_\mu + \Delta T_\mu = \sum_{\nu} \alpha_\nu \Delta T_\nu, \tag{6.2}$$

where $\alpha_\nu = \left[\sum_k C_k/\tau_k\right]^{-1} C_\nu \tau_\nu$, $\mathbf{v}_\mu$ is the phonon group velocity, $\tau_\mu$ the scattering time and $\Delta T_\mu$ the deviational phonon pseudo-temperatures, which are a measure of the non-equilibrium population of phonon mode $\mu$ .[172, 173] Eq. 6.2 is solved iteratively, the first guess being given by diffusive equation.

Upon convergence, the effective thermal conductivity is computed by using Fourier's law

$$\kappa_{\text{eff}} = -\frac{L}{\Delta T A} \int \mathbf{J} \cdot \hat{\mathbf{n}} dS. \tag{6.3}$$

Here, $A$ is the area of the hot contact and $\hat{\mathbf{n}}$ is its normal. The term $\mathbf{J}$ is the heat flux, given by $\mathbf{J} = \sum_\mu C_\mu \mathbf{v}_\mu \Delta T_\mu$, where $C_\mu$ is the heat capacity. The group velocities, scattering times as well heat capacities are computed from first principles using *AlmaBTE*. [117] The phonon dispersions as well as the scattering times were computed on a 30 × 30 × 30 point Brillouin zone mesh; the second and third-order interatomic force constants for pristine materials, computed with density functional theory using the virtual crystal approximation, are obtained from the *AlmaBTE* materials database. [117] To better understand the effect of the geometry on $\kappa_{\text{eff}}$, we also compute the mode-resolved phonon suppression function, given by

$$S_\mu = -\frac{L}{\Delta T A \tau_\mu v_{\alpha,x}} \int \Delta T_\mu dS, \tag{6.4}$$

so that $\kappa_{\text{eff}} = \sum_\mu C_\mu v_{\mu,x}^2 \tau_\mu S_\mu$. [173]

For computational efficiency, equation 6.2 is solved using the anisotropic MFP-BTE (aMFP-BTE). [173] The aMFP-BTE is based on the interpolation of $\Delta T_\mu$ onto the space of the vectorial MFPs, given by $\mathbf{v}_\mu \tau_\mu$; in practice, equation 6.2 is for a uniform spherical grid whose point locations are labeled by $\mathbf{F}_{ml}$, $m$ and $l$ labeling MFP and polar angle, respectively. Within this formalism, phonon temperatures ($\Delta T_{ml}$), heat flux ($\mathbf{J}_{ml}$) and suppression functions ($S_{ml}$) are defined on a polar surface. In the rest of this work, however, we are interested in angularly averaged quantities; notably, the MFP-dependent suppression function is given by $S_m = \sum_l S_{ml}$.

We have computed the effective thermal conductivity, $\kappa_{\mathrm{eff}}$, of InAs, GaAs, and Si membranes containing an array of cylindrical nanopores with different shapes, sizes, and spacings which we parameterize in terms of the total pore fraction, $\phi$, and the array periodicity, L. The thickness of the membrane is considered infinite. Figure 6.1 shows the distribution of thermal flux for one such case, GaAs with porosity 0.25 and L = 50 nm. As we expect, most of the heat is concentrated in the space between the pores. Figures 6.1 and 6.3(bottom-right) show plots of $\kappa_{\mathrm{eff}}$ of GaAs with for a pore spacing of L = 100 nm with porosities of 0.05 and 0.25 over a wide range of temperatures. We note that the conductivities obtained from BTE are significantly lower than those from Fourier's law due to the effect of ballistic scattering of long mean free path phonons which is not captured in Fourier's law. The thermal conductivity obtained using Fourier's law only depends on the pore fraction, not the pore spacing, and matches the macroscopic effective medium theory, $\kappa_{\mathrm{eff}}/\kappa_{\mathrm{bulk}} = (1-\phi)/(1+\phi)$. We will use these simulations to validate our proposed model, as detailed in the next sections.

## 6.4 Effective Medium Theory for Nongray Materials

In this section, we present a reduced-order model for approximating $\kappa_{\mathrm{eff}}$ in nanostructures with aligned pores. Assuming an isotropic intrinsic MFP distribution, K($\Lambda$), the

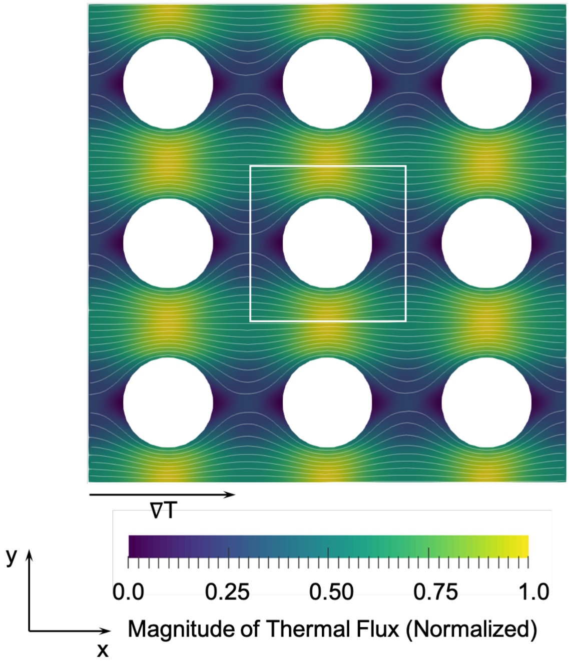

Figure 6.1: Magnitude of the thermal flux in GaAs containing aligned cylindrical pores at an average temperature of 300 K. The system has porosity $\phi = 0.25$, the spacing between pores is L = 50 nm and the white box shows the unit cell. The heat flux is higher in the constriction between the pores, and in addition to creating the constriction, the pores also exert a drag on the heat flux in this region.

effective thermal conductivity of materials after nanostructuring is written in terms of the suppression of the material's thermal conductivity distribution

$$\kappa_{\text{eff}} = \int_0^{\infty} \mathrm{K}(\Lambda) S(\Lambda) d\Lambda. \tag{6.5}$$

In Eq. 6.5, $S(\Lambda)$ is the phonon suppression function, a tool describing the degree of reduction of heat transport with respect to the bulk for a given intrinsic MFP $\Lambda$. [171] In the diffusive regime, $S(\Lambda \to 0) \approx \frac{1-\phi}{1+\phi}$, which is in agreement with Maxwell-Garnett prediction, while in the ballistic regime, $S(\Lambda \to \infty) \propto L_c \Lambda^{-1}$, [174] where $L_c$ is the mean line-of-sight between phonon scattering event with the nanostructure. Integrating Eq. 6.5 by parts, we obtain

$$\kappa_{\text{eff}} = \kappa_{\text{bulk}} \left[ S(\infty) - \int_0^{\infty} \alpha(\Lambda) g(\Lambda) d\Lambda \right], \tag{6.6}$$

where the normalized cumulative thermal conductivity, $\alpha(\Lambda)$, is defined as

$$\alpha(\Lambda) = \frac{1}{\kappa_{\mathrm{bulk}}} \int_0^{\Lambda} \mathrm{K}(\lambda) d\lambda, \tag{6.7}$$

and

$$g(\Lambda) = \frac{\partial S(\Lambda)}{\partial \Lambda}. \tag{6.8}$$

We note that

$$S(\infty) = S(0) + \int_0^{\infty} g(\Lambda) d\Lambda, \tag{6.9}$$

therefore, Eq. 6.6 turns into

$$\kappa_{\mathrm{eff}} = \kappa_{\mathrm{bulk}} \left[ S(0) + \int_0^{\infty} g(\Lambda) \left(1 - \alpha(\Lambda)\right) d\Lambda \right]. \tag{6.10}$$

We approximate the cumulative thermal conductivity by a logistic function with logarithmic abscissa

$$\alpha(\Lambda) = \frac{1}{1 + \frac{\Lambda_o}{\Lambda}}. \tag{6.11}$$

Here $\Lambda_o$ is the *characteristic* MFP used to fit the logistic function to the cumulative thermal conductivity, [89] it is the median MFP of the thermal conductivity distribution $\mathrm{K}(\Lambda)$. The suppression function can be derived by adding the resistances due to the diffusive and ballistic transport, [84] which leads to

$$S(\Lambda) = \frac{S(0)}{1 + \frac{\Lambda}{L_c}}. \tag{6.12}$$

The term $S(0)$ in Eq. 6.12 accounts for the reduction in the density of phonon modes due to the pores and the increased resistance due to the path that heat must take around pores. These macroscopic effects are the same for all phonon modes and are equivalent to the

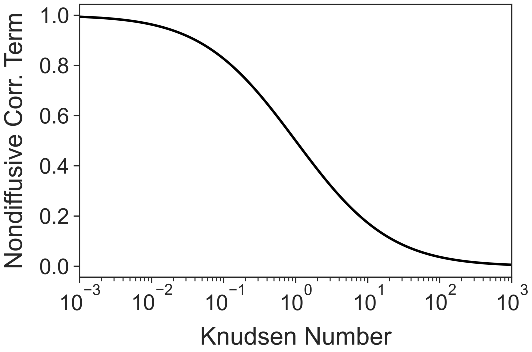

Figure 6.2: Nondiffusive correction term, $\Xi$ vs. Knudsen number. It can be seen that the scale-dependent correction term becomes significant in the ballistic regime where $Kn \gg 1$.

fractional reduction in thermal conductivity predicted by Fourier's law, $S(0) = \kappa_{\text{fourier}}/\kappa_{\text{bulk}}$. Using Eqs. 6.11 and 6.12, Eq. 6.10 becomes

$$\kappa_{\text{eff}}(L_c) = \kappa_{\text{bulk}} S(0)\left[1 - \Lambda_o L_c \int_0^\infty \frac{1}{(\Lambda + \Lambda_o)(\Lambda + L_c)^2} d\Lambda\right], \tag{6.13}$$

which leads to

$$\kappa_{\text{eff}} = \kappa_{\text{fourier}} \Xi(Kn), \tag{6.14}$$

where the *nondiffusive correction term* that accounts for truncation of long MFP phonons by nanoscale pores is given by

$$\Xi(Kn) = \left[\frac{1 + Kn\left(\ln(Kn) - 1\right)}{(Kn - 1)^2}\right], \tag{6.15}$$

with the Knudsen number $Kn = \frac{\Lambda_o}{L_c}$.

Equations 6.14–6.15 are the first main results of our work, and will be referred to as the *BTE-informed* reduced-order model. Interestingly, $\Xi$ depends only on $Kn$. Figure 6.2 shows the nondiffusive correction $\Xi$ versus Knudsen number. For $Kn = 1$, Eq. 6.13 leads to $\kappa_{\text{eff}} = \frac{1}{2}\ \kappa_{\text{fourier}}$. For $Kn \to 0$, $\Xi \to 1$, recovering the diffusive regime. For large

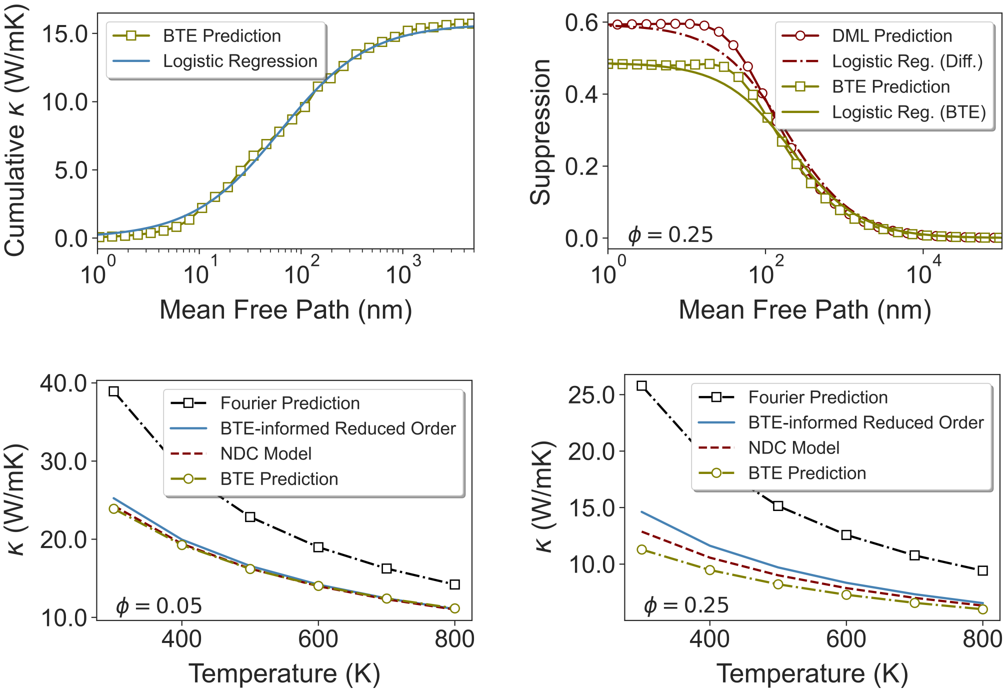

Figure 6.3: (Top-left) The green squares show the cumulative thermal conductivity of bulk GaAs at 800 K computed using BTE, and the solid blue line shows its least-squares logistic regression fit of Eq. 6.11. (Top-right) Plot of the suppression function $S(\Lambda, L_c)$ for same GaAs as in (atop-left) but containing an array of cylindrical pores with porosity $\phi = 25\%$ and pore spacing $L = 100$ nm. The plot in green squares shows the suppression function computed from BTE along with its fit of Eq. 6.12 in solid green. The plot in red circles shows the suppression function obtained from the diffusive material limit model described in "Multiscale Modeling Of Materials" section 6.6, along with its fit of Eq. 6.12 in solid red – see APPENDIX 6.8.2 for mathematical details. Panels (bottom-left) and (bottom-right) plot the thermal conductivity versus temperature for GaAs containing 5% and 25% porosity with a 100 nm pore spacing. The black dot-dashed line with square markers shows the prediction from Fourier's law, and the BTE prediction is plotted with a green dot-dashed line with open circles. The prediction from the reduced-order model, Eq 6.14, using diffusive material suppression is shown in red dash line, and the *BTE-informed* reduced-order model is plotted in solid blue.

$Kn$, i.e. in the ballistic regime, $\Xi(Kn) \approx \ln{(Kn)} Kn^{-1}$.

The cumulative thermal conductivity in bulk GaAs at room temperature from first principles and its least-squares logistic regression's fit from Eq. 6.11 are plotted in figure 6.3(top-left). The logistic curve gives $\Lambda_o = 183$ nm. This is roughly the feature size in GaAs-based porous structures where the phonon-pore scattering takes precedence over the anharmonic scattering. The suppression function and its regression fit from Eq. 6.12 are plotted in figure 6.3(top-right). These figures suggest that equations 6.11 and 6.12 are reasonable approximations to $\alpha(\Lambda)$ and $S(\Lambda)$, respectively. Figures 6.3(bottom-left) and 6.3(bottom-right) illustrate the predictions from the *BTE-informed* reduced-order model applied to the GaAs case for different porosities $\phi$. For $\phi = 0.05$, the model is in agreement with the BTE prediction with less than 5% error, but the higher porosity of $\phi = 0.25$, the model slightly overestimates the thermal conductivity with about 25% error at low temperatures and less than 10% error at high temperatures. The reason for this discrepancy is due to stronger size effects for cases with large porosities, which causes $S(\Lambda)$ to be non-monotonic. [86]

## 6.5 The Diffusive Material Limit

In the previous section, we provide a simple expression for predicting $\kappa_{\text{eff}}$ for different characteristic MFP, $\Lambda_0$ and material's feature size $L_c$. However, while $\Lambda_0$ can be easily obtained from $\alpha(\Lambda)$ and then used for different geometries, obtaining $L_c$ is more convoluted; in fact, as we have shown, it depends on the size of the pores relative to the intrinsic length scale to phonon transport in the bulk material, and as we show later, it also depends on the pore shape. The utility of the reduced order model for $\kappa_{\text{eff}}$ is only achieved if we have a scheme to estimate the value of $L_c$ efficiently, and thus in this section we set out such an approach.

We begin by considering the *diffusive material limit*, described concisely in Appendix 6.8.2 and in details in refs. [175, 86] In this limit, we assume that the suppression function is the same as that from the diffusive regime, $S_{\text{diff}}(\xi)$, where $\xi = \Lambda/L$; this function is scale- and material- independent and is valid only at the macroscales, where all the phonon MFPs are larger than $L_c$. Note that even though in the diffusive regime all phonons travel diffusively, we can still compute the suppression function for arbitrarily MFPs, which, however, will be filtered out. On the other side, in the diffusive material limit, we have $S(\Lambda) = S_{\text{diff}}(\Lambda/L)$, with $L$ being the actual periodicity of the nanomaterial. Under these conditions one finds that the suppression function $S_{\text{diff}}(\Lambda)$ has four key properties: [86] i) its small-MFP limit corresponds to the suppression predicted by Fourier's law, ii) it is material independent, iii) it is scale independent, e.g. it can be translated to consider different dimensions, and vi) it always overestimates the suppression functions computed more accurately from BTE (i.e., $S_{\text{diff}}(\Lambda) > S(\Lambda)$). In practice, in our simulation we obtain $S_{\text{diff}}(\Lambda)$ by making the simulation domain large enough, with periodicity being $L_{\text{large}}$, so that $S(0)$ is the same as $\kappa_{\text{fourier}}/\kappa_{\text{BTE}}$, meaning that there are little ballistic effects on small-MFP phonons. Then, we normalize $\Lambda$ by $L_{\text{large}}$, e.g. $S_{\text{diff}}(\Lambda) \rightarrow S(\xi)$, where $\xi = \Lambda L_{\text{large}}^{-1}$. Once $S(\xi)$ is computed for a given geometry, described in terms of relative distances, we assume that the suppression function of a system described by the same geometry and periodidicity $L$ is simply given by $S(\Lambda) = S_{\text{diff}}(\Lambda/L)$. Essentially, we are neglecting the effect of nondiffusive phonons on small-MFP phonons even at small scales, e.g. where the diffusive material limit is not exactly satisfied. Figure 6.3(top-right) shows $S_{\text{diff}}(\Lambda/L)$ with $L = 50$ nm and porosity $\phi = 0.25$. As expected, it deviates from the BTE around the small-MFP region.

## 6.6 The NonDiffusive Correction Model

In the previous two sections, we have provided an effective medium theory for $\kappa_{\mathrm{eff}}$, encoded by the nondiffusive correction term, and computed the diffusive material limit of the suppression function. In this section, we combine the two concepts: we derive the nondiffusive correction from the diffusive material limit. The resulting method is called the "Nondiffusive Correction Model" (NDC). To do so, similarly to the case with the BTE-informed suppression function, we fit $S_{\mathrm{diff}}$ with a logistic function, as shown in 6.3(top-right). The resulting $L_c$ is 182 nm while that obtained from the BTE-informed model is 214 nm. We note that for the former case, $L_c/L$ is a constant since $S_{\mathrm{diff}}$ is scale-independent. As shown from Figs. 6.3(bottom), the effective thermal conductivities, denoted with $\kappa_{\mathrm{NDC}}$, are in good agreement with those computed directly with the BTE. For the low porosity case, the model is accurately predicts thermal conductivity (less than 1% error) but for the high porosity case, the model slightly overestimates the thermal conductivity (less than 10% error at low temperatures and less than 5% error at high temperatures). The reason for this trend is that small-MFP phonons, i.e. in the region where $S_{\mathrm{diff}}(\Lambda)$ deviates from $S_{\mathrm{diff}}(\Lambda)$ the most, carry little heat with respect the bulk thermal conductivity. However, for high porosities, $L_c$ are smaller thus larger suppression occur throughout the MFP spectrum. Hence, the deviation of $S_{\mathrm{diff}}(\Lambda)$ in the small-MFP region has a larger impact for the case $\phi$ = 0.25.

We *emphasize* that the NDC model is material- and scale- independent, hence once $L_c/L$ and $S(0)$ are identified for a given geometry, they can be used for any material and scale, free from tedious Boltzmann transport simulations. The presented model thus

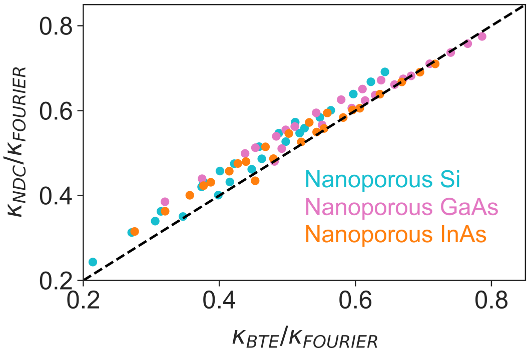

Figure 6.4: Comparison of the thermal conductivity reduction predicted by the reduced order model *vs.* the prediction from the full BTE simulation for a selection of three base materials (Si, GaAs and InAs) at a variety of different temperatures, and containing nanoscale pores with a variety of different porosities and spacings. The periodicity varies from 25–100 nm and the temperature varies from 300–800 K.

provides an upper bound (unless the logistic fit behaves poorly) to $\kappa_{\text{eff}}$ of a nanoporous material knowing the corresponding $\Lambda_o$, $L$ and tabulated values of $S(0)$ and $L_c/L$. To this end, we provide such data for several systems and materials in the Appendix 6.8.1. To summarize, the procedure is as follows:

1. Select a material at a given temperature (from table 6.2). Record the associated $\Lambda_o$ and $\kappa_{\text{bulk}}$.
2. Select a geometry from table 6.1. Record associated $S(0)$ and $L_c/L$.
3. Choose the periodicity of the material, $L$.
4. Compute the Knudsen number as $Kn = \frac{\Lambda_o}{L_c}$
5. Compute the effective thermal conductivity as $\kappa_{\text{eff}} = \kappa_{\text{bulk}} S(0) \Xi(Kn)$

## 6.7 Conclusion

To summarize, we have developed a general model to predict lattice thermal conductivity of dielectrics with nanoscale to macroscale porosity. In this model, the cumulative lattice thermal conductivity is approximated by a logistic function regression with a single tuning parameter single parameter, $\Lambda_o$ the median phonon mean free path. The effect from scattering at pore interfaces is described by the phonon suppression function. This suppression function can be approximated well with another logistic function curve with two fitting parameters of $S(0)$ and $L_c$. The former parameter describes phonon suppression in the diffusive regime and the latter one describes the characteristic scattering distance imposed on the phonons by porosity. These parameters are tabulated in table 6.1 for pores with different shapes and porosities. The model is robust in providing a good approximating of the results from Boltzmann transport simulations of lattice thermal conductivity for a wide range of pores shapes, sizes and spacings that span both the diffusive and ballistic regimes. This provides a simple yet accurate estimation of thermal transport in nanostructures that can be used to rapidly screen or designing materials for a particular thermal task. As such this work provides an important tool to facilitate design and discovery of materials for thermal related applications, without explicitly solving the BTE.

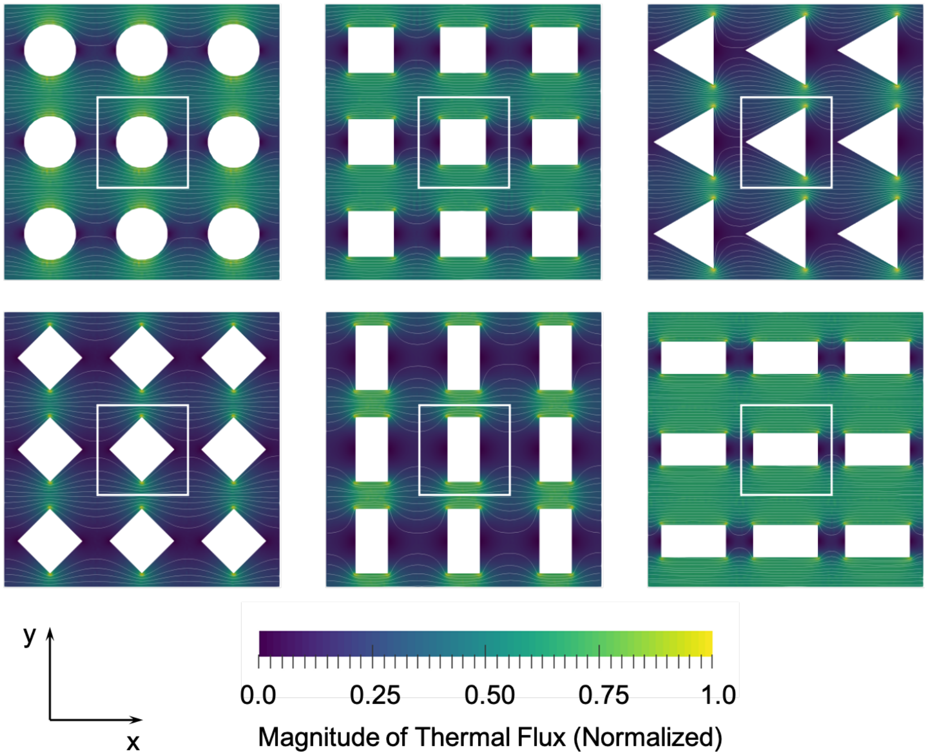

Figure 6.5: Magnitude of the thermal flux in diffusive (material-independent) structure containing aligned pores with different shapes. The porosity is fixed to 0.25 and periodicity is L = 50 nm. The unit cells is highlighted.

## 6.8 Appendix

### 6.8.1 Tabulated Data for the NDC

Table 6.1 shows the phonon characteristic length, $L_c$ and diffusive suppression function, $S(0)$ for pores with different shapes and porosities. The shape of the pores are shown in Fig. 6.5. In all cases temperature gradient is along abscissa. Tables 6.2 and 6.3 show the characteristic MFP and bulk thermal conductivity of wide sweep of IV and III-V dielectrics at different temperatures.

Table 6.1: The diffusive model prediction for phonon characteristic length and diffusive suppression in pores with different shapes and porosity. In all cases temperature gradient is along abscissa.

| Porosity | Circle pore | | Square pore | | Triangle pore | | Rectangle pore | | Rhombus pore | |
|---|---|---|---|---|---|---|---|---|---|---|
| | $L_c/L$ | S(0) | $L_c/L$ | S(0) | $L_c/L$ | S(0) | $L_c/L$ | S(0) | $L_c/L$ | S(0) |
| 0.05 | 3.92 | 0.90 | 3.22 | 0.90 | 2.74 | 0.90 | 3.26 | 0.92 | 3.48 | 0.90 |
| 0.10 | 2.64 | 0.83 | 2.38 | 0.80 | 2.04 | 0.77 | 2.34 | 0.84 | 2.54 | 0.80 |
| 0.15 | 2.24 | 0.74 | 1.86 | 0.73 | 1.56 | 0.69 | 1.80 | 0.80 | 2.22 | 0.70 |
| 0.20 | 2.02 | 0.66 | 1.54 | 0.66 | 1.66 | 0.54 | 1.62 | 0.72 | 1.74 | 0.64 |
| 0.25 | 1.82 | 0.59 | 1.58 | 0.56 | 1.14 | 0.51 | 1.48 | 0.67 | 1.60 | 0.56 |
| 0.30 | 1.54 | 0.54 | 1.36 | 0.51 | 1.04 | 0.42 | 1.34 | 0.63 | 1.36 | 0.49 |
| 0.35 | 1.46 | 0.48 | 1.18 | 0.46 | 0.90 | 0.33 | 1.16 | 0.59 | 1.22 | 0.42 |
| 0.40 | 1.40 | 0.42 | 1.08 | 0.41 | 0.76 | 0.24 | 0.98 | 0.57 | 1.04 | 0.36 |
| 0.45 | 1.26 | 0.37 | 1.02 | 0.36 | – | – | 0.84 | 0.54 | 1.00 | 0.26 |
| 0.50 | 1.18 | 0.32 | 0.94 | 0.31 | – | – | 0.78 | 0.50 | – | – |

Table 6.2: The characteristic MFP of IV and III-V dielectrics.

| Temperature(K) | Characteristic Mean Free Path ($\mu m$) | | | | | | | | | |
|---|---|---|---|---|---|---|---|---|---|---|
| | AlAs | AlN | GaAs | GaN | GaP | Ge | InAs | InP | Si | Sn |
| 200 | 0.41 | 0.43 | 0.31 | 0.46 | 0.35 | 0.53 | 0.47 | 1.35 | 1.33 | 0.26 |
| 300 | 0.24 | 0.16 | 0.18 | 0.25 | 0.21 | 0.30 | 0.29 | 0.80 | 0.49 | 0.18 |
| 400 | 0.17 | 0.10 | 0.13 | 0.18 | 0.16 | 0.21 | 0.21 | 0.58 | 0.29 | 0.13 |
| 500 | 0.13 | 0.07 | 0.10 | 0.15 | 0.13 | 0.16 | 0.17 | 0.45 | 0.21 | 0.11 |
| 600 | 0.11 | 0.05 | 0.08 | 0.13 | 0.10 | 0.13 | 0.14 | 0.37 | 0.17 | 0.09 |
| 700 | 0.09 | 0.04 | 0.07 | 0.11 | 0.09 | 0.11 | 0.12 | 0.32 | 0.14 | 0.08 |
| 800 | 0.08 | 0.04 | 0.06 | 0.10 | 0.08 | 0.10 | 0.10 | 0.28 | 0.12 | 0.07 |

### 6.8.2 The Diffusive Material Limit

Here we briefly describe the diffusive material limit, introduced in [86]. With no loss of generality, let us assume we have an isotropic MFP distribution, then the BTE reads

$$\Lambda \mathbf{s} \cdot \nabla T(\Lambda, \Omega) + T(\Lambda, \Omega) = \int \alpha(\Lambda') \langle T(\Lambda') \rangle d\Lambda', \tag{6.16}$$

Table 6.3: The bulk thermal conductivity of IV and III-V dielectrics.

| Temperature(K) | Bulk Thermal Conductivity (W/mK) | | | | | | | | | |
|---|---|---|---|---|---|---|---|---|---|---|
| | AlAs | AlN | GaAs | GaN | GaP | Ge | InAs | InP | Si | Sn |
| 200 | 127 | 594 | 71 | 359 | 122 | 90 | 44 | 126 | 287 | 28 |
| 300 | 81 | 302 | 45 | 250 | 82 | 60 | 28 | 81 | 165 | 19 |
| 400 | 60 | 203 | 34 | 197 | 62 | 45 | 21 | 60 | 118 | 14 |
| 500 | 48 | 155 | 27 | 165 | 50 | 37 | 17 | 48 | 93 | 12 |
| 600 | 40 | 126 | 22 | 142 | 42 | 31 | 14 | 40 | 76 | 10 |
| 700 | 34 | 106 | 19 | 126 | 36 | 27 | 12 | 34 | 65 | 8 |
| 800 | 30 | 92 | 17 | 113 | 32 | 24 | 10 | 30 | 57 | 7 |

where $\langle f \rangle$ is an average over the solid angle and $\int \alpha(\Lambda')d\Lambda' = 1$. The suppression function is given by [87]

$$S(\Lambda) = 3\langle \mathbf{s} \otimes \mathbf{s} \nabla \tilde{T}(\Lambda, \Omega) \cdot \hat{\mathbf{n}} \rangle, \tag{6.17}$$

where $\tilde{f} = -LA^{-1}\Delta T \int_A f dS$. Let us now focus on the small-MFP limit of $S$. Combining Eq. 6.16-6.17, we have

$$S(0) = \int \alpha(\Lambda')\nabla\langle\tilde{T}(\Lambda')\rangle \cdot \hat{\mathbf{n}} d\Lambda', \tag{6.18}$$

where we used $\langle \mathbf{s} \otimes \mathbf{s} \rangle = 1/3$. For nanoscale materials $\langle\nabla\tilde{T}(\Lambda')\rangle \cdot \hat{\mathbf{n}} < \nabla\tilde{T}_F \cdot \hat{\mathbf{n}}$, [86] where $T_F$ is computed from Fourier's law; thus $S(0) < \kappa_{\text{fourier}}/\kappa_{\text{bulk}}$. For this reason, BTE simulations on materials where size effects are significant show that $S(0)$ is material dependent and is always smaller than the Fourier's limit. On the other hand, in macroscopic systems the phonon distributions are isotropic and $\langle\tilde{T}(\Lambda')\rangle \approx \tilde{T}_F$ for the entire range of the bulk MFP distribution, thus $S(0) = \nabla\tilde{T}_f \cdot \hat{\mathbf{n}} = \kappa_{\text{fourier}}/\kappa_{\text{bulk}}$, which is exactly the macroscopic suppression. In this regime, the effective thermal conductivity is $\kappa_{\text{eff}} = \int \mathcal{K}(\Lambda)S(\Lambda)d\Lambda \approx S(0)\kappa_{\text{bulk}} = \kappa_{\text{fourier}}$. Similarly, the pseudo lattice temperature, i.e. the RHS of Eq. 6.16, can be approximated by $\int \alpha(\Lambda')\langle T(\Lambda)\rangle d\Lambda \approx \langle T(0)\rangle = T_F$. Note that as $\alpha(\Lambda)$ disappeared from the definition of the pseudotemperature, Eq. 6.16 is now material- and scale- independent, i.e.

$$\xi \mathbf{s} \cdot \nabla T(\xi, \Omega) + T(\xi, \Omega) = \langle T(0)\rangle, \tag{6.19}$$

where $\xi = \Lambda/L$. In this regime, the suppression function is $S_{\text{diff}}(\xi)$. We stress that Eq. 6.19 is valid only when all the bulk MFP are well below $L_c$. The diffusive material limit, then, amounts to using Eq. 6.19 in cases where such a condition is not necessarily satisfied, i.e. $S(\lambda) = S_{\text{diff}}(\Lambda/L)$. In practice, this limit can be obtained, as we did in our work, by making the material sufficiently large so that Eq. 6.19 holds, and solve it for a wide MFP range so that the logistic-shape of the suppression function is recovered. Then by using the scale-independence of Eq. 6.19, we scale the domain of the suppression function to adapt it to cases with smaller $L$. Note that even though the solution of the BTE for MFPs that are beyond the bulk distribution is not relevant, we can still solve Eq. 6.19 for arbitrarily $\Lambda$ and compute the relative suppression function; then, the portion of the spectrum not belonging to the support of $\mathcal{K}(\Lambda)$ will be filtered by Eq. 6.3. We note that since in this case $S(0) = \kappa_{\text{fourier}}/\kappa_{\text{bulk}}$, the suppression function of the diffusive material limit is an upper bound to the actual one. [175] Lastly, the name of “diffusive material” arises from the need to differentiate this regime from the mere diffusive limit, which is solved using Fourier’s law, while also emphasizing that the solution of Eq. 6.19 should be carried out over the whole range of bulk MFPs.

# Bibliography

[1] Lawrence Livermore National Laboratory. U.s. energy use rises to highest level ever.

[2] Jihui Yang. Potential applications of thermoelectric waste heat recovery in the automotive industry. In *ICT 2005. 24th International Conference on Thermoelectrics, 2005.*, pages 170–174. IEEE, 2005.

[3] Cronin B Vining. A model for the high-temperature transport properties of heavily doped n-type silicon-germanium alloys. *Journal of Applied Physics*, 69(1):331–341, 1991.

[4] Adem Atmaca and Mehmet Kanoglu. Reducing energy consumption of a raw mill in cement industry. *Energy*, 42(1):261–269, 2012.

[5] Rahman Saidur, Mahdi Rezaei, Wan Khairul Muzammil, MH Hassan, Saman Paria, and Md Hasanuzzaman. Technologies to recover exhaust heat from internal combustion engines. *Renewable and sustainable energy reviews*, 16(8):5649–5659, 2012.

[6] George Nolas, Lilia M Woods, and Ryoji Funahashi. Advanced thermoelectrics, 2020.

[7] Joni Welman Simatupang and Irwan Purnama. Study on various simple power tracking methods for thermoelectric generator. In *2019 International Conference on Sustainable Energy Engineering and Application (ICSEEA)*, pages 79–84. IEEE, 2019.

[8] Kris Anderson and Nigel Brandon. Techno-economic analysis of thermoelectrics for waste heat recovery. *Energy Sources, Part B: Economics, Planning, and Policy*, 14(4):147–157, 2019.

[9] Yuping He, François Léonard, Douglas L Medlin, Nicholas Baldasaro, Dorota S Temple, Philip Barletta, and Catalin D Spataru. High-efficiency thin-film superlattice thermoelectric cooler modules enabled by low resistivity contacts. *Advanced Electronic Materials*, 4(3):1700381, 2018.

[10] Xudong Zhu, Lili Cao, Wei Zhu, and Yuan Deng. Enhanced interfacial adhesion and thermal stability in bismuth telluride/nickel/copper multilayer films with low electrical contact resistance. *Advanced Materials Interfaces*, 5(23):1801279, 2018.

[11] Weishu Liu and Shengqiang Bai. Thermoelectric interface materials: A perspective to the challenge of thermoelectric power generation module. *Journal of Materiomics*, 5(3):321–336, 2019.

[12] Yi Ma, Richard Heijl, and Anders EC Palmqvist. Composite thermoelectric materials with embedded nanoparticles. *Journal of Materials Science*, 48(7):2767–2778, 2013.

[13] Sabah K Bux, Richard G Blair, Pawan K Gogna, Hohyun Lee, Gang Chen, Mildred S Dresselhaus, Richard B Kaner, and Jean-Pierre Fleurial. Nanostructured bulk silicon as an effective thermoelectric material. *Advanced Functional Materials*, 19(15):2445–2452, 2009.

[14] HR Shanks, PD Maycock, PH Sidles, and GC Danielson. Thermal conductivity of silicon from 300 to 1400 k. *Physical Review*, 130(5):1743, 1963.

[15] D Coleman, T Lopez, S Exarhos, M Mecklenburg, S Bux, and L Mangolini. Thermoelectric performance of silicon with oxide nanoinclusions. *Materials Research Letters*, 6(8):419–425, 2018.

[16] Gang Chen. *Nanoscale energy transport and conversion: a parallel treatment of electrons, molecules, phonons, and photons*. Oxford university press, 2005.

[17] Mark S Lundstrom and Changwook Jeong. *Near-Equilibrium Transport: Fundamentals and Applications*, volume 2. World Scientific Publishing Company, 2012.

[18] Y Pei, AD LaLonde, H Wang, and G Jeffrey Snyder. Energy environ. sci. 5, 7963 (2012).

[19] Georg Kresse and Jürgen Hafner. Ab initio molecular dynamics for liquid metals. *Physical Review B*, 47(1):558, 1993.

[20] G. Kresse and J. Furthmüller. Efficient iterative schemes for ab initio total-energy calculations using a plane-wave basis set. *Phys. Rev. B*, 54:11169–11186, Oct 1996.

[21] G. Kresse and J. Hafner. Ab initio molecular-dynamics simulation of the liquid-metal–amorphous-semiconductor transition in germanium. *Phys. Rev. B*, 49:14251–14269, May 1994.

[22] G Kresse and J Hafner. Phys. re v. b 1993, 47, 558.(b) kresse, g.; furthmüller. *Comput. Mater. Sci*, 6:15, 1996.

[23] John P Perdew, Kieron Burke, and Matthias Ernzerhof. Generalized gradient approximation made simple. *Physical review letters*, 77(18):3865, 1996.

[24] Peter E Blöchl. Projector augmented-wave method. *Physical review B*, 50(24):17953, 1994.

[25] Georg Kresse and Daniel Joubert. From ultrasoft pseudopotentials to the projector augmented-wave method. *Physical review b*, 59(3):1758, 1999.

[26] Hendrik J Monkhorst and James D Pack. Special points for brillouin-zone integrations. *Physical review B*, 13(12):5188, 1976.

[27] WB Joyce and RW Dixon. Analytic approximations for the fermi energy of an ideal fermi gas. *Applied Physics Letters*, 31(5):354–356, 1977.

[28] Michael E Levinshtein, Sergey L Rumyantsev, and Michael S Shur. *Properties of Advanced Semiconductor Materials: GaN, AIN, InN, BN, SiC, SiGe*. John Wiley & Sons, 2001.

[29] Mark Lundstrom. *Fundamentals of carrier transport*. Cambridge university press, 2009.

[30] M Mondal and KP Gnatak. Effect of carrier degeneracy on the screening length in degenerate tetragonal semiconductors. *physica status solidi (b)*, 135(1):239–251, 1986.

[31] D Mark Riffe. Temperature dependence of silicon carrier effective masses with application to femtosecond reflectivity measurements. *JOSA B*, 19(5):1092–1100, 2002.

[32] M. V. Fischetti. Monte carlo simulation of transport in technologically significant semiconductors of the diamond and zinc-blende structures. i. homogeneous transport. *IEEE Transactions on Electron Devices*, 38(3):634–649, 1991.

[33] Yu I Ravich, BA Efimova, and VI Tamarchenko. Scattering of current carriers and transport phenomena in lead chalcogenides. *physica status solidi (b)*, 43(1):11–33, 1971.

[34] Hohyun Lee, Daryoosh Vashaee, DZ Wang, Mildred S Dresselhaus, ZF Ren, and Gang Chen. Effects of nanoscale porosity on thermoelectric properties of sige. *Journal of Applied Physics*, 107(9):094308, 2010.

[35] Biswaranjan R Nag. *Electron transport in compound semiconductors*, volume 11. Springer Science & Business Media, 2012.

[36] S. Aria Hosseini, Giuseppe Romano, and P. Alex Greaney. Mitigating the effect of nanoscale porosity on thermoelectric power factor of si, 2020.

[37] J Martin, Li Wang, Lidong Chen, and GS Nolas. Enhanced seebeck coefficient through energy-barrier scattering in pbte nanocomposites. *Physical review B*, 79(11):115311, 2009.

[38] A. J. Minnich, H. Lee, X. W. Wang, G. Joshi, M. S. Dresselhaus, Z. F. Ren, G. Chen, and D. Vashaee. Modeling study of thermoelectric sige nanocomposites. *Phys. Rev. B*, 80:155327, Oct 2009.

[39] AJ Minnich, H Lee, XW Wang, G Joshi, MS Dresselhaus, ZF Ren, G Chen, and D Vashaee. Modeling study of thermoelectric sige nanocomposites. *Physical Review B*, 80(15):155327, 2009.

[40] M Cruz, C Wang, MR Beltrán, and J Tagüeña-Martínez. Morphological effects on the electronic band structure of porous silicon. *Physical Review B*, 53(7):3827, 1996.

[41] Guangsha Shi and Emmanouil Kioupakis. Electronic and optical properties of nanoporous silicon for solar-cell applications. *Acs Photonics*, 2(2):208–215, 2015.

[42] Wu Li, Lucas Lindsay, David A Broido, Derek A Stewart, and Natalio Mingo. Thermal conductivity of bulk and nanowire mg 2 si x sn 1- x alloys from first principles. *Physical Review B*, 86(17):174307, 2012.

[43] Ramez Cheaito, John C Duda, Thomas E Beechem, Khalid Hattar, Jon F Ihlefeld, Douglas L Medlin, Mark A Rodriguez, Michael J Campion, Edward S Piekos, and Patrick E Hopkins. Experimental investigation of size effects on the thermal conductivity of silicon-germanium alloy thin films. *Physical review letters*, 109(19):195901, 2012.

[44] Jeffrey L Braun, Christopher H Baker, Ashutosh Giri, Mirza Elahi, Kateryna Artyushkova, Thomas E Beechem, Pamela M Norris, Zayd C Leseman, John T Gaskins, and Patrick E Hopkins. Size effects on the thermal conductivity of amorphous silicon thin films. *Physical Review B*, 93(14):140201, 2016.

[45] Tianli Feng and Xiulin Ruan. Ultra-low thermal conductivity in graphene nanomesh. *Carbon*, 101:107–113, 2016.

[46] Jaime Andres Perez-Taborda, Miguel Muñoz Rojo, Jon Maiz, Neophytos Neophytou, and Marisol Martin-Gonzalez. Ultra-low thermal conductivities in large-area si-ge nanomeshes for thermoelectric applications. *Scientific reports*, 6(1):1–10, 2016.

[47] Ming Hu and Dimos Poulikakos. Si/ge superlattice nanowires with ultralow thermal conductivity. *Nano letters*, 12(11):5487–5494, 2012.

[48] Xin Mu, Lili Wang, Xueming Yang, Pu Zhang, Albert C To, and Tengfei Luo. Ultra-low thermal conductivity in si/ge hierarchical superlattice nanowire. *Scientific reports*, 5(1):1–11, 2015.

[49] Jivtesh Garg and Gang Chen. Minimum thermal conductivity in superlattices: A first-principles formalism. *Physical Review B*, 87(14):140302, 2013.

[50] Xiaolei Shi, Angyin Wu, Weidi Liu, Raza Moshwan, Yuan Wang, Zhi-Gang Chen, and Jin Zou. Polycrystalline snse with extraordinary thermoelectric property via nanoporous design. *ACS nano*, 12(11):11417–11425, 2018.

[51] Laura de Sousa Oliveira and Neophytos Neophytou. Large-scale molecular dynamics investigation of geometrical features in nanoporous si. *Phys. Rev. B*, 100:035409, Jul 2019.

[52] Laura de Sousa Oliveira, S. Aria Hosseini, Alex Greaney, and Neophytos Neophytou. Heat current anticorrelation effects leading to thermal conductivity reduction in nanoporous si. *Phys. Rev. B*, 102:205405, Nov 2020.

[53] Raúl José Martín-Palma, Fernando Agulló-Rueda, and José Martínez-Duart. *Nanotechnology for microelectronics and optoelectronics.* Elsevier, 2006.

[54] Loreto Mateu and Francesc Moll. Review of energy harvesting techniques and applications for microelectronics. In *VLSI Circuits and Systems II*, volume 5837, pages 359–373. International Society for Optics and Photonics, 2005.

[55] Marius Grundmann. *Nano-optoelectronics: concepts, physics and devices.* Springer Science & Business Media, 2002.

[56] Isha Bharti, Nishu Gupta, and KM Gupta. Novel applications of functionally graded nano, optoelectronic and thermoelectric materials. *International Journal of Materials, Mechanics and Manufacturing*, 1(3):221–224, 2013.

[57] Ali Shakouri and Mona Zebarjadi. Nanoengineered materials for thermoelectric energy conversion. *Thermal Nanosystems and Nanomaterials*, pages 225–299, 2009.

[58] Ali Shakouri. Recent developments in semiconductor thermoelectric physics and materials. *Annual review of materials research*, 41:399–431, 2011.

[59] G Jeffrey Snyder and Eric S Toberer. Complex thermoelectric materials. *Materials for sustainable energy: a collection of peer-reviewed research and review articles from Nature Publishing Group*, pages 101–110, 2011.

[60] AJl Minnich, Milfred S Dresselhaus, ZF Ren, and G Chen. Bulk nanostructured thermoelectric materials: current research and future prospects. *Energy & Environmental Science*, 2(5):466–479, 2009.

[61] Chhatrasal Gayner and Yaron Amouyal. Energy filtering of charge carriers: current trends, challenges, and prospects for thermoelectric materials. *Advanced Functional Materials*, 30(18):1901789, 2020.

[62] Daniel F Hanks, Zhengmao Lu, Jay Sircar, Todd R Salamon, Dion S Antao, Kevin R Bagnall, Banafsheh Barabadi, and Evelyn N Wang. Nanoporous membrane device for ultra high heat flux thermal management. *Microsystems & nanoengineering*, 4(1):1–10, 2018.

[63] H Jeremy Cho, Daniel J Preston, Yangying Zhu, and Evelyn N Wang. Nanoengineered materials for liquid–vapour phase-change heat transfer. *Nature Reviews Materials*, 2(2):1–17, 2016.

[64] Zhiping Xu and Markus J Buehler. Nanoengineering heat transfer performance at carbon nanotube interfaces. *ACS nano*, 3(9):2767–2775, 2009.

[65] Asuka Miura, Shu Zhou, Tomohiro Nozaki, and Junichiro Shiomi. Crystalline–amorphous silicon nanocomposites with reduced thermal conductivity for bulk thermoelectrics. *ACS applied materials & interfaces*, 7(24):13484–13489, 2015.

[66] Bolin Liao and Gang Chen. Nanocomposites for thermoelectrics and thermal engineering. *MRS Bulletin*, 40(9):746–752, 2015.

[67] Ranita Basu, Shovit Bhattacharya, Ranu Bhatt, Mainak Roy, Sajid Ahmad, Ajay Singh, M Navaneethan, Y Hayakawa, DK Aswal, and SK Gupta. Improved thermoelectric performance of hot pressed nanostructured n-type sige bulk alloys. *Journal of Materials Chemistry A*, 2(19):6922–6930, 2014.

[68] Jinyao Tang, Hung-Ta Wang, Dong Hyun Lee, Melissa Fardy, Ziyang Huo, Thomas P Russell, and Peidong Yang. Holey silicon as an efficient thermoelectric material. *Nano letters*, 10(10):4279–4283, 2010.

[69] Jongwoo Lim, Hung-Ta Wang, Jinyao Tang, Sean C Andrews, Hongyun So, Jaeho Lee, Dong Hyun Lee, Thomas P Russell, and Peidong Yang. Simultaneous thermoelectric property measurement and incoherent phonon transport in holey silicon. *ACS nano*, 10(1):124–132, 2016.

[70] Giuseppe Romano and Jeffrey C. Grossman. Toward phonon-boundary engineering in nanoporous materials. *Applied Physics Letters*, 105(3):033116, 2014.

[71] Hatim Machrafi and Georgy Lebon. Size and porosity effects on thermal conductivity of nanoporous material with an extension to nanoporous particles embedded in a host matrix. *Physics Letters A*, 379(12-13):968–973, 2015.

[72] Joo-Hyoung Lee and Jeffrey C Grossman. Thermoelectric properties of nanoporous ge. *Applied Physics Letters*, 95(1):013106, 2009.

[73] Joo-Hyoung Lee, Giulia A Galli, and Jeffrey C Grossman. Nanoporous si as an efficient thermoelectric material. *Nano letters*, 8(11):3750–3754, 2008.

[74] Tse-Yang Hsieh, Herng Lin, Tsang-Jen Hsieh, and Juan-Chen Huang. Thermal conductivity modeling of periodic porous silicon with aligned cylindrical pores. *Journal of Applied Physics*, 111(12):124329, 2012.

[75] Rolf Landauer. The electrical resistance of binary metallic mixtures. *Journal of Applied Physics*, 23(7):779–784, 1952.

[76] Carl Johan Friedrich Böttcher and Paul Bordewijk. *Theory of electric polarization*, volume 2. Elsevier Science Limited, 1978.

[77] DPH Hasselman and Lloyd F Johnson. Effective thermal conductivity of composites with interfacial thermal barrier resistance. *Journal of composite materials*, 21(6):508–515, 1987.

[78] James Clerk Maxwell. *A treatise on electricity and magnetism*, volume 1. Oxford: Clarendon Press, 1873.

[79] Arnold Eucken. W armeleitf ahigkeit keramischer feuerfester stoffe-berechnung aus der w armeleitf ahigkeit der bestandteile. *Forschung auf dem Gebiet des Ingenieurwesens*, 3:16, 1932.

[80] Lord Rayleigh. Lvi. on the influence of obstacles arranged in rectangular order upon the properties of a medium. *The London, Edinburgh, and Dublin Philosophical Magazine and Journal of Science*, 34(211):481–502, 1892.

[81] Y Benveniste. Effective thermal conductivity of composites with a thermal contact resistance between the constituents: Nondilute case. *Journal of applied physics*, 61(8):2840–2843, 1987.

[82] Ce-Wen Nan, R Birringer, David R Clarke, and H Gleiter. Effective thermal conductivity of particulate composites with interfacial thermal resistance. *Journal of Applied Physics*, 81(10):6692–6699, 1997.

[83] Austin Minnich and Gang Chen. Modified effective medium formulation for the thermal conductivity of nanocomposites. *Applied Physics Letters*, 91(7):073105, 2007.

[84] Ravi Prasher. Transverse thermal conductivity of porous materials made from aligned nano-and microcylindrical pores. *Journal of Applied Physics*, 100(6):064302, 2006.

[85] Liang-Chun Liu and Mei-Jiau Huang. Thermal conductivity modeling of micro-and nanoporous silicon. *International journal of thermal sciences*, 49(9):1547–1554, 2010.

[86] Giuseppe Romano and Alexie M Kolpak. Diffusive phonons in nongray nanostructures. *Journal of Heat Transfer*, 141(1), 2019.

[87] Giuseppe Romano and Alexie M Kolpak. Directional phonon suppression function as a tool for the identification of ultralow thermal conductivity materials. *Scientific reports*, 7(1):1–8, 2017.

[88] SJ Poon and K Limtragool. Nanostructure model of thermal conductivity for high thermoelectric performance. *Journal of Applied Physics*, 110(11):114306, 2011.

[89] Wu Li, Jesús Carrete, Nebil A Katcho, and Natalio Mingo. Shengbte: A solver of the boltzmann transport equation for phonons. *Computer Physics Communications*, 185(6):1747–1758, 2014.

[90] Lunlun Gong, Yonghong Wang, Xudong Cheng, Ruifang Zhang, and Heping Zhang. A novel effective medium theory for modelling the thermal conductivity of porous materials. *International Journal of Heat and Mass Transfer*, 68:295–298, 2014.

[91] Jianfeng Wang, James K Carson, Mike F North, and Donald J Cleland. A new approach to modelling the effective thermal conductivity of heterogeneous materials. *International journal of heat and mass transfer*, 49(17-18):3075–3083, 2006.

[92] RH Tarkhanyan and DG Niarchos. Reduction in lattice thermal conductivity of porous materials due to inhomogeneous porosity. *International journal of thermal sciences*, 67:107–112, 2013.

[93] Karol Pietrak and Tomasz S Wiśniewski. A review of models for effective thermal conductivity of composite materials. *Journal of Power Technologies*, 95(1):14–24, 2014.

[94] Giuseppe Romano and Jeffrey C Grossman. Toward phonon-boundary engineering in nanoporous materials. *Applied Physics Letters*, 105(3):033116, 2014.

[95] S. Aria Hosseini, Devin Coleman, Sabah K. Bux, Lorenzo Mangolini, and P. Alex Greaney. Enhanced power factor via electron energy filtering by nanoinclusions. *Manuscr. Submitt. Publ. 2020*, 2021.

[96] Georg Kresse and Jürgen Hafner. Ab initio molecular-dynamics simulation of the liquid-metal–amorphous-semiconductor transition in germanium. *Physical Review B*, 49(20):14251, 1994.

[97] Georg Kresse and Jürgen Furthmüller. Efficiency of ab-initio total energy calculations for metals and semiconductors using a plane-wave basis set. *Computational materials science*, 6(1):15–50, 1996.

[98] Georg Kresse and Jürgen Furthmüller. Efficient iterative schemes for ab initio total-energy calculations using a plane-wave basis set. *Physical review B*, 54(16):11169, 1996.

[99] S. Aria Hosseini. Thermoelectric.py. `https://github.com/ariahosseini/thermoelectric.py`, 2019.

[100] SM Sze and KK Ng. pn junctions. In *Physics of Semiconductor Devices*, volume 2, pages 80–89. Wiley New York, 2006.

[101] Jackson R Harter, S Aria Hosseini, Todd S Palmer, and P Alex Greaney. Prediction of thermal conductivity in dielectrics using fast, spectrally-resolved phonon transport simulations. *International Journal of Heat and Mass Transfer*, 144:118595, 2019.

[102] LC Burton. Temperature dependence of the silicon work function by means of a retarding potential technique. *Journal of Applied Physics*, 47(3):1189–1191, 1976.

[103] Laura de Sousa Oliveira and Neophytos Neophytou. Large-scale molecular dynamics investigation of geometrical features in nanoporous si. *Physical Review B*, 100(3):035409, 2019.

[104] Laura de Sousa Oliveira, S Aria Hosseini, Alex Greaney, and Neophytos Neophytou. Heat current anticorrelation effects leading to thermal conductivity reduction in nanoporous si. *Physical Review B*, 102(20):205405, 2020.

[105] Hyun-Sik Kim, Zachary M Gibbs, Yinglu Tang, Heng Wang, and G Jeffrey Snyder. Characterization of lorenz number with seebeck coefficient measurement. *APL materials*, 3(4):041506, 2015.

[106] George S Nolas, Jeffrey Sharp, and Julian Goldsmid. *Thermoelectrics: basic principles and new materials developments*, volume 45. Springer Science & Business Media, 2013.

[107] Saffa B Riffat and Xiaoli Ma. Thermoelectrics: a review of present and potential applications. *Applied thermal engineering*, 23(8):913–935, 2003.

[108] Christopher J Vineis, Ali Shakouri, Arun Majumdar, and Mercouri G Kanatzidis. Nanostructured thermoelectrics: big efficiency gains from small features. *Advanced materials*, 22(36):3970–3980, 2010.

[109] Giuseppe Romano and Jeffrey C Grossman. Phonon bottleneck identification in disordered nanoporous materials. *Physical Review B*, 96(11):115425, 2017.

[110] Avinash Vishwakarma, Sivaiah Bathula, Nagendra S Chauhan, Ruchi Bhardwaj, Bhasker Gahtori, Avanish K Srivastava, and Ajay Dhar. Facile synthesis of nanostructured n-type sige alloys with enhanced thermoelectric performance using rapid solidification employing melt spinning followed by spark plasma sintering. *Current Applied Physics*, 18(12):1540–1545, 2018.

[111] Sivaiah Bathula, M Jayasimhadri, Nidhi Singh, AK Srivastava, Jiji Pulikkotil, Ajay Dhar, and RC Budhani. Enhanced thermoelectric figure-of-merit in spark plasma sintered nanostructured n-type sige alloys. *Applied Physics Letters*, 101(21):213902, 2012.

[112] Yanzhong Pei, Aaron LaLonde, Shiho Iwanaga, and G Jeffrey Snyder. High thermoelectric figure of merit in heavy hole dominated pbte. *Energy & Environmental Science*, 4(6):2085–2089, 2011.

[113] Y Gelbstein, Z Dashevsky, and MP Dariel. High performance n-type pbte-based materials for thermoelectric applications. *Physica B: Condensed Matter*, 363(1-4):196–205, 2005.

[114] Ananya Banik and Kanishka Biswas. A game-changing strategy in snse thermoelectrics. *Joule*, 3(3):636–638, 2019.

[115] Jungdae Kim, Sunglae Cho, et al. A review of snse: growth and thermoelectric properties. *Journal of the Korean Physical Society*, 72(8):841–857, 2018.

[116] Giuseppe Romano. Openbte: A multiscale solver for the phonon boltzmann transport equation. In *APS Meeting Abstracts*, 2019.

[117] Jesús Carrete, Bjorn Vermeersch, Ankita Katre, Ambroise van Roekeghem, Tao Wang, Georg KH Madsen, and Natalio Mingo. almabte: A solver of the space–time dependent boltzmann transport equation for phonons in structured materials. *Computer Physics Communications*, 220:351–362, 2017.

[118] Marco Arrigoni, Jesús Carrete, Natalio Mingo, and Georg KH Madsen. First-principles quantitative prediction of the lattice thermal conductivity in random semiconductor alloys: The role of force-constant disorder. *Physical Review B*, 98(11):115205, 2018.

[119] Shin-ichiro Tamura. Isotope scattering of dispersive phonons in ge. *Physical Review B*, 27(2):858, 1983.

[120] Takuma Hori, Junichiro Shiomi, and Chris Dames. Effective phonon mean free path in polycrystalline nanostructures. *Applied Physics Letters*, 106(17):171901, 2015.

[121] Chengyun Hua and Austin J Minnich. Importance of frequency-dependent grain boundary scattering in nanocrystalline silicon and silicon–germanium thermoelectrics. *Semiconductor Science and Technology*, 29(12):124004, 2014.

[122] Lina Yang and Austin J Minnich. Thermal transport in nanocrystalline si and sige by ab initio based monte carlo simulation. *Scientific reports*, 7(1):1–11, 2017.

[123] Giuseppe Romano, Keivan Esfarjani, David A Strubbe, David Broido, and Alexie M Kolpak. Temperature-dependent thermal conductivity in silicon nanostructured materials studied by the boltzmann transport equation. *Physical Review B*, 93(3):035408, 2016.

[124] N Savvides and DM Rowe. Precipitation of phosphorus from solid solutions in si-ge alloys and its effect on thermoelectric transport properties. *Journal of Physics D: Applied Physics*, 14(4):723, 1981.

[125] G Kresse, J Furthmüller, and J Hafner. Theory of the crystal structures of selenium and tellurium: the effect of generalized-gradient corrections to the local-density approximation. *Physical Review B*, 50(18):13181, 1994.

[126] Jasprit Singh. *Physics of Semiconductors and their Heterostructures.* McGraw-Hill College, 1993.

[127] Yuan Taur and Tak H Ning. *Fundamentals of modern VLSI devices.* Cambridge university press, 2013.

[128] Jens S Christensen. *Dopant diffusion in Si and SiGe.* PhD thesis, Mikroelektronik och informationsteknik, 2004.

[129] Eric Pop. Energy dissipation and transport in nanoscale devices. *Nano Research*, 3(3):147–169, 2010.

[130] G Berruto, I Madan, Y Murooka, GM Vanacore, E Pomarico, J Rajeswari, R Lamb, P Huang, AJ Kruchkov, Y Togawa, et al. Laser-induced skyrmion writing and erasing in an ultrafast cryo-lorentz transmission electron microscope. *Physical review letters*, 120(11):117201, 2018.

[131] Sun Gyu Choi, Tae-Jung Ha, Byoung-Gon Yu, Seung Pil Jaung, Ohmyoung Kwon, and Hyung-Ho Park. Improvement of uncooled infrared imaging detector by using mesoporous silica as a thermal isolation layer. *Ceramics International*, 34(4):833–836, 2008.

[132] Ming Lei, Ben Xu, Yutao Pei, Haibao Lu, and Yong Qing Fu. Micro-mechanics of nanostructured carbon/shape memory polymer hybrid thin film. *Soft Matter*, 12(1):106–114, 2016.

[133] Jesús Carrete, Wu Li, Natalio Mingo, Shidong Wang, and Stefano Curtarolo. Finding unprecedentedly low-thermal-conductivity half-heusler semiconductors via high-throughput materials modeling. *Physical Review X*, 4(1):011019, 2014.

[134] Ronggui Yang, Gang Chen, and Mildred S Dresselhaus. Thermal conductivity modeling of core- shell and tubular nanowires. *Nano letters*, 5(6):1111–1115, 2005.

[135] Vincent Dusastre. *Materials for sustainable energy: a collection of peer-reviewed research and review articles from Nature Publishing Group*. World Scientific, 2010.

[136] Jen-Kan Yu, Slobodan Mitrovic, Douglas Tham, Joseph Varghese, and James R Heath. Reduction of thermal conductivity in phononic nanomesh structures. *Nature nanotechnology*, 5(10):718–721, 2010.

[137] Yoshiaki Nakamura. Nanostructure design for drastic reduction of thermal conductivity while preserving high electrical conductivity. *Science and Technology of advanced MaTerialS*, 19(1):31–43, 2018.

[138] L Thumfart, J Carrete, B Vermeersch, N Ye, T Truglas, J Feser, H Groiss, N Mingo, and A Rastelli. Thermal transport through ge-rich ge/si superlattices grown on ge (0 0 1). *Journal of Physics D: Applied Physics*, 51(1):014001, 2017.

[139] Kevin D Parrish, Justin R Abel, Ankit Jain, Jonathan A Malen, and Alan JH McGaughey. Phonon-boundary scattering in nanoporous silicon films: Comparison of monte carlo techniques. *Journal of Applied Physics*, 122(12):125101, 2017.

[140] Jaeho Lee, Woochul Lee, Geoff Wehmeyer, Scott Dhuey, Deirdre L Olynick, Stefano Cabrini, Chris Dames, Jeffrey J Urban, and Peidong Yang. Investigation of phonon coherence and backscattering using silicon nanomeshes. *Nature communications*, 8(1):1–8, 2017.

[141] Edward Dechaumphai and Renkun Chen. Thermal transport in phononic crystals: the role of zone folding effect. *Journal of Applied Physics*, 111(7):073508, 2012.

[142] Navaneetha K Ravichandran and Austin J Minnich. Coherent and incoherent thermal transport in nanomeshes. *Physical Review B*, 89(20):205432, 2014.

[143] Taneli Juntunen, Osmo Vänskä, and Ilkka Tittonen. Anderson localization quenches thermal transport in aperiodic superlattices. *Physical review letters*, 122(10):105901, 2019.

[144] AJH McGaughey and M Kaviany. Thermal conductivity decomposition and analysis using molecular dynamics simulations. part i. lennard-jones argon. *International Journal of Heat and Mass Transfer*, 47(8-9):1783–1798, 2004.

[145] Payam Norouzzadeh, Amin Nozariasbmarz, Jerzy S Krasinski, and Daryoosh Vashaee. Thermal conductivity of nanostructured sixge1- x in amorphous limit by molecular dynamics simulation. *Journal of Applied Physics*, 117(21):214303, 2015.

[146] Sten Sarman and Aatto Laaksonen. The heat conductivity of liquid crystal phases of a soft ellipsoid string-fluid evaluated by molecular dynamics simulation. *Physical Chemistry Chemical Physics*, 13(13):5915–5925, 2011.

[147] Phillbot Keblinski, SR Phillpot, SUS Choi, and JA Eastman. Mechanisms of heat flow in suspensions of nano-sized particles (nanofluids). *International journal of heat and mass transfer*, 45(4):855–863, 2002.

[148] Yuping He, Davide Donadio, Joo-Hyoung Lee, Jeffrey C Grossman, and Giulia Galli. Thermal transport in nanoporous silicon: interplay between disorder at mesoscopic and atomic scales. *Acs Nano*, 5(3):1839–1844, 2011.

[149] LN Maurer, S Mei, and I Knezevic. Rayleigh waves, surface disorder, and phonon localization in nanostructures. *Physical Review B*, 94(4):045312, 2016.

[150] Sebastian G Volz and Gang Chen. Molecular-dynamics simulation of thermal conductivity of silicon crystals. *Physical Review B*, 61(4):2651, 2000.

[151] J-H Lee, JC Grossman, J Reed, and G Galli. Lattice thermal conductivity of nanoporous si: Molecular dynamics study. *Applied Physics Letters*, 91(22):223110, 2007.

[152] Stefanie Wolf, Neophytos Neophytou, Zlatan Stanojevic, and Hans Kosina. Monte carlo simulations of thermal conductivity in nanoporous si membranes. *Journal of electronic materials*, 43(10):3870–3875, 2014.

[153] Z Aksamija. Full band monte carlo simulation of phonon transport in semiconductor nanostructures. In *Proceedings of CHT-15. 6 th International Symposium on ADVANCES IN COMPUTATIONAL HEAT TRANSFER*. Begel House Inc., 2015.

[154] Jackson R Harter, Laura de Sousa Oliveira, Agnieszka Truszkowska, Todd S Palmer, and P Alex Greaney. Deterministic phonon transport predictions of thermal conductivity in uranium dioxide with xenon impurities. *Journal of Heat Transfer*, 140(5), 2018.

[155] Asegun S Henry and Gang Chen. Spectral phonon transport properties of silicon based on molecular dynamics simulations and lattice dynamics. *Journal of Computational and Theoretical Nanoscience*, 5(2):141–152, 2008.

[156] JE Turney, ES Landry, AJH McGaughey, and CH Amon. Predicting phonon properties and thermal conductivity from anharmonic lattice dynamics calculations and molecular dynamics simulations. *Physical Review B*, 79(6):064301, 2009.

[157] Steve Plimpton. Fast parallel algorithms for short-range molecular dynamics. *Journal of computational physics*, 117(1):1–19, 1995.

[158] Frank H Stillinger and Thomas A Weber. Computer simulation of local order in condensed phases of silicon. *Physical review B*, 31(8):5262, 1985.

[159] PC Howell. Comparison of molecular dynamics methods and interatomic potentials for calculating the thermal conductivity of silicon. *The Journal of chemical physics*, 137(22):2129, 2012.

[160] Patrick K Schelling, Simon R Phillpot, and Pawel Keblinski. Comparison of atomic-level simulation methods for computing thermal conductivity. *Physical Review B*, 65(14):144306, 2002.

[161] Jin Fang and Laurent Pilon. Scaling laws for thermal conductivity of crystalline nanoporous silicon based on molecular dynamics simulations. *Journal of Applied Physics*, 110(6):064305, 2011.

[162] Laura de Sousa Oliveira and P Alex Greaney. Method to manage integration error in the green-kubo method. *Physical Review E*, 95(2):023308, 2017.

[163] Dhritiman Chakraborty, Hossein Karamitaheri, Laura de Sousa Oliveira, and Neophytos Neophytou. Effect of wave versus particle phonon nature in thermal transport through nanostructures. *Computational Materials Science*, 180:109712, 2020.

[164] Dhritiman Chakraborty, Laura de Sousa Oliveira, and Neophytos Neophytou. Enhanced phonon boundary scattering at high temperatures in hierarchically disordered nanostructures. *Journal of Electronic Materials*, 48(4):1909–1916, 2019.

[165] Zhaojie Wang, Joseph E Alaniz, Wanyoung Jang, Javier E Garay, and Chris Dames. Thermal conductivity of nanocrystalline silicon: importance of grain size and frequency-dependent mean free paths. *Nano letters*, 11(6):2206–2213, 2011.

[166] Xinjiang Wang and Baoling Huang. Computational study of in-plane phonon transport in si thin films. *Scientific reports*, 4(1):1–10, 2014.

[167] Alan JH McGaughey and Ankit Jain. Nanostructure thermal conductivity prediction by monte carlo sampling of phonon free paths. *Applied Physics Letters*, 100(6):061911, 2012.

[168] Roman Anufriev, Jeremie Maire, and Masahiro Nomura. Reduction of thermal conductivity by surface scattering of phonons in periodic silicon nanostructures. *Phys. Rev. B*, 93:045411, Jan 2016.

[169] Navaneetha K. Ravichandran, Hang Zhang, and Austin J. Minnich. Spectrally resolved specular reflections of thermal phonons from atomically rough surfaces. *Phys. Rev. X*, 8:041004, Oct 2018.

[170] Jackson R Harter, Todd S Palmer, and P Alex Greaney. Predicting mesoscale spectral thermal conductivity using advanced deterministic phonon transport techniques. *Adv. Heat Transf.*, 52(INL/JOU-20-58945-Rev000), 2020.

[171] Fan Yang and Chris Dames. Mean free path spectra as a tool to understand thermal conductivity in bulk and nanostructures. *Phys. Rev. B*, 87(3):035437, 2013.

[172] Chengyun Hua and Austin J Minnich. Transport regimes in quasiballistic heat conduction. *Phys. Rev. B*, 89(9):094302, 2014.

[173] G. Romano. Efficient calculations of the mode-resolved ab-initio thermal conductivity in nanostructures. *https://arxiv.org/2105.08181*, 2021.

[174] Gang Chen. *Nanoscale energy transport and conversion: a parallel treatment of electrons, molecules, phonons, and photons.* Oxford University Press, USA, 2005.

[175] Giuseppe Romano, Alexie M Kolpak, Jesús Carrete, and David Broido. Parameter-free model to estimate thermal conductivity in nanostructured materials. *Physical Review B*, 100(4):045310, 2019.

[176] S. Aria Hosseini. https://github.com/ariahosseini.

[177] Wu Li, Lucas Lindsay, David A. Broido, Derek A. Stewart, and Natalio Mingo. Thermal conductivity of bulk and nanowire $\mathrm{mg}_2\mathrm{si}x\mathrm{sn}1-x$ alloys from first principles. *Phys. Rev. B*, 86:174307, 2012.

[178] S. Aria Hosseini, Giuseppe Romano, and P. Alex Greaney. Mitigating the effect of nanoscale porosity on thermoelectric power factor of si. *ACS Applied Energy Materials*, 4(2):1915–1923, 2021.

[179] Jiangtao Wei, Liangliang Yang, Zhe Ma, Peishuai Song, Mingliang Zhang, Jing Ma, Fuhua Yang, and Xiaodong Wang. Review of current high-zt thermoelectric materials. *Journal of Materials Science*, pages 1–63, 2020.

[180] Joachim Sonntag. Thermoelectric power in alloys with phase separation (composites). *Journal of Physics: Condensed Matter*, 21(17):175703, 2009.

[181] J-B Vaney, Andrea Piarristeguy, V Ohorodniichuck, O Ferry, Annie Pradel, Eric Alleno, Judith Monnier, Elsa B Lopes, AP Gonçalves, Gaëlle Delaizir, et al. Effective medium theory based modeling of the thermoelectric properties of composites: comparison between predictions and experiments in the glass–crystal composite system si 10 as 15 te 75–bi 0.4 sb 1.6 te 3. *Journal of Materials Chemistry C*, 3(42):11090–11098, 2015.

[182] Itzhak Webman, Joshua Jortner, and Morrel H Cohen. Thermoelectric power in inhomogeneous materials. *Physical Review B*, 16(6):2959, 1977.

[183] Thomas Lopez and Lorenzo Mangolini. In situ monitoring of hydrogen desorption from silicon nanoparticles dispersed in a nonthermal plasma. *Journal of Vacuum Science & Technology B, Nanotechnology and Microelectronics: Materials, Processing, Measurement, and Phenomena*, 34(4):041206, 2016.

[184] Uwe R Kortshagen, R Mohan Sankaran, Rui N Pereira, Steven L Girshick, Jeslin J Wu, and Eray S Aydil. Nonthermal plasma synthesis of nanocrystals: fundamental principles, materials, and applications. *Chemical reviews*, 116(18):11061–11127, 2016.

[185] Marc K Etherington, Nadzeya A Kukhta, Heather F Higginbotham, Andrew Danos, Aisha N Bismillah, David R Graves, Paul R McGonigal, Nils Haase, Antonia Morherr, Andrei S Batsanov, et al. Persistent dimer emission in thermally activated delayed fluorescence materials. *The Journal of Physical Chemistry C*, 123(17):11109–11117, 2019.

[186] CA Swenson. Recommended values for the thermal expansivity of silicon from 0 to 1000 k. *Journal of physical and chemical reference data*, 12(2):179–182, 1983.

[187] Kasper A Borup, Eric S Toberer, Leslie D Zoltan, George Nakatsukasa, Michael Errico, Jean-Pierre Fleurial, Bo B Iversen, and G Jeffrey Snyder. Measurement of the electrical resistivity and hall coefficient at high temperatures. *Review of Scientific Instruments*, 83(12):123902, 2012.

[188] C Wood, D Zoltan, and G Stapfer. Measurement of seebeck coefficient using a light pulse. *Review of scientific instruments*, 56(5):719–722, 1985.

[189] Je-Hyeong Bahk, Zhixi Bian, and Ali Shakouri. Electron energy filtering by a nonplanar potential to enhance the thermoelectric power factor in bulk materials. *Phys. Rev. B*, 87:075204, Feb 2013.

[190] Je-Hyeong Bahk, Zhixi Bian, and Ali Shakouri. Electron transport modeling and energy filtering for efficient thermoelectric $\mathrm{mg_2si_{1-x}sn_x}$ solid solutions. *Phys. Rev. B*, 89:075204, Feb 2014.

[191] T. J. Scheidemantel, C. Ambrosch-Draxl, T. Thonhauser, J. V. Badding, and J. O. Sofo. Transport coefficients from first-principles calculations. *Phys. Rev. B*, 68:125210, Sep 2003.

[192] Aaron J Schmidt, Kimberlee C Collins, Austin J Minnich, and Gang Chen. Thermal conductance and phonon transmissivity of metal–graphite interfaces. *Journal of Applied Physics*, 107(10):104907, 2010.

[193] M. Bachmann, M. Czerner, and C. Heiliger. Ineffectiveness of energy filtering at grain boundaries for thermoelectric materials. *Phys. Rev. B*, 86:115320, Sep 2012.

[194] Charles Kittel, Paul McEuen, and Paul McEuen. *Introduction to solid state physics*, volume 8. Wiley New York, 1996.

[195] E Flage-Larsen and Ø Prytz. The lorenz function: Its properties at optimum thermoelectric figure-of-merit. *Applied Physics Letters*, 99(20):202108, 2011.